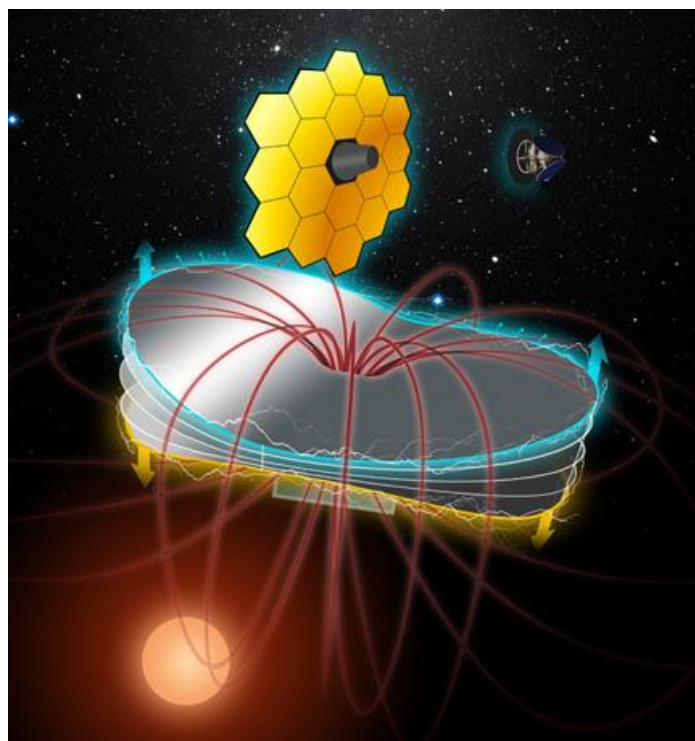# HIGH-TEMPERATURE SUPERCONDUCTORS AS ELECTROMAGNETIC DEPLOYMENT AND SUPPORT STRUCTURES IN SPACECRAFT

NASA NIAC Phase I
Final Report
MIT Space Systems Lab
10/1/2012

Gwendolyn V. Gettliffe   *gvg@mit.edu*

Niraj K. Inamdar   *inamdar@mit.edu*

RESEARCH MENTOR: Dr. Rebecca Masterson   *becki@mit.edu*

PRINCIPAL INVESTIGATOR: Prof. David W. Miller   *millerd@mit.edu*

Table of Contents

1 Chapter 1 - Introduction

1.1 Motivation

This report, concluding a one-year NIAC Phase I study, describes a new structural and mechanical technique aimed at reducing the mass and increasing the deployed-to-stowed length and volume ratios of spacecraft systems. This technique uses the magnetic fields generated by electrical current passing through coils of high-temperature superconductors (HTSs) to support spacecraft structures and deploy them to operational configurations from their stowed positions inside a launch vehicle fairing.

The chief limiting factor in accessing space today is the prohibitively large launch cost per unit mass of spacecraft. Therefore, the reduction of spacecraft mass has been a primary design driver for the last several decades. The traditional approach to the reduction of spacecraft mass is the optimization of actuators and structures to use the minimum amount of material required for support, deployment, and interconnection. Isogrid panels, composite honeycomb panels, and gas-filled inflatable beams all reduce the mass of material necessary to build a truss or panel, provide separation between elements, or otherwise apply surface forces to a spacecraft structure. An alternative to these "traditional" methods is the use of electromagnetic body forces generated by HTSs to reduce the need for material, load-bearing support, and standoffs on spacecraft by maintaining spacing, stability, and position of elements with respect to one another.

HTS structures present an opportunity for significant mass savings over traditional options, especially in larger systems that require massive structural components. Electromagnetic body forces generated by superconducting magnets are used to move and position spacecraft elements in lieu of traditional structural components, such as telescoping beams, segmented masts and inflatables. HTS structures have less mass per unit characteristic length of the spacecraft than aluminum beams and therefore offer the performance benefits of larger deployed structures while enabling the stowed structure to fit into existing launch vehicle payload fairings. However, the major cost of using HTS structures is the need to cool them to low temperatures so that they become superconducting, which requires passive cooling structures like heatshields or active cooling subsystems like cryogenic heat pipes. This work will also discuss the use of non-superconducting conductors for smaller forces or distances when passive cooling is not available. HTSs (which in general are superconducting at temperatures below 77K) and room-temperature conductors can be utilized in tandem to perform more complex operations.

This section explains the five primary benefits that HTS structures can offer to the aerospace community:

1. Reduced mass
2. Larger structures with same launch vehicles
3. Vibration- and thermally-isolated structures

4. Staged deployment, in-space assembly with fewer operations, and partial system replacements
5. Reconfiguration of structures after deployment

1.1.1. Reduced mass

HTS structures can change the way mass scales with size; above some characteristic size for each spacecraft structure, the HTS system weighs less than other methods. For small, simple structures, the mass associated with single or multiple electromagnets and their power systems may be greater than that of traditional or other low mass structural options. In those cases, HTS structures may not be an advantageous choice (unless they present an additional benefit to the system; see benefits 3-5 below). For larger structures, however, the initial mass cost of electromagnets is small compared to the mass of a solid, rigid structure. After the payload, the structural subsystem is the second largest average fraction of spacecraft dry mass across all mission categories, as shown in Table 1, making structural mass the obvious target for mass reduction. [1]

Table 1: Top 4 most massive subsystems average % of dry mass [1]

Subsystem (% of Dry Mass)	No Prop (%)	LEO Prop (%)	High Earth (%)	Planetary (%)
Payload	41%	31%	32%	15%
Struct/Mech	**20%**	**27%**	**24%**	**25%**
Power	19%	21%	17%	21%
Attitude D&C	8%	6%	6%	6%

One goal of our work, though not addressed more than qualitatively in the Phase I work, is to determine at what size HTS structural options become less massive than alternative structures. In order to compare the different alternatives, we define *linear structural density* as being the mass of the structural subsystem (including the mass of those elements of the electrical and thermal subsystems dedicated to structural deployment and support) divided by the length of the structure (for long, thin structures like booms) and *areal structural density* as being the mass of the structural subsystem divided by the area of the structure (for large, broad structures, like heatshields).

In contrast, the term *net areal density* is used in this work to refer to the total mass of a spacecraft per unit area of a specific characteristic structure, the area of which dictates a key performance parameter of the mission, such as the primary mirror of a telescope. Examining the *net* areal density of space telescopes over time reveals an unsurprising trend over time towards larger mirrors with lower areal densities. This trend is shown in Figure 1.
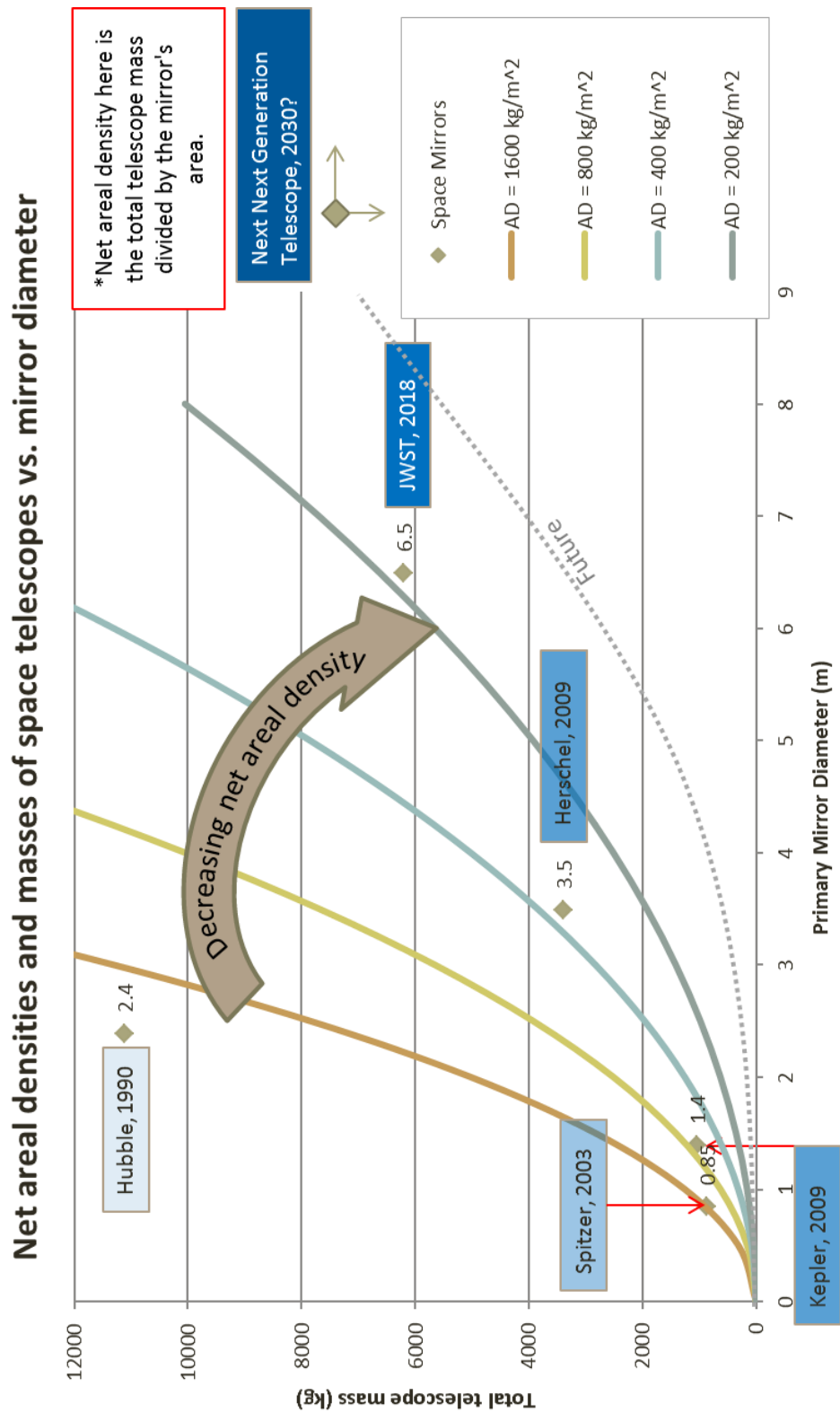
Figure 1: Chronological progression of net areal densities of space telescopes; mirror diameters listed beside points

As shown in Figure 1, each successively newer mission has a lower net areal density than the last, and each, with the exception of Hubble, has a larger primary mirror than the last. The James Webb Space Telescope (JWST) is the first space telescope being built with a primary mirror larger than the diameter of its intended launch vehicle and, as such, the mirror must be hinged, folded, and then deployed from its stowed position within the launch vehicle. As the available launch vehicle fleet remains relatively static in fairing size over the foreseeable future, larger space structures will require additional, likely complex and operationally risky deployments in order to fit inside the fairing envelope, which suggests another potential benefit of HTS structures.

1.1.2. Larger structures with same launch vehicles

Many space structures have performance benefits at larger sizes, but spacecraft size is limited by fairing envelope dimensions and maximum takeoff weight of launch vehicles. The high compaction ratio of HTS structures (related to how the stowed dimensions compare with the fully-deployed size of the spacecraft) means that spacecraft designers can reap the benefits of larger structures while being less size-limited by the launch vehicle. For instance, a stack of HTS coils and tethers that can deploy to a boom length of tens of meters may be less than a meter in stowed stack height, whereas aluminum beams can only be as long as the maximum dimension of the fairing envelope before requiring hinges and actuators. Figure 2, from Bearden, 2001 [2] , shows how launch vehicle costs increase with both orbit altitude and satellite dry mass, and how spacecraft going beyond LEO cost twice as much per kilogram as those launching to LEO. If HTS structures can reduce the mass of a spacecraft by even 5%, the potential savings, both in cost and usable launch vehicle capacity, are enormous.
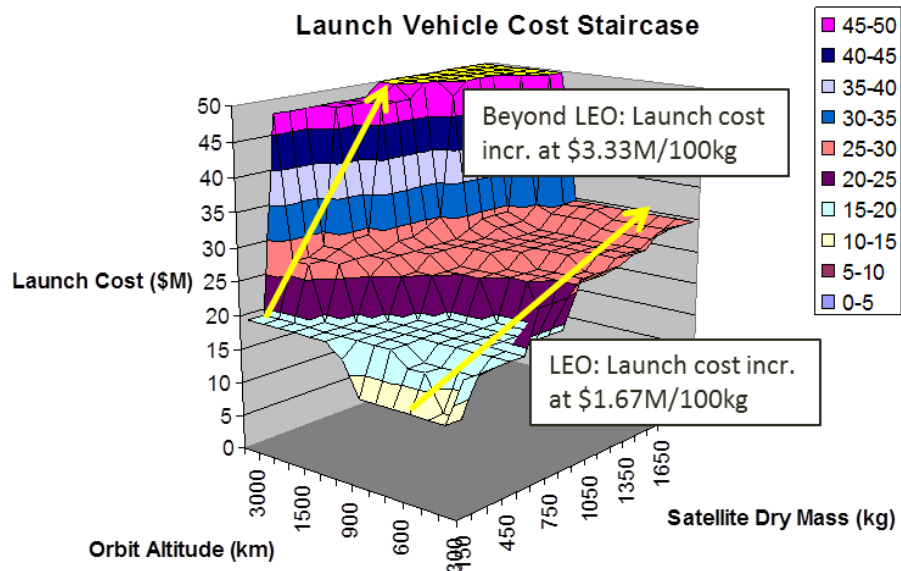

Figure 2: Launch vehicle cost with respect to orbit altitude and satellite dry mass. [2]

Example performance benefits of bigger structures:

- **Larger primary telescope mirrors can observe objects farther away because of finer angular resolution and increased effective aperture.**

$$\sin \theta = \frac{1.22\,\lambda}{D}$$

  The above equation shows the relationship between diffraction-limited angular resolution *Θ*, wavelength *λ*, and aperture diameter *D* for a circular aperture. Angular resolution in the telescope case is the minimum angle between distinguishable objects in the image produced by the telescope's objective, or primary mirror, which serves as the aperture when using the above equation. The larger D is, the smaller sin *Θ* is, which for small angles means a smaller *Θ*, thus giving a finer angular resolution and the ability to distinguish smaller distances in the telescope's image, unless the payload's resolution is otherwise limited by the design of the focal plane sensor.

- **Larger solar sails provide more thrust via greater surface area over which solar pressure acts.**

- **Larger parabolic radio frequency antennas have higher gain and can enable more distant missions or increased transmission data rates.**

$$\text{Gain} = \frac{4\pi\eta A}{\lambda^2}$$

  where η is the antenna efficiency, λ is the wavelength of the signal being transmitted, and A is the effective antenna area. Gain varies directly with A.

- **Larger solar panels can hold more photovoltaic cells and thus generate more power.**
- **Longer synthetic aperture radar arrays achieve finest resolution in both cross- and along-track dimensions by minimizing along-track (AT) dimension and maximizing cross-track (CT) dimension.**
- **Larger heatshields can keep more (or bigger) equipment cold.**

While larger structures provide performance benefits, launch vehicle constraints limit payload linear dimensions and mass. Table 2 shows the payload capacities of the largest currently available and proposed launch vehicles (sans the SLS, which has no hard specifications available at this date but is rumored to have an 8m diameter payload fairing), including the maximum mass of payload to LEO, the fairing diameter and usable envelope diameter within the fairing, and the maximum fairing height for the vehicle. Green rows are the current heavy launch fleet; blue are proposed or in-development vehicles; and brown are retired vehicles.

Table 2: Current and proposed launch vehicle specifications

Large Launch Vehicles	Fairing diameter (m) / usable envelope (m)	Max fairing height (m)	Payload to LEO (kg)
Delta IV Heavy	5.1/**4.57**	9.72	23000
Ariane V	5.4/**4.57**	17	21000
Proton	4.35/**4**	15.25	20700
Atlas V HLV (proposed)	5.4/**4.57**	13	29400
Falcon Heavy (in dev)	5.2/**4.6**	11.4	53000 (~26000 if fully reusable)
Space Shuttle (retired)	~**4.6**	8	24400 after Challenger, 29000 was original specification

Structures larger than about 4.5m in two or more dimensions are thus unable to fit into any of the currently available launch vehicles without needing to be condensed in at least one dimension. HTS structures provide a means for increasing the deployed-to-stowed length ratio of a structure that can be launched by one of the current fleet of launch vehicles.

1.1.3. Vibration- and thermally-isolated structures

Structures that are electromagnetically supported (and thus have empty space between them instead of solid structures) minimize the conductive pathways between spacecraft elements. This enables better thermal and vibrational isolation for sensitive components than if other parts of the vehicle are physically joined together.

The pointing accuracy and image quality of precision instruments is affected by coupled vibrations or jitter in the structure from internal or external disturbances (the latter including gravity gradient torqueing and solar pressure). Longer structures have a greater displacement at their far end than do shorter structures for the same angle rotation as well as a lower fundamental frequency, which is undesirable due to potential coupling with the launch vehicle during launch and with the attitude control system during operations. Attitude control of the spacecraft becomes much more difficult when the fundamental frequency is low.

The cryocoolers used with cryogenic heatpipes for cooling superconducting coils generate their own disturbance profiles, so vibrational isolation is more approachable in systems already possessing passive areal cooling in the form of a sun- or heatshield.

1.1.4. Staged deployment, in-space assembly, and partial system replacements

In combination with electromagnetic formation flight, which will be discussed in greater detail in Section 2, HTS structures minimize or eliminate connections between spacecraft parts such that a heatshield and a mirror assembly of a spacecraft like JWST, for instance, do not have to be launched at the same time. Additionally, the entire spacecraft would not have to be replaced should one of the two fail because the parts are independent and do not require much or any physical assembly. This could give large, complex spacecraft longer lifetimes and the ability to be serviced or replaced at distances as great as Earth-Sun L2.

1.1.5. Reconfiguration of structures after deployment

Reconfigurability is a spacecraft function that is not currently cost effective since two different functional designs on a single vehicle require a large amount of additional structural/mechanism mass, and the benefits are usually not worth the added design complexity. HTS structures allow for dynamic changes in boom length, solar array placement, and heatshield angle, as well as reversible deployments in some configurations – the capability to reconfigure could create a whole new paradigm of multi-purpose spacecraft. Much of the analysis done in Chapter 4 supports the capabilities of HTS structures for use in Reconfigurability, and while HTS structures carry a significant power and thermal burden in their use, in large, high-performance systems, unique capabilities like Reconfigurability might be worth the trade, especially in designs where the coils do not have to be superconducting and in use at all times. This Phase I study and report aims to provide information about the potential of HTS structures for such unique functions as well as information about the feasibility of HTS structures overall.

1.2   Study objectives/Research questions
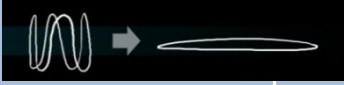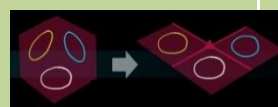
The three major questions that this report addresses are related to the technical feasibility of HTS structures, the spectrum of viable applications to spacecraft, and the new operations enabled or made substantially more realistic by HTS structures respectively.

Question 1: *Can we use electromagnetic forces generated by and acting between high-temperature superconductor current-carrying coils to move, unfold, and support parts of a spacecraft from its stowed position?*

In order to answer that question, we first define functional configurations of coils that can be used to perform specific operations onboard a spacecraft, distinguished from each other by their degrees of freedom, starting and ending positions, number of coils, and whether they are done at initial deployment of a structure or at a point later in the operational lifetime.

HTS coils can repel, attract, and even shear with respect to one another; in a flexible, non-circular coil, elements of the same coil can perform these actions on one another, deforming the shape of the coil over time. In combination with various boundary conditions, these operations lead to the seven functional coil configurations, depicted in Table 3, that we have identified for use in spacecraft deployment and support activities: four (1-4, in blue) are for initial deployment and three (5-7, in green) are variants of the deployment configurations for use in overall spacecraft shape change during the spacecraft operational lifetime. Table 3 describes the configurations and the spacecraft operations they could perform. These configurations will be capitalized when referred to in this report.

Table 3: Seven potential functional coil configurations

Configuration	Phase	Description	Uses
1. Expand	Deployment	A single, flexible HTS coil that is folded in its stowed position and uses its own magnetic field when current is run through it to Expand to flat shape	To deploy and hold taut the perimeters of large membranous or flexible structures
2. Inflate	Deployment	A 3D structure is built with two or more repelling coils in a configuration that creates a space between the two, Inflating a structure (bounded by flexible walls or tethers)	To create a volume (such as a tank or toroidal perimeter) or to increase surface area (for solar cells)
3. Unfold	Deployment	A series of coils embedded in or attached to a structure that is stowed folded and must be Unfolded to become operational (folds can be hinges, springs, or couplings)	To deploy long, flat structures (like solar panels) or to take advantage of mechanical resistance at folds to create variable angles
4. Separate	Deployment	Corollary of Inflate, in which two or more coils repel each other in series facing each other to Separate two parts of a spacecraft; tethered or membranous structure connecting	To put large, controllable distance between two sensitive parts of spacecraft (such as a nuclear reactor, astronauts, optics, thrusters)
5. Deform	Operational	Two or more coils embedded in parts of the structure act magnetically on each other to temporarily Deform or change the shape of the spacecraft	To reduce radar cross section (RCS) or adjust shape for avoidance of debris
6. Reconfigure	Operational	Corollary of Deform, except Reconfigured state is sustainable and lasting	To reduce drag profile or Reconfigure satellite for different ConOps
7. Refocus	Operational	Two or more coils adjust their magnetic state such that an antenna or mirror is Deformed to Refocus it. Orientation of coils dependent on original shape of mirror or antenna.	To change focus lengths of mirrors and gains of antennas by reforming or moving their dishes, mirrors, or horns to Refocus them on a new target

The four deployment configurations (1-4 in Table 3) are numerically modeled in MATLAB and Simulink to verify that the deployments can be performed as described in Table 3 and are validated in the far-field (where the coils are very far apart from one another) against the dipole approximation of coil forces and torques. Chapter 3 describes these models and how they were constructed and validated.

Question 2: *For which operations does this technology represent an improvement over existing or in-development options?*

In order to investigate the performance of HTS structures versus other low-mass structural technologies, the ranges of key performance parameters over which HTS structures are viable options for spacecraft design must first be determined. Chapter 4 characterizes the performance of HTS structures using the models introduced in Chapter 3, while in Chapter 5 they are compared to other structural options, both traditional rigid metal structures and "alternative" structures made with different materials and deployment operations.

Question 3: *What new mission capabilities does this technology enable?*

The Reconfigure, Deform, and Refocus operational configurations all represent mission capabilities that have heretofore required structures and mechanisms that are too expensive in metrics like mass, size, or power or are too complex and therefore too risky to justify for the additional performance benefits that they offer. This is why spacecraft do not commonly include these capabilities.

Using magnetic forces, however, such shape-changing mission capabilities are not structurally much different from the deployment and support configurations required to move from a stowed configuration to a deployed one, so including the ability to Reconfigure or Deform utilizes the existing structural architecture more efficiently than in non-electromagnetic structures. Operational configurations will be discussed further in Chapters 3 and 4.

The goal of this report is to provide analyses of the dynamics of rigid (and, briefly, flexible) electromagnetic coils when exerting forces and torques on one another, such that we can support a positive answer for Question 1, narrow down the field of potential deployment and support functions that are worth further study for Question 2, and explore new spacecraft architectures that have not previously been worth seriously entertaining for Question 3.

2   Chapter 2 – Background

This chapter introduces the foundational scientific principles for HTS and reviews previous development efforts to mature key enabling technologies for HTS electromagnetic structures. We discuss the enabling scientific principles and phenomena that form the basis of our study, draw lines between HTS structures and previous space electromagnetic work, and briefly examine the maturity of the HTS structure concept before moving into more theoretical analysis of the deployment dynamics in Chapter 3.

2.1   Scientific principles enabling HTS structures

HTS structures are enabled by the fundamental scientific principles of electromagnetism and the unique environment of space, as well as the developments made over the last several decades in manufacturing superconductors and controlling electromagnets onboard multi-system vehicles. The industry development is explored in later sections; this section describes the underlying fundamental scientific principles that enable HTS structures, including:

1. The creation of Lorentz and Laplace forces via interaction of a magnetic field and current
2. The Meissner effect, superconductivity, and the manufacturing of HTS wire
3. Enabling characteristics of space environment (microgravity and vacuum)

2.1.1   Generation of Lorentz and Laplace forces

HTS structures operate using electromagnetic forces to push, pull, and move with respect to each other. Electromagnetic forces (called Lorentz or Laplace forces depending on whether the force is acting on a single charge or a current of charges respectively) result from the interaction of a magnetic field and a current.

A point charge q moving with velocity $\vec{v}$ in external magnetic and electric fields, $\vec{B}$ and $\vec{E}$ respectively, experiences a Lorentz force $\vec{F}$, given by:

$$\vec{F} = q[\vec{E} + \vec{v} \times \vec{B}]$$

where $q\vec{E}$ is the *electric* force, and $q\vec{v} \times \vec{B}$ is the *magnetic* force. The macroscopic force on a wire is the *magnetic* force and is called the Laplace force. It is generated by a magnetic field $\vec{B}$ on a wire carrying current $\vec{I}$ (a stream of point charges) as follows:

$$\vec{F} = I \int_{wire} d\vec{l} \times \vec{B}$$

The magnetic force is thus orthogonal to the wire and to the orientation of the magnetic field at the point of calculation. In order to calculate the magnetic field $\vec{B}$ for use in determining the Laplace force on a wire or coil of wire, one can use the Biot-Savart law, which can be derived from Ampère's law and Gauss's law, to compute the resultant magnetic field vector $\vec{B}$ at a position **r** with respect to a steady current *I*:

$$\vec{B} = \frac{\mu}{4\pi} \int\limits_{wire} \frac{I d\vec{l} \times \vec{r}}{|\vec{r}|^3}$$

In the deployment modeling work that will be described in Chapter 3, the magnetic field and the Laplace forces across a current-carrying wire are approximated over time by implementing the Biot-Savart law numerically, discretizing electric current elements in order to determine the magnetic field generated by arbitrary configurations of rigid (meaning a fixed, non-changing shape) and flexible coils. Knowledge of the magnetic field at each point in space around a current-carrying wire allows the calculation of the resultant force upon another current-carrying wire as a result of that magnetic field, which can then be used to determine the number of turns a coil requires or how much current it needs to carry in order to deploy a structure.

2.1.2   Meissner effect, superconductors, and manufacturing of HTS wire

Superconductors enable HTS structures because they are able to generate much larger forces via their larger current carrying capacity, which increases the distance over which they can work for the same amount of mass. Superconductors are materials that conduct electrical current perfectly below a critical temperature T_c; superconductors have zero resistivity, with negligible quantities right around their T_c. Any current through them will persist significantly longer than through a non-superconductive material. Superconductivity is characterized by **the Meissner effect**, the expulsion of an external magnetic field from a superconductor once cooled below its T_c during its transition to a superconducting state. Every superconductor has a critical temperature, external magnetic field strength, and current density above which superconductivity ceases, shown graphically in Figure 3.
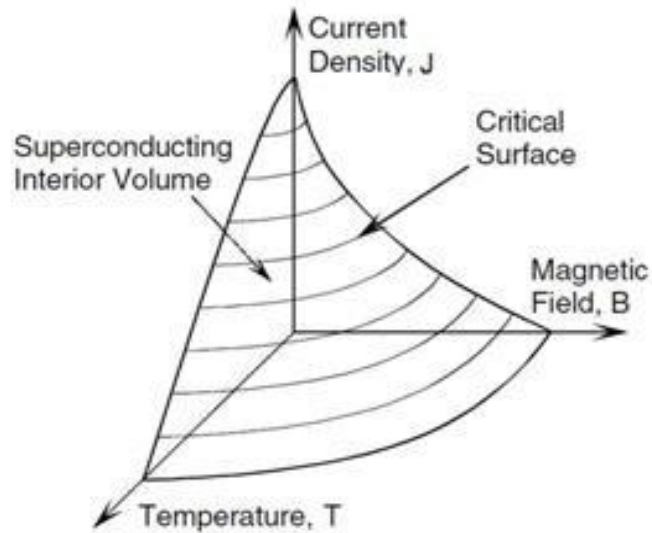
Figure 3: Critical surface for Type II superconductor [3]

High-temperature superconductors, or HTSs, are those superconductors with T_cs above 77K, or the boiling point of liquid nitrogen, enabling them to be cooled to a superconducting state using LN2. The higher the T_c, the less it costs (in terms of power, storage, and consumables, for applications where a cryogen is not recycled) to do the cooling. HTS development and the subsequent development of HTS wire has led to a broad array of applications for superconductors, including long distance power transfer, electromagnets, and energy storage.

There are two types of superconductors; Type-I only exhibit the Meissner effect with one critical field strength above which superconductivity ceases. Type-II superconductors, which include all high-temperature superconductors, as well as some low-temperature superconductors (LTSs) with T_cs too low to qualify as "high-temperature", also exhibit **a "mixed-state" Meissner effect** that increases their critical magnetic fields and configuration stability. Because of this effect, Type-II superconductors are often used in superconducting magnets in the form of coils of wire made with superconductor filaments embedded in support material less than a millimeter in diameter.

The "mixed" Meissner effect is different from the Meissner effect in that some magnetic field penetrates the superconductor through filaments of normal-state material, and the material can support higher magnetic fields before superconductivity breaks down. There are thus two critical field strengths in Type II superconductors: beyond the first field strength, where superconductivity would cease completely in a Type I superconductor, a vortex ("mixed") state exists in which some magnetic flux is allowed to penetrate the material while it continues superconducting. Beyond the second, higher critical field strength, superconductivity ceases.

Type-II superconductors are the only type of superconductor used in wire. Many of these types of wire are made with HTSs to lower cooling costs, especially for non-magnetic applications. Some wire, however, especially that which is used in powerful electromagnets like those in the Large Hadron Collider, is made with LTSs that need to be kept much colder but

can sustain much higher current densities than HTSs. For example, niobium–tin (Nb3Sn) has a T_c of 18.3K and can withstand magnetic field strengths up to 30 tesla (with a record current density of 2643 A/mm^2 at 12T and 4.2K) [4]. HTS wires do not have the same current densities, and, as a result, they cannot generate magnetic fields as high as LTSs. But, though pure HTS materials are just as brittle as LTS materials, HTSs can be constructed into flexible, durable wire. The flexibility of HTS wire enables the Expand configuration that we proposed earlier in this section for deployment of a single, folded and stowed coil into a large, flat, expanded coil.

Compared to standard, room-temperature conductors, HTS wires are able to create larger magnetic fields and sustain higher current densities, with little-to-no resistive losses through the wire (compared to high resistive losses in copper and aluminum). While room temperature conductor coils can be used to magnetically operate on each other, the Laplace forces able to be generated on each other are significantly lower than those that can be created with HTS coils, due to the lower induced magnetic field. HTS wire thus enables electromagnetic structures with multi-meter separation between coils, which in turn enables larger vehicles and the performance benefits enumerated in Chapter 1 that accompany larger structures.

Whereas several decades ago it was difficult for manufacturers to create HTS wire of any useful length, **HTS can now be created in lengths upwards of 1500m** [5], reducing the need for splices that result in resistive losses of power to heat. Individual strands of tape-shaped (wide and thin) cable are multilayered with various substrates and insulators for mechanical strength and chemical stability while at the same time trying to maximize the current density of the wire. Figure 4 shows a cutaway view of an HTS wire.
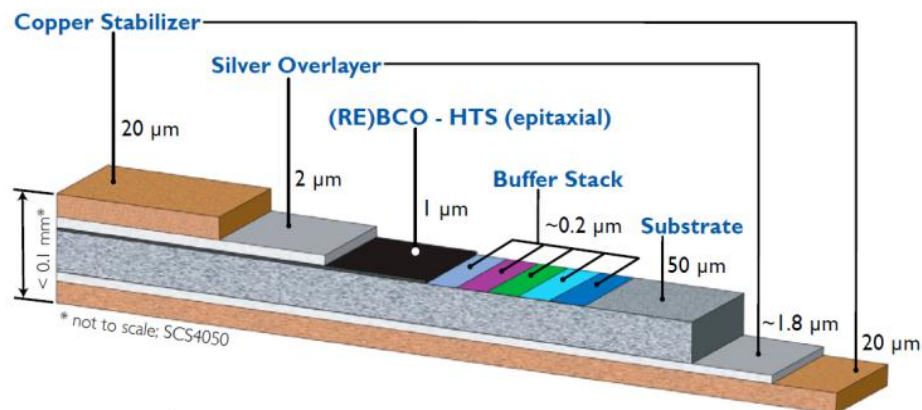
Figure 4: Cutaway view of a 2G HTS wire [6]

Roebel cables, shown in Figure 5, implement a way of winding together individual wire strands to reduce AC losses due to self-field interaction with the current running through each strand, reducing the critical current I_c able to pass through that wire. When determining the configuration of turns in a coil or strands in a cable, it is especially important to consider how the self-field affects the I_c in each strand to optimize for the maximum current density in the coil cross-section possible.

Figure 5: 15-strand HTS Roebel cable [7]

SuperPower Inc, a subsidiary of Furukawa Electric Co., Ltd, manufactures a flexible "2G", or second generation, HTS wire with a minimum bend diameter of 11mm at room temperature (and at least 25.4 mm at superconducting temperatures) and maximum hoop stress of 700 MPa before irreversible degradation of the critical current. Recent axial stress-strain measurements conducted at the Naval Research Laboratory on standard 4 mm wide SCS4050 production wire gave a yield stress for the wire of 970 MPa at 0.92% strain. [8] The 2G HTS wire can carry between 250 and 350 A/cm wire width (or 25 – 35 kA/cm2 with a .1mm wire thickness) through 650m lengths (80-110A critical current with a 4mm wire width) [6]. We use the properties of this 2G wire in our models.

2.1.3   Space environment

On the ground, gravity and the need to cool superconductors in an otherwise room-temperature environment makes using electromagnets as actuators or structural support difficult and not broadly useful. In the space environment, however, an electromagnet does not need an enormous magnetic field to actuate components, and there is no air transferring heat into the magnet by convection, making space a potentially favorable environment for the use of HTS structures.

The microgravity environment of space enables HTS structures because spacecraft elements can be actuated without overcoming gravitational forces. Thus, only small forces are needed to cause motion or actuation, reducing the necessary size and current of electromagnets used for such tasks compared to what would be needed, for instance, to repel a coil upwards on the Earth's surface.

The vacuum of space is both beneficial and detrimental to the use of superconductors. If it can avoid radiated input from the sun, Earth, or the space vehicle, a thermally isolated HTS subsystem can maintain superconducting temperatures without cryogens. However, it is difficult to remove heat from the system in a vacuum if it cannot be isolated from conductive or radiating heat sources. This thermal environment makes more advanced cooling systems, like the cryogenic heatpipe described in Section 2.2, necessary for maintenance of the superconductor below its critical transition temperature.

2.2   Enabling technology and previous work

A number of previous and ongoing industries and projects lend credibility to the concept of using HTS to actuate spacecraft elements with respect to one another, including (1) **dynamics and control** technologies and testbeds like MIT SSL's electromagnetic formation flight (EMFF) testbed and the University of Maryland's (UMD) RINGS project (slated to fly to ISS in December 2012) Peck's flux pinning [9], and Pedreiro's Disturbance Free Payload [10]; and (2) **thermal control** innovations like Sedwick's cryogenic heatpipe for HTS coil cooling.

1.   <u>**Dynamics and control**</u> of a spacecraft without a support structure become a significant challenge and represent the majority of the work that must be done to design a system of electromagnets, since actuation and support are dictated by the feedback-informed distribution and direction of power through wire. The MIT SSL and UMD Space Power and Propulsion Laboratory have studied the problem of controlling electromagnetic coils in 3- and 6-DOF systems for the last decade, showing that control of free-flying or tethered vehicles with electromagnets is feasible and reinforcing the concept of using HTS coils to deploy a structure.

Electromagnetic formation flight (EMFF), has been the subject of study by the MIT SSL since 2002, funded by the original NIAC program (Phase I and Phase II studies), NRO DII, the JPL TPF Program, NASA GSFC SBIR, and DARPA. In 2003, the MIT AeroAstro senior capstone design class focused on the development of an algorithm for formation control using the inter-vehicle forces from steerable electromagnetic dipoles. As part of the class, and with funding from the NRO DII and the NASA Institute for Advanced Concepts, the MIT group implemented a laboratory testbed that used high temperature superconducting (HTS) wire to create electromagnetic coils. In a follow-on effort, MIT and Aurora Flight Sciences (AFS) investigated the performance of a room-temperature conductor version of EMFF (termed microEMFF). This effort included both a performance assessment and construction of a ground-based microEMFF testbed. *Resonant Inductive Near-field Generation System (RINGS),* is a joint UMD SPPL/MIT SSL/AFS project that, among other things, is a microEMFF demonstration onboard the International Space Station. These programs have included intensive control algorithm development as well as TRL development of the HTS EMFF concept to TRL 4 and the microEMFF concept to TRL 5, once RINGS begins operations on ISS.

The basic concept of EMFF is to provide actuation in relative degrees of freedom for formation flight systems using electromagnetic forces/torques and reaction wheels. The positions of system elements can change so long as the center of mass of such a system remains fixed (barring external input). The motivation for EMFF in multi-vehicle systems is fourfold:

- Station-keeping for distributed satellite systems
- Replacement of consumables (thrusters)
- Elimination of thruster plumes
- Enabling of high delta-V formation flying missions

EMFF Testbed Parameters	
Mass (single vehicle)	36 kg
Height	1.18 m
Maximum Diameter	0.90 m
Operating duration	~ 20 minutes
Table dimensions	3 m x 1.5 m
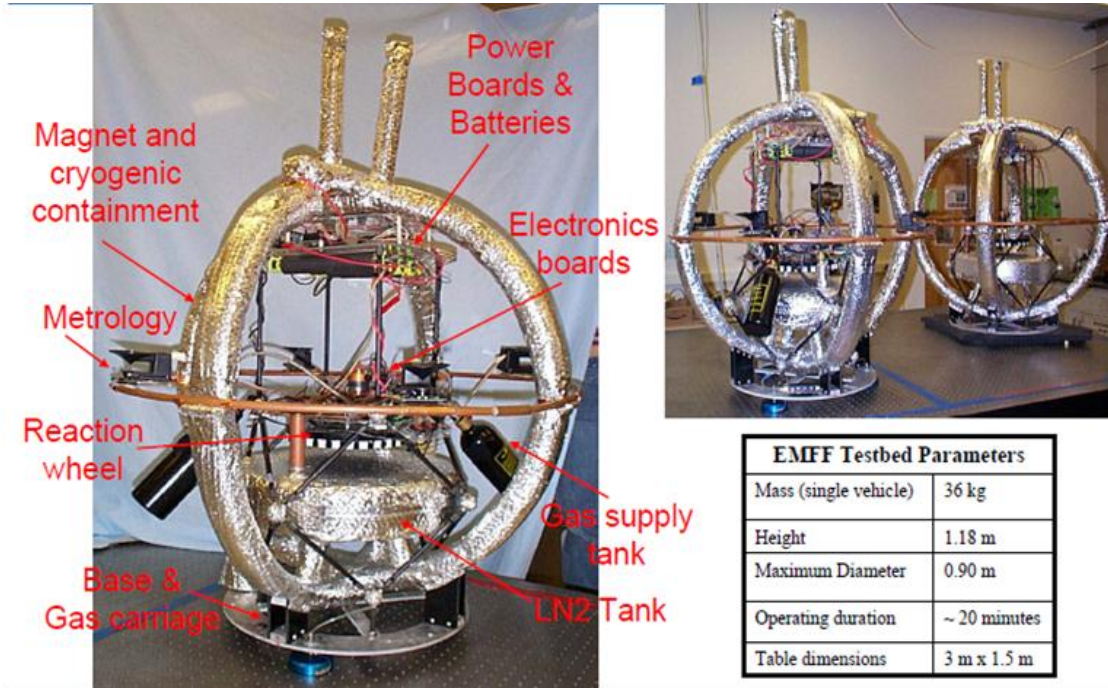
Figure 6: MIT SSL EMFF Testbed [11]

In the 3DOF EMFF testbed built at MIT SSL, shown with subsystem labels and with both test vehicles in Figure 6, vehicles exert electromagnetic forces and torques on each other using two perpendicular HTS coil electromagnets each. A 6DOF system would use three orthogonal HTS coils to create a completely electromagnetically steerable magnetic dipole. The reaction wheel decouples torques, allowing independent control of a vehicle's rotation.

During MIT SSL's previous work with this experimental testbed, several control algorithms were developed and validated. These results show that the relative position of spacecraft can be controlled and stabilized using 1 to 3 electromagnetic coils and 3 reaction wheels per vehicle [12]. While this particular testbed was not a consumable-free, closed-loop system (LN$_2$ cooled the superconductors but was allowed to boil off), the cryogenic heatpipe previously discussed enabled a closed-loop system with no LN2 loss.

RINGS, or Resonant Inductive Near-field Generation System, is an electromagnetic formation flight and wireless power/data transfer testbed that will begin operations on the ISS in December 2012. It is an add-on to the SPHERES (Synchronized Position Hold Engage and Reorient Experimental Satellites) developed by MIT SSL and is currently being operated by NASA Ames Research Center as a National Lab onboard the ISS. RINGS is an advancement of the microEMFF concept in that it uses room-temperature conductors instead of

superconductors, and its use on the ISS will advance the TRL of microEMFF to 5 via brassboard demonstration in a relevant environment. The RINGS consist of two 155-turn, 0.685m outside diameter coils of non-insulated air-cooled aluminum cable enclosed in a protective plastic shielding. One coil is mounted on each of two SPHERES as shown in Figure 7 and, using the SPHERES' CO2 thrusters to steer the dipole, the coils can be used to maneuver with respect to one another magnetically.
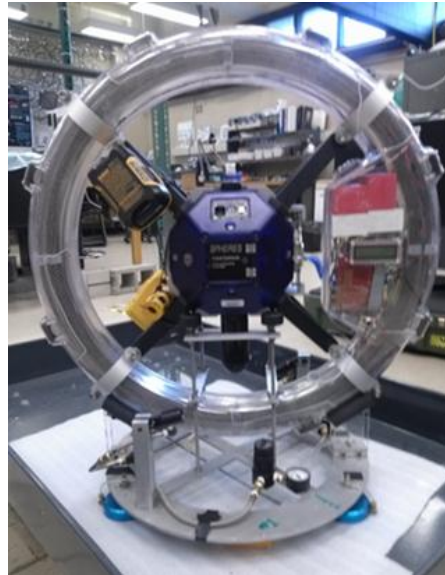
Figure 7: A SPHERE outfitted with RINGS hardware in laboratory

The primary differences between the application of HTSs in EMFF and in structures/deployment are (1) the presence or absence of physical connection paths between interacting coils and (2) the level of real-time direction the system has over the movement of coils.

EMFF vehicles can steer their dipoles in response to real-time system input to maneuver with respect to one another and have reaction wheels to cancel out torque when shearing with another vehicle. HTS structures are limited by their physical connection to the elements that they are moving, and their movements are planned for and constrained to certain, predictable paths, as is desired when deploying spacecraft elements to operational configurations. It is important to note that HTS structures can isolate different parts of a spacecraft vibrationally to a greater extent than can solid structures, but unless the elements are formation flying, there are still some transmission paths of forces and vibration, limiting movement of a coil in at least one degree of freedom. The EMFF project did not focus on deployment dynamics and the stability of transient states from one position to another without capacity for 6DOF control and steering of the resultant dipoles, thus further work is required to characterize this feasibility risk (and control design challenge) for the HTS structures application. Although controllability is a major component of technical feasibility for HTS structures, it is not the focus of this report.

Electromagnetic actuation on spacecraft has been the subject of research by a number of groups because of its potential for vibrational isolation and reconfiguration. **Disturbance Free Payload, or DFP**, is an architecture developed by Pedreiro et al for use in vibration isolation of

spacecraft payloads from the rest of the spacecraft using multiple electromagnetic actuators [10].

Flux pinning is an electromagnetic phenomenon in superconductors that enables highly accurate positioning between an electromagnet and a permanent magnet or other magnetic field source that can be used for safer and easier in-space assembly and reconfiguration of space systems in orbit. Small defects in the superconducting material can increase critical magnetic fields and contribute to the stability of the system by fixing vortex points, or filaments, through which magnetic field lines pass and are subsequently pinned when the superconductor is cooled below its T_c. Pinning of the field lines pins the source of the magnetic field in position and orientation. A number of joints, hinges, and interfaces can be created using configurations of permanent magnets to limit or direct the motion of a superconducting cube about the permanent magnets. As of 2009, multi-centimeter gaps between the magnets were supportable with high stiffness and damping with small masses. Flux pinning as a means of supporting and manipulating space structures is the subject of work by Peck et al at Cornell University [9].

Stiffening of membranous or low net areal density structures has been proposed on multiple occasions, such as Zubrin's "magsail" concept in which a large membranous plasma wind sail is held taut using a flexible HTS coiled around its perimeter to repel itself into a circle and keep the sail under tension. Zubrin ultimately selected a non-magnetic deployment system (rotating booms to deploy the sail initially using centrifugal force), citing "reliable deployment" as a key issue for magsails. [13] A previous NIAC study performed by Powell et al [14] proposed a system like that being studied in this report: flexible cables made of high-temperature superconducting wire Expanding or Inflating in order to serve as deployment actuators, perimeter support, and standoff structures simultaneously for large scale spacecraft. Powell primarily discusses the HTS wire properties and materials and does not go into detail on the deployment process. This report will explore such magnetic deployment in detail in an effort to determine if magnetic deployment is feasible, and if so, for what types and sizes of structures.

Other past studies of deployment or support using electromagnetism in membranous structures include microwave beam-driven spin deployment of solar sails (Benford, [15]) and membranous structures containing conductive meshes that can be shaped using magnetic pressure from permanent magnets or electromagnets (Amboss, [16]).

For applications that require long, low-mass structures, HTS structures are more suited than flux pinning or DMP to deployment and support in those situations. The possibility remains, however, of using a combination of flux pinning, DMP, EMFF, and HTS structures to magnetically assemble, deploy, and support large and complex space structures. Other light structural technologies like inflatables or tensegrity structures do not have active control over their shape; they attempt to deploy and either succeed or fail, and then they passively maintain their configuration for the lifetime of the vehicle. The ability to control and change the magnetic field means that electromagnetic structures are able to change their shape after deploying, depending on their boundary conditions.

2.   **Thermal control** down to cryogenic temperatures is necessary to induce superconductivity in HTSs. This level of thermal control is not normally present on spacecraft unless the vehicle has a payload that requires special cooling, making the need for cooling one of the primary disadvantages of HTS structures. Additionally, HTS performance is dictated by its warmest temperature, meaning that cooling devices are required at every point along the coil, which is not feasible (or even accomplishable), for large coils. Cooling equipment that can cool the full perimeter of a coil is needed and must be scalable to different size coils. Such equipment should preferably be consumable-free so as not to limit the lifetime of the mission. If the thermal control requires too much mass and power, the thermal subsystem could make HTS structures less competitive with traditional structures by nullifying any potential savings of HTS structures.

The cryogenic heatpipe developed by Sedwick and Kwon [11] for use in EMFF, pictured in Figure 8, provides a starting point for continued development and improvement of a competitive HTS coil cooling system by accomplishing consumable-free isothermalization to cryogenic temperatures (the same temperature at every point on the coil) with a single cryocooler.

Figure 8: Cross-section of heat pipe (left) and cryogenic heatpipe (copper casing) in open toroidal vacuum chamber (right)

This rigid heatpipe uses nitrogen as a working fluid and a stainless steel mesh as the wicking structure, with the HTS coil enclosed within the heatpipe instead of residing externally as with traditional heatpipes. A condenser, operated with an LN2 reservoir (like in the laboratory setup shown in Figure 8) or powered by a cryocooler, extracts heat from the system while the mesh passively wicks the condensed LN2 around the pipe via capillary action on several layers of wire mesh to cool and achieve isothermalization of the coil. Isothermalization means that minimal temperature gradients exist across the entire coil. Isothermal conditions are desired because the warmest point in the coil is the limiting factor in the performance of the HTS wire. When used with a cryocooler, as in the composite heatpipe design discussed next, this heatpipe is a closed system wherein the working fluid is conserved so long as the system remains sealed.

UMD SPPL conducted additional heatpipe development under a NASA STTR, in cooperation with Axis Engineering Technologies, Inc. [17]. The principal heatpipe design remained the same; however, the focus was on manufacturability of the heatpipe, which was previously found to be problematic. The issue was that the superconducting coil had to be a continuous spiral, requiring that the housing be formed around the coil. The housing must also be thermally conductive but ideally electrically insulating, since eddy currents developed in the housing would generate heat and dissipate power.

The resulting design is shown in Figure 9. The clamshell design is constructed from a thin-walled composite material, instead of the copper used in the first heatpipe, held together with a set of inner and outer clamp rings. The composite material is electrically insulating, but the thin wall allows for good heat conducting radially. The outside of the pipe is subsequently coated with MLI.
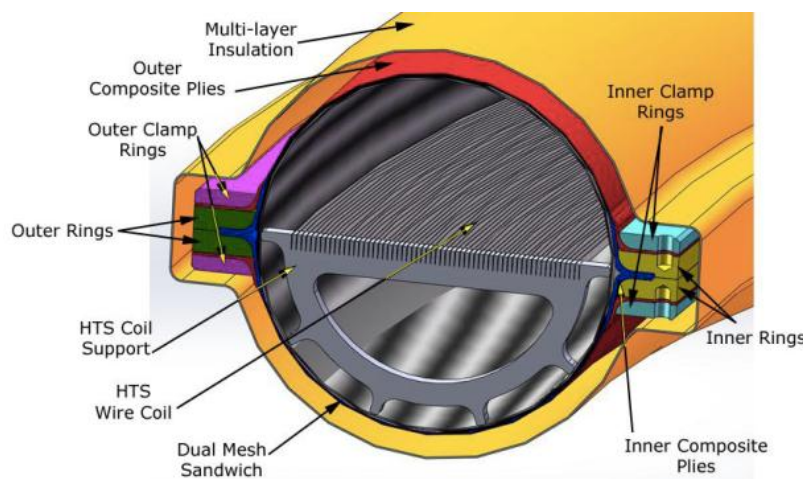
Figure 9: Two-part composite heatpipe showing an HTS coil inside

The cryogenic heatpipe, about two meters in diameter with 100 turns of HTS coil within its 4cm pipe diameter, was designed with a heat capacity of 100W (determined from the measured radiated heat input from the vacuum chamber walls) and succeeded in keeping the HTS coil below its critical temperature of 110K. The mass of the 2m diameter copper pipe was approximately 70.5 grams.   In LEO, however, the worst-case heat capacity of a 1 meter diameter MLI-coated coil (the size used in the EMFF testbed) is 5W [11]. 5W of heat can be extracted using a relatively low-mass (2.1 kg) cryocooler like the Sunpower CryoTel MT [18].

2.3   Technology readiness

HTS structures are a logical evolution of the previously realized or studied applications of electromagnets in space, and they bridge the gap between electromagnetic actuation, support, and positioning as a system that is capable of all three functions. In the future, spacecraft designers can tie together many of these positioning and actuation applications into a single or collection of multiple spacecraft, utilizing formation flying, easy in-situ assembly, isolation and high stowed-to-deployed size ratio structures to enable spacecraft that have never before been possible. Therefore, in this report, we will address several of the questions relevant to the feasibility and viability of implementing HTS structures through modeling and trade analysis. Furthermore, a goal of this work is to mature the technology readiness level (TRL) of HTS structures from conceptualization and early analysis of this application (TRL 2) to a more detailed analysis and hardware proof-of-concepts (TRL 3). Phase I encompasses the transition from TRL 2 to early 3 while our Phase II work aims to mature the technology further through TRL 3.

3   Chapter 3 – Theoretical Approach

This chapter will detail the equations of motion that describe the dynamical evolution of current-carrying coils in space and how this motion was simulated using MATLAB and Simulink models. In this report, we will be primarily discussing the motion of two rigid coils under a variety of boundary constraints; we will briefly discuss the motion of flexible coils in this chapter with a more in-depth discussion and analysis reserved for our Phase II report. These particular models were selected because between the two of them, all seven functional configurations presented in Chapter 1 could be modeled given appropriate boundary conditions.

In general, any current-carrying coil will experience forces and torques due to other current-carrying coils and magnetic fields in the vicinity. One of the purposes of this work is to determine how the mutual evolution of a network of coils is dependent upon the initial positions and orientations of the coils and how that evolution can be controlled for deployment and subsequent support purposes by imposing various constraints upon them, such as flexible tethers and hinges. Accurate models of coil dynamics can be used to characterize the range of system parameters over which electromagnetic structures are potentially useful. In this chapter, these models and the methods used in their construction will be introduced for use in studying the ranges over which each of the functional configurations is feasible.

3.1   Dynamics of unrestrained coils

The coil dynamics can be described fully by Newton's laws of motion. Newton's 2nd law will be employed in both its rectilinear form, for modeling the motion of the center of mass of the coil, and in its angular form, in order to describe the rigid body rotation of the coils through space. Newton's laws are first supplemented with the appropriate electromagnetic laws introduced in Chapter 2 to describe the electromagnetic forces and torques exerted on each coil by one another in a six degree-of-freedom model and later with mechanical forces that reflect the influence of constraining devices (tethers and hinges) on the coils.

3.1.1   Rectilinear motion

Consider a set of current loops, one of which we label by the subscript i, where i = 1,2,…, N, with N being the number of coils in our system. The magnitude of the current in coil i is given by I_i. At some point P in space (defined with respect to a suitably-chosen inertial coordinate system), the magnetic field due to a directed, differential coil element $d\vec{l}_i$ is given by Ampere's law:

$$d\vec{B}_i = \frac{\mu I_i}{4\pi} \frac{d\vec{l}_i \times \vec{r}_{Pi}}{|\vec{r}_{Pi}|^3}$$

where $\vec{r}_{Pi} \equiv \vec{r}_i - \vec{r}_P$ is the vector from P to the differential coil element, $d\vec{l}_i$ is the vector between two infinitesimally close points on the current loop, and μ is the magnetic constant, equal to 1.26×10^{-6} T·m /A.

The total magnetic field at *P* due to coil *i* is given by the integral over the entire loop, or:

$$\vec{B}_i = \oint_{\text{Loop } i} \frac{\mu I_i}{4\pi} \frac{d\vec{l}_i \times \vec{r}_{Pi}}{|\vec{r}_{Pi}|^3}$$

Now, suppose *P* happens to be on another current loop (denoted "*j*"), with the magnitude of its current given by I_j. Let the differential coil element at *P* be given by $d\vec{l}_j$; then, by the Lorentz law, the force exerted on this differential coil element by the magnetic field due to coil *i* is given by:

$$d\vec{F}_j = I_j d\vec{l}_j \times \vec{B}_i$$

$$= I_j d\vec{l}_j \times \oint_{\text{Loop } i} \frac{\mu I_i}{4\pi} \frac{d\vec{l}_i \times \vec{r}_{ji}}{|\vec{r}_{ji}|^3}$$

where $\vec{r}_{ij}$ has been rewritten from $\vec{r}_{iP}$ to emphasize that the magnetic field from coil *i* is acting to create a force on the differential coil element $d\vec{l}_j$. I_i and I_j are constant values around the current loop, and in cases in which each coil is made up of wire turned multiple times, if n_i is the number of turns in the *i*th coil, we may define an effective current $I_{eff,i}$ as follows:

$$I_{eff,i} \equiv n_i I_i$$

The total force exerted on coil *j* by coil *i* is then given by integrating the Lorentz force over coil *j*:

$$\vec{F}_j = \frac{\mu I_{eff,i} I_{eff,j}}{4\pi} \oint_{\text{Loop } j} d\vec{l}_j \times \oint_{\text{Loop } i} \frac{d\vec{l}_i \times \vec{r}_{ji}}{|\vec{r}_{ji}|^3}$$

By Newton's 2nd and 3rd laws, the force $\vec{F}_i$ acting on coil *i* from coil *j* is given by

$$\vec{F}_i = -\vec{F}_j = m_i \vec{a}_i,$$

these forces acting on the centers of mass of each coil. For a system with more than two coils, the force is equal to the summation of the contributions from each of the *N*-1 other coils (*N*-1 instead of *N* because the self-contribution of force from coil *j* is 0).

Since a coil responding to the magnetic fields of other coils will move and rotate, the vector variables of current element direction and position in the above equation change with time for each coil in the system. As such, the delay in the response of a given coil due to the finite propagation speed of electromagnetic waves must be taken into account. In our case, however, so long as we are interested in time scales much greater than $|\vec{r}_{ij}|/c$, where *c* is the speed of light (3×10^8 m/s), the effect of the delay will be negligible.

By denoting the position of the center of mass of the *j*th coil in the inertial coordinate system by an overbar, $\bar{r}_j$, we have:

$$\vec{F}_j = m_j \frac{d^2 \bar{r}_j}{dt^2}$$

$$= \sum_{\substack{j=1 \\ j \neq i}}^{N} \frac{\mu I_{eff,i} I_{eff,j}}{4\pi} \oint_{\text{Loop } j} d\vec{l}_j \times \oint_{\text{Loop } i} \frac{d\vec{l}_i \times \vec{r}_{ji}}{\left| \vec{r}_{ji} \right|^3}$$

There is no clean analytical solution for this problem besides the above double integral. For an axially symmetric coil, however, the magnetic field at a point *P* along the axis of symmetry out of the plane of the coil has the analytical solution:

$$\left| \vec{B} \right| = \frac{\mu n I R^2}{2 \left(R^2 + x^2 \right)^{3/2}}$$

where $\vec{B}$ is calculated in Tesla, *R* is the coil radius in meters, *I* is the current in amps, *n* is the number of turns of wire in the coil, and *x* is the distance in meters along the axis from the center of the coil. This solution is useful for calculating the force on a single particle along the coil's axis, but not for the force at any other point. Therefore, a numerical approximation of the force between the coils is required in order to study the behavior of the coils over time, accomplished by numerically performing the line integrals above. In this report, we investigate the dynamics of the coils using numerical models constructed in MATLAB and Simulink.

3.1.2   Rigid body dynamics and rotation

In addition to the translational, rectilinear motion of two coils in space, the torque and resultant rotation induced by asymmetric forces on differential elements across the coil must be taken into account.

By the force expressions given above, the torque exerted on the *i*th coil about its center of mass is given by:

$$\vec{\tau}_i = \sum_{\substack{j=1 \\ j \neq i}}^{N} \frac{\mu I_{eff,i} I_{eff,j}}{4\pi} \oint_{\text{Loop } i} (\vec{r}_i - \bar{r}_i) \times d\vec{l}_i \times \oint_{\text{Loop } j} \frac{d\vec{l}_j \times \vec{r}_{ij}}{\left| \vec{r}_{ij} \right|^3}$$

where $\vec{r}_i$ is the location of the differential element $d\vec{l}_i$ with respect to the global inertial coordinate system, and $(\vec{r}_i - \bar{r}_i)$ is the vector from differential element $d\vec{l}_i$ to the center of the coil, providing the moment arm of the torque formulation.

As with any analysis of rigid body motion, care must be taken in how the orientation of each body (in this case, the individual coils) is parameterized. In this report, the orientation of the coils in space is parameterized by means of a quaternion.

The use of quaternions to describe the orientation of a body in space is well established—for a full account of the theory, the reader is referred to, e.g. [19]. We describe the approach in relation to coil dynamics briefly:

We attach a coordinate system (called the body coordinate system and denoted $\{X_B^{(i)}\}$) to the ith coil. The orientation of this coordinate system is encoded within the quaternion $\vec{q}_i$ via the direction cosines matrix A_i, which specifies the coordinates of $\{X_B^{(i)}\}$ with respect to a suitably chosen global inertial coordinate system.

The matrix A_i, when multiplied to the right by the set of vectors that define the positions of the points around the coil around its center, effects the appropriate rotation upon the coil. The dynamical response of the coils is calculated using Newton's 2nd law in angular form, or

$$\vec{\tau}_i = [I]_i \vec{\alpha}_i$$

Here, $[I]_i$ is the moment of inertia matrix of the ith coil calculated with respect to its center of mass, given by:

$$[I]_i = \begin{bmatrix} \dfrac{m_i R_i}{2} & 0 & 0 \\ 0 & \dfrac{m_i R_i}{2} & 0 \\ 0 & 0 & m_i R_i \end{bmatrix}$$

We have chosen $\{X_B^{(i)}\}$ so that it is aligned with the principal axes of the coil; the third entry in the diagonal of $[I]_i$ corresponds with the axis normal to the plane of the coil. The angular acceleration of the body is $\vec{\alpha}_i$. From this, the evolution of the quaternion—and the orientation of the coil—can be advanced accordingly. [19]

3.2   Incorporation of constraining elements

The equations of motion presented above are for coils in empty space. Ultimately, mechanical elements (possibly in conjunction with appropriate current controllers for the coils) must be employed in order to execute desired geometrical configurations of the coils in space. The coils and these constraining elements will then serve as the primary structure of the spacecraft. Below, we describe incorporation of such constraints into the equations of motion.

3.2.1   Tethers

For the Separate functional configuration, the use of tethers to connect magnetic coils to each other and restrict their motion eliminates the need to control currents in order to keep coils positioned the desired distances from one another, as they would have to be in electromagnetic formation flight. Tethers also reduce the risk associated with two or more coils accelerating away from each other during deployment. This risk reduction is performed via the tethers providing a corrective "spring" force for any overshoot of the desired separation distance. In this report, three tethers equally spaced around the perimeter of the coils are used to restrict the motion of the coils, as shown in Figure 10. In future work, we will consider more complex tether configurations.

Figure 10: Diagram of 3-tether spacing between two coils
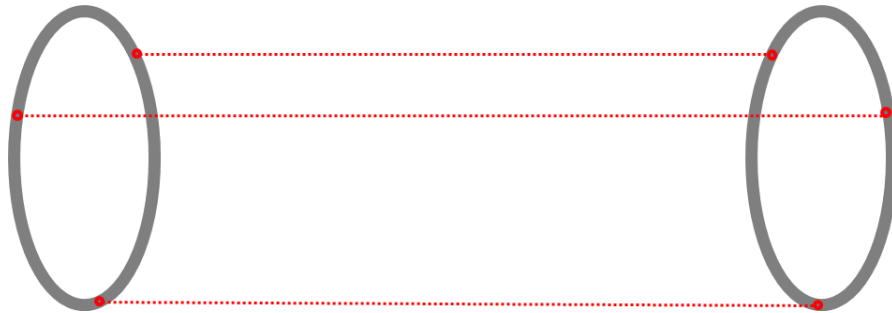
Three tethers are used instead of two because two tethers do not restrict the rotation of the coil around the axis drawn through the tether attachments (visualized in Figure 11), which could lead to a 180 degree flip of one or both coils once the tethers reach their full length during deployment.

Figure 11: Diagram of 2-tether spacing and unrestricted motion

In the Separate deployment, the coils start close to one another with tethers slack, as shown in Figure 12. Suppose the coils are aligned along their central axes, and the tethers—all identical to one another—are parallel to these axes. Once current is run through the coils in opposing directions, the coils begin to accelerate away from each other until the coils are L_t apart, where L_t is the unstretched length of a tether. If the tethers are stretched to a length $L > L_t$, an elastic force due to the tension of the tethers is effected. If we define $\Delta L \equiv L - L_t$, then the elastic force of a single tether on a given coil is $\left|\vec{F}_{elast,tether}\right| = k\Delta L$, where k is the spring constant of the tether with the force directed towards the other coil. If there are three equal length and material tethers, then the total elastic force acting on a coil is $\left|\vec{F}_{elast}\right| = 3k\Delta L$. In this model, the tethers are not rigid and do not provide compressive forces for distances shorter than L_t.
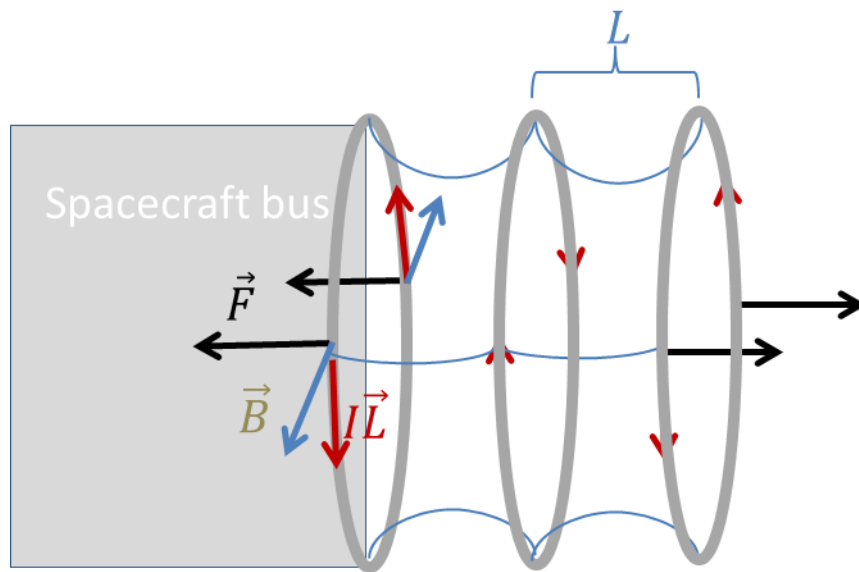
Figure 12: Three coil Separate configuration with slack tethers

Thus, in a two coil system with three identical tethers, when $L < L_t$, the forces acting on the coils are solely to due to electromagnetic interaction, while, when $L \geq L_t$, the forces acting on the coils will be due to both electromagnetic interactions and elasticity, the magnitude of the elastic force given by $3k\Delta L$.

In the more general case of coils and tethers not aligned, the effect of the tethers on the coils may be determined as follows. Let the three tethers be indexed by α = 1,2,3. Each tether has a natural length $L_{t,\alpha}$ beyond which, when stretched, a restorative elastic force results. If the length of the tether is less than this, the tether will slacken and not exert any force in the opposite direction. Let the tethers have elastic constants given by k_α. If the distance between the endpoints of the tether is given by L_α, the magnitude of the elastic force due to tether α is given by:

$$\left|\vec{F}_\alpha\right| = k_\alpha \Delta L_\alpha H_\alpha$$

where

$$\Delta L_\alpha \equiv L_\alpha - L_{t,\alpha}$$

and

$$H_\alpha = \begin{cases} 1 \text{ if } \Delta L_\alpha > 0 \\ 0 \text{ if } \Delta L_\alpha < 0 \end{cases}$$

To determine the directions in which each force acts, we consider the case in which the tethers are between only two coils. The tethers are attached to individual points on the coils. For tether α, let the vector describing the point of attachment on coil 1 be given by $\vec{P}_\alpha^{(1)}$, while the point of attachment on coil 2 is given by $\vec{P}_\alpha^{(2)}$. Thus, it is clear that:

$$L_\alpha = |\vec{P}_\alpha^{(1)} - \vec{P}_\alpha^{(2)}|$$

while the unit vector $\hat{P}_{elast,\alpha}$ parallel to the elastic force due to tether α is given by:

$$\hat{P}_{elast,\alpha} = \frac{\vec{P}_\alpha^{(1)} - \vec{P}_\alpha^{(2)}}{|\vec{P}_\alpha^{(1)} - \vec{P}_\alpha^{(2)}|}$$

With these definitions, we can write

$$\vec{F}_\alpha^{(1)} = -k_\alpha \Delta L_\alpha H_\alpha \hat{P}_{elast,\alpha}$$
$$\vec{F}_\alpha^{(2)} = k_\alpha \Delta L_\alpha H_\alpha \hat{P}_{elast,\alpha}$$

where $\vec{F}_\alpha^{(1)}$ is the force due to tether α exerted on coil 1 and $\vec{F}_\alpha^{(2)}$ is the force due to tether α exerted on coil 2. The total force on each coil is then simply

$$\vec{F}_{Elast}^{(1)} = \sum_{\alpha=1}^{3} \vec{F}_\alpha^{(1)}$$
$$\vec{F}_{Elast}^{(2)} = -\vec{F}_{Elast}^{(1)}$$

Now, the tethers will also effect torques upon the coils. If we wish to determine the torques about centers of mass of each coil due to tether α, we simply take the moment of the elastic force with respect to the coil center of mass:

$$\vec{\tau}^{(1)}_{O,\alpha,Elast} = -k_\alpha \Delta L_\alpha H_\alpha \left[\left(\vec{P}^{(1)}_\alpha - \bar{r}_1 \right) \times \hat{P}_{elast,\alpha} \right]$$
$$\vec{\tau}^{(2)}_{O,\alpha,Elast} = k_\alpha \Delta L_\alpha H_\alpha \left[\left(\vec{P}^{(2)}_\alpha - \bar{r}_2 \right) \times \hat{P}_{elast,\alpha} \right]$$

Thus, the total torque exerted by the tethers on each coil is given by

$$\vec{\tau}^{(1)}_{O,Elast} = \sum_{\alpha=1}^{3} \vec{\tau}^{(1)}_{O,\alpha,Elast}$$
$$\vec{\tau}^{(2)}_{O,Elast} = \sum_{\alpha=1}^{3} \vec{\tau}^{(2)}_{O,\alpha,Elast}$$

One concern with this deployment strategy is that oscillations of the coils will occur around the equilibrium length of the tether. Potential solutions to avoid or damp out oscillations include a current controller that reduces and even switches the direction of current in the coils such that the coils experience an attractive force (i.e. a force in the opposite direction of their deployment motion) and are thus slowed to a stop as they reach the equilibrium length L_{eq}. In this report, we do not explore a controlled method of damping in detail.

Because any realistic tether will have intrinsic to it some damping due to friction between its constitutive materials. To account for this most generally, we would need to solve, simultaneously with those of the coils, the equations of motion of the tethers themselves. However, this is computationally intensive, requiring the additional solution of the three coupled partial differential equations (complete with tether-coil boundary conditions) of the elastic behavior of the tethers.

For simplicity, therefore, we use instead a model in which the damping forces exerted on the coils are a function of the velocities of the tether attachment points only, as in a classical mass-damper system. Thus, we consider the relative velocity $\vec{V}_\alpha$ of the two coil attachment points for tether α with respect to the inertial coordinate system:

$$\vec{V}_\alpha = \frac{d}{dt} \left[\vec{P}^{(1)}_\alpha - \vec{P}^{(2)}_\alpha \right]$$

The damping force is supposed proportional to this, the proportionality constant taken to be b_α. It can be shown, then, that:

$$\vec{F}^{(1)}_{\alpha,damp} = -b_\alpha |\vec{V}_\alpha| H_\alpha \left[\frac{\text{sign}(\vec{V}_\alpha)}{\sqrt{3}} \cdot \hat{P}_{elast,\alpha} \right] \hat{P}_{elast,\alpha}$$

$$\vec{F}^{(2)}_{\alpha,damp} = b_\alpha |\vec{V}_\alpha| H_\alpha \left[\frac{\text{sign}(\vec{V}_\alpha)}{\sqrt{3}} \cdot \hat{P}_{elast,\alpha} \right] \hat{P}_{elast,\alpha}$$

The total damping force acting on the coils is given by:

$$F^{(1)}_{damp} = \sum_{\alpha=1}^{3} \vec{F}^{(1)}_{\alpha,damp}$$

$$F^{(2)}_{damp} = -F^{(1)}_{damp}$$

The torques about the coil centers of mass due to damping from tether α are:

$$\vec{\tau}^{(1)}_{B,\alpha,Damp} = -b_\alpha |\vec{V}_\alpha| H_\alpha \left[\frac{\text{sign}(\vec{V}_\alpha)}{\sqrt{3}} \cdot \hat{P}_{elast,\alpha} \right] \left[\left(\vec{P}^{(1)}_\alpha - \bar{r}_1 \right) \times \hat{P}_{elast,\alpha} \right]$$

$$\vec{\tau}^{(2)}_{B,\alpha,Damp} = b_\alpha |\vec{V}_\alpha| H_\alpha \left[\frac{\text{sign}(\vec{V}_\alpha)}{\sqrt{3}} \cdot \hat{P}_{elast,\alpha} \right] \left[\left(\vec{P}^{(2)}_\alpha - \bar{r}_2 \right) \times \hat{P}_{elast,\alpha} \right]$$

where the *B* denotes that the torques are taken with respect to the center of mass of the coil body. The total damping torques given by:

$$\vec{\tau}^{(1)}_{B,Damp} = \sum_{\alpha=1}^{3} \vec{\tau}^{(1)}_{B,\alpha,Damp}$$

$$\vec{\tau}^{(2)}_{B,Damp} = \sum_{\alpha=1}^{3} \vec{\tau}^{(2)}_{B,\alpha,Damp}$$

Other options besides simple cable tethers attached at each end to a coil exist for the Separate deployment. Thin, rigid members with joints that lock open as the coils move apart in order to guarantee a fixed distance between the coils and reduce oscillations during deployment are also a possibility, though such constraints would be more massive and complex than simple tethers and thus less competitive in a design trade where mass is a driving parameter. The Separate coil configuration as modeled here is both a deployment and a support device; with rigid, locking members, it becomes purely a deployment device and thus loses the novelty of being able to perform two functions simultaneously. Another option, one that allows for Reconfiguration over the lifetime of the spacecraft, is tethers that can be reeled out from a spool or back in to change the unstretched length L_t.

3.2.2 Hinges

The other constrained structural configuration we shall consider is that in which two hinged panels are deployed by means of coil-generated forces. For the Unfold configuration, coils are embedded or otherwise attached to rigid panels aligned on one edge and connected with a hinge, with motion limited to rotation around that hinge. This configuration is useful for the deployment of solar panels or electronically steered radar arrays or other segmented flat structures. When current is run through the coils, the force that they exert on each other is converted to torque around the hinge, causing them to rotate towards one another for two currents in the same direction and away from each other for two currents in the opposite direction, as in Figure 13.
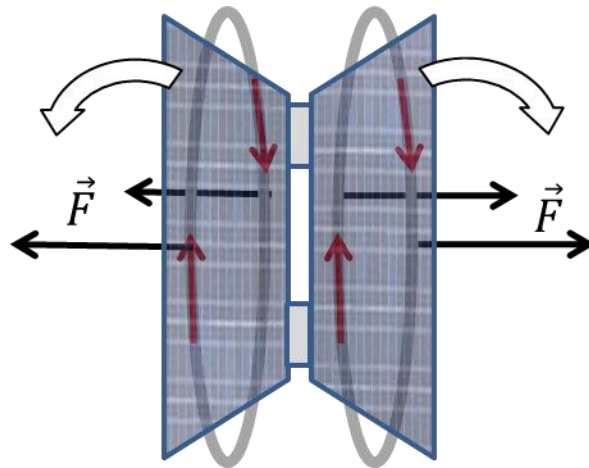
Figure 13: Two coils repelling each other across a hinge in Unfold configuration

In order for a hinged structure to deploy and maintain a predetermined equilibrium position, there must be a restorative force that opposes the coil driven separation. In practice, this will be accomplished by incorporating a torque spring or springs into the hinge about which the panels rotate.

Having a spring also supports Reconfiguration or Deformation of a structure operationally, since shutting off current through the coils allows the spring to pull the coils back together. Reconfiguration or Deformation is also possible by reversing the current in one coil in order to cause attraction between the coils.

Let us consider the torques about the hinge more in detail. Let the angles of the two panels around the hinge axis be given by θ_1 and θ_2. In the simplest case, if a torque spring is attached between the two panels, the spring torque is given by:

$$\left|\vec{\tau}_{spring}\right| = -\kappa\varDelta\theta$$

where κ is the torque spring constant, $\Delta\theta = \theta - \theta_0$, $\theta \equiv |\theta_1 - \theta_2|$ is the angle between the two panels, and θ_0 is the natural angle of the spring. These angles are depicted in Figure 14, with the panels to which the coils are attached represented by lines from the bases of the coils to the hinge.
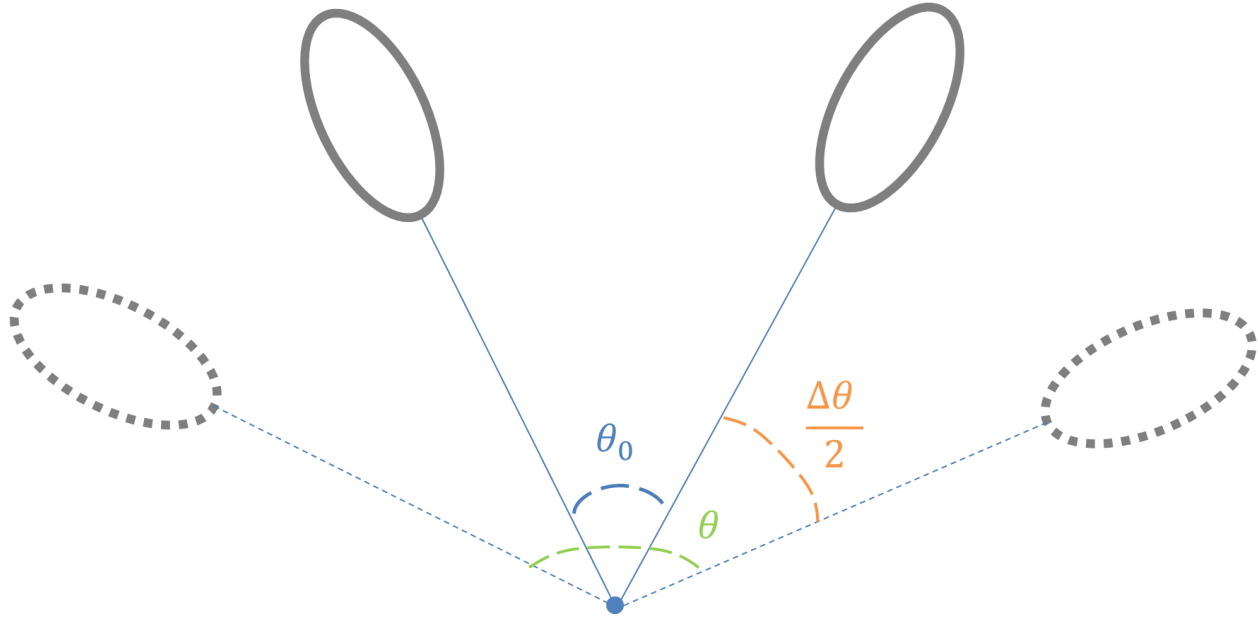
Figure 14: Hinge at equilibrium angle of spring and at stretched angle

Finally, in order to more effectively dampen any oscillations that occur about the equilibrium position, a rotational damping torque proportional to the angular velocity of the panels may be built into the hinge.

In considering more fully the dynamics of the coils about a hinge, we first make some assumptions:

1) The system comprises two panels, rotating about a hinge and in planes parallel to one another, with coils attached to each panel
2) The hinge is fixed with respect to some inertial coordinate system
3) The hinge is parallel to a unit vector which we denote $\hat{j}$
4) The coil is rigidly connected to the panel
5) The coils and the panels are all rigid members (a brief discussion of what happens when the panels are not completely rigid may be found below)

These assumptions allow us to directly formulate our equations of motion. Since the hinge is assumed fixed with respect to the inertial coordinate system, we may use the parallel axis theorem in determining the moment of inertia of the system (since there is only one degree of freedom per coil in this system, we do not need to calculate the entire moment of inertia matrix). Let the distance from the hinge axis to the center of each coil as mounted on the panel be given by $L_{m,i}$, and let the radius of each coil be given by R_i, $i = 1,2$. A coil rotating about an axis that passes through its diameter has a moment of inertia given by $m_i R_i^2/2$. The moment arm is given by $L_{m,i}$, so that, by the parallel axis theorem, the moment of inertia of the coil about the hinge axis is given by:

$$I_{coil,Hinge}^{(i)} = \frac{m_i R_i^2}{2} + m_i L_{m,i}^2$$

To get the moment of inertia of a single coil-panel construct, we must add to this the moment of inertia of the panel. Suppose the panel is rigid, rectangular, very thin compared to its length, and of mass $m_{panel,i}$. If it has a length of h_i,

$$I_{P,Hinge}^{(i)} = \frac{m_{panel,i} h_i^2}{3}$$

so that the moment of inertia $I_{hinge}^{(1)}$ about the hinge for a single coil-panel construct is:

$$I_{Hinge}^{(i)} = \frac{m_i R_i^2}{2} + m_i L_{m,i}^2 + \frac{m_{panel,i} h_i^2}{3}$$

Again, the dynamics of the hinge deployment as specified allow for one degree of freedom of motion for each of the two panels, parameterized as the angle of each panel with respect to some axis. Then, Newton's 2nd law can be written in angular form:

$$I_{Hinge}^{(1)} \frac{d^2\theta_1}{dt^2} \hat{j} = \sum \vec{\tau}_{Hinge,1}^{(1)}$$
$$I_{Hinge}^{(2)} \frac{d^2\theta_2}{dt^2} \hat{j} = \sum \vec{\tau}_{Hinge}^{(2)}$$

It remains to specify the torques acting on each panel. We will first consider the restorative torque applied to each panel counter to the moments due to electromagnetic force. These will be applied by torque springs about the hinge axis, and they may be implemented in one of two ways.

As mentioned above, the first way in which the torque spring may be implemented is by fixing it to each of the panels, so that the spring torque is a function of the difference in angle between the two panels, $\theta = |\theta_2 - \theta_1|$. Supposing the spring has a spring constant given by κ and an unstretched angle between its end connections of θ_0, the torque applied to each panel due to the spring will be given by:

$$\left.\begin{aligned}\vec{\tau}_{spring,1} &= \kappa(\theta - \theta_0)\hat{\jmath} \\ \vec{\tau}_{spring,2} &= -\kappa(\theta - \theta_0)\hat{\jmath}\end{aligned}\right\} \text{(Connected spring)}$$

One consequence of this method of implementing a torque spring is that if there is any kind of jerking motion of either coil, then the coils will both acquire a net rotation, executing a motion in which the line bisecting the two panels has a nonzero angular rate about the hinge axis (as in Figure 14). This is undesirable when deploying the panels to precise orientations with respect to inertial space is required. Nevertheless, it is favorable from the point of view of minimizing the number of possible variables in the system and in that it directly ties the motions of the two panels to one another, if the deployment action requires so.

As an alternative, we may consider the case in which each panel is attached to its own spring, each spring in turn connected to a structure that may be considered fixed. In this case, we have a spring constant for each panel, κ_1 and κ_2, and an unstretched angle for each, $\theta_{0,1}$ and $\theta_{0,2}$, so that the spring torques are given by

$$\left.\begin{aligned}\vec{\tau}^{(1)}_{spring} &= \kappa_1(\theta_1 - \theta_{0,1})\hat{\jmath} \\ \vec{\tau}^{(2)}_{spring} &= \kappa_2(\theta_2 - \theta_{0,2})\hat{\jmath}\end{aligned}\right\} \text{(Separate springs)}$$

The spring torques are now applied independently, but at the cost of having to determine additional parameters in order to implement a given equilibrium configuration. In this report, we will focus solely on implementing the first, connected, spring torques.

As mentioned, we may also incorporate damping torques into the motion of the panels. How we do so, however, depends on the nature of the hinge itself. If the hinge is made up of two separate elements, each attached to a panel and rotating about an axle not connected to either, then the damping force will be proportional to the angular velocity of each panel independently about the axis:

$$\left.\begin{aligned}\vec{\tau}_{damp,1} &= -\beta\dot{\theta}_1\hat{\jmath} \\ \vec{\tau}_{damp,2} &= -\beta\dot{\theta}_2\hat{\jmath}\end{aligned}\right\} \text{(Separate hinge elements)}$$

where β is the damping constant for the torque damping. If, however, the hinge is such that one element rotates about the other, then the damping torque will be a function of the difference in angular rates of each panel:

$$\left.\begin{aligned}\vec{\tau}_{damp}^{(1)} &= \beta(\dot{\theta}_1 - \dot{\theta}_2)\hat{\jmath} \\ \vec{\tau}_{damp}^{(2)} &= -\beta(\dot{\theta}_1 - \dot{\theta}_2)\hat{\jmath}\end{aligned}\right\} \text{ (Connected hinge elements)}$$

In this report we consider the hinge assembly to be made of separate hinge elements as in the first formulation.

It remains to determine what the torques about the hinge axis are due to electromagnetic interactions between the coils. If we designate the meeting point of the panels and the hinge as the *y*-axis through the origin of the inertial coordinate system, then we have

$$\vec{\tau}_{Hinge}^{(1)} = \frac{\mu I_{eff,1} I_{eff,2}}{4\pi} \oint_{\text{Loop 1}} \vec{r}_1 \times d\vec{l}_1 \times \oint_{\text{Loop 2}} \frac{d\vec{l}_2 \times \vec{r}_{12}}{|\vec{r}_{12}|^3}$$

$$\vec{\tau}_{Hinge}^{(2)} = \frac{\mu I_{eff,1} I_{eff,2}}{4\pi} \oint_{\text{Loop 2}} \vec{r}_2 \times d\vec{l}_2 \times \oint_{\text{Loop 1}} \frac{d\vec{l}_1 \times \vec{r}_{21}}{|\vec{r}_{21}|^3}$$

where $\vec{r}_1$ is the distance from the origin to a point on coil 1, $\vec{r}_2$ is the distance from the origin to a point on coil 2, and $\vec{r}_{12} = \vec{r}_2 - \vec{r}_1$. The resulting torque will be in a direction parallel to the hinge axis.

3.3   Dynamic model implementation

The equations of motion shown above were implemented and validated in MATLAB using a combination of built-in MATLAB functions, MathWorks' Simulink tool, and a number of custom-written scripts.

Generally, dynamics involving the full Biot-Savart force law were computed in Simulink (which allows considerably for the incorporation of custom scripts), while those implementing the dipole force law were computed using the built-in ode45 solver. In the former case, the need to numerically compute the line integrals and resulting forces and torques about the coils necessitated the development of custom scripts, while in the latter case, analytical forms for the force and moment equations lent themselves to calculation using one of MATLAB's robust ordinary differential equation solvers.

3.3.1   General solution algorithm

The two-coil model was constructed for use in studying the actuation of circular, magnetic coils modeled as *rigid*, or unchanged from their circular state in the process of actuation. This model applies to the Unfold, and Separate deployment configurations and the Deform, Reconfigure, and Refocus operational configurations, all shown in Figure 15. Though this report focuses on two-coil systems, the model could be expanded to include three or more coils, which would enable study of the Inflate configuration.
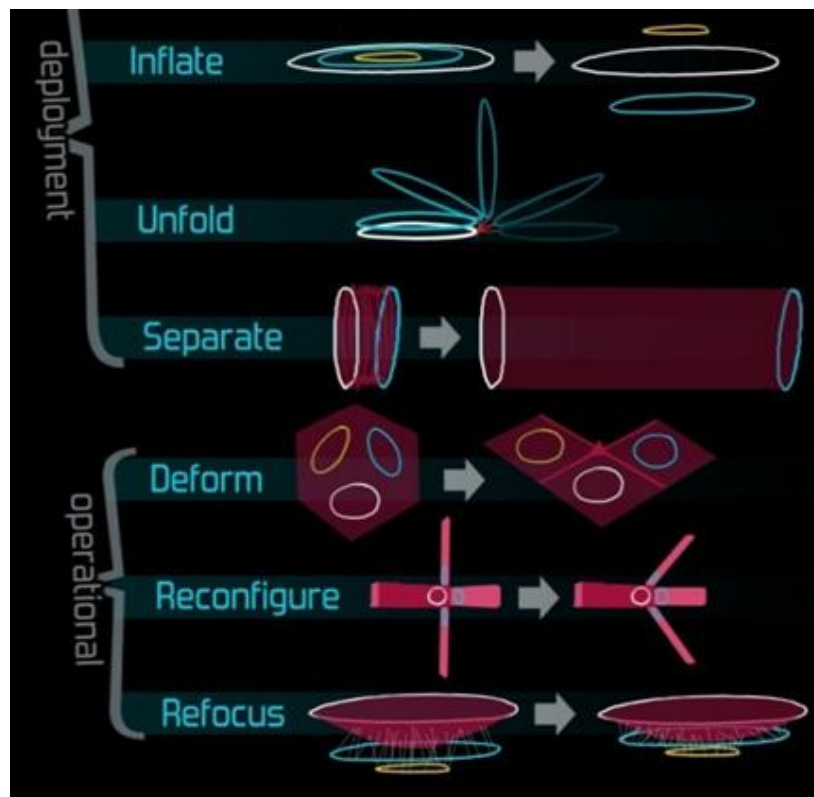

Figure 15: Rigid coil functional configurations

Below, we detail the steps taken in solution of the general equations of motion:

- The model begins by defining the positions of φ evenly spaced points around each of two coils with respect to a global coordinate origin and assigns values for current ($I_{1,2}$), wire cross-sectional area, wire density per unit length ρ, radii of the coils ($R_{1,2}$), and the moments of inertia of each ring ($[I]_{1,2}$).
- At each timestep, the force and torque on each coil as a result of the magnetic field of the other coil must be calculated. This is done using a double for-loop that calculates the force and torque on each point around Coil 1 from every point on Coil 2 (and vice versa), summing the contributions on one point from Coil 2 and then summing all the resultant forces and torques around Coil 1 for a final force and torque value on the coil at that timestep. The resultant forces and torques are multiplied after the loops end by the currents and appropriate constants to complete the Biot-Savart equation and calculation of Laplace force.
- Accelerations of the centers of mass are calculated by dividing the resultant electromagnetic force ($\vec{F}_{12}$),) by the masses of the coils.
- The positions of the coils are updated using the position and the velocity from the previous timestep.
- To determine the rotation on the coil about its center of mass, the torques (one for each coil) are projected onto the local axes $\{X_B\}$ of the coils. The angular velocities, quaternions and direction cosines matrices are calculated from the torques, and the orientation of the coils in space are updated accordingly.
- Plot new location and repeat in next time step.

3.3.2   Note on solution of stiff equations

$\vec{F}_{elast}$ is dependent on ΔL and the time is discretized by timesteps of varying duration in the tether model discussed above. We see from the formula for $\vec{F}_{elast}$ that the larger k is, the larger the restorative $\vec{F}_{elast}$ force is for a certain ΔL. $\vec{F}_{elast}$ and the electromagnetic force $\vec{F}_{magnetic}$ act simultaneously over the course of a timestep Δt; as $\vec{F}_{magnetic}$ stretches the tether, $\vec{F}_{elast}$ is opposing this motion. The formula for $\vec{F}_{coil}$ when $L \geq L_t$ is very stiff when using most materials. The $\vec{F}_{magnetic}$ acting to accelerate the coils apart over a timestep Δt creates a ΔL that causes a $\vec{F}_{elast}$ that is much larger than the $\vec{F}_{magnetic}$ for all but the smallest ΔLs (and thus the smallest Δts are required for these two opposing forces to be of similar magnitudes and allow the model to converge to the approximation of continuous motion). A Simulink model utilizing the variable-timestep ode45 is used to reach the small Δts when $L \geq L_t$ and use larger Δts when $L < L_t$ for shorter overall run times.

3.4   Validation of numerical models

Validation of the numerical methods employed in solving the dynamical equations of the coils are carried out by comparing results in which the force law is governed by the Biot-Savart law with those in the dipole approximation.

Validation of the numerical approximation can be done via an approximation of the coils as magnetic dipoles at far-field distances. The far-field as discussed in this report is defined as the case in which the diameter D of each coil under consideration is much less than the distance between every pair of coils in the network:

$$D_{i,j} \ll |\vec{r}_{ij}|, \quad i,j = 1,2,\dots,N;$$

A more thorough discussion of what constitutes this limit follows below. While validation against an exact analytic solution is not possible in the near field, we demonstrate that both the behavior of the numerical model in the near field is consistent with its behavior in the far-field, and that the behavior of the numerical model in the far-field matches that of the dipole. Thus, the validation provides confidence in the accuracy of the model.

3.4.1   Analytic dipole model

Now, the forces exerted by two magnetic dipoles on each other are given by Schweighart [20]:

$$\vec{F}_j = \frac{3\mu}{4\pi}\left[\frac{\vec{m}_i \cdot \vec{m}_j}{r^5}\vec{r} + \frac{\vec{m}_i \cdot \vec{r}}{r^5}\vec{m}_j + \frac{\vec{m}_j \cdot \vec{r}}{r^5}\vec{m}_i - 5\frac{(\vec{m}_i \cdot \vec{r})(\vec{m}_j \cdot \vec{r})}{r^7}\vec{r}\right]$$

where $\vec{r}$ is the vector distance between the centers of the coils, μ is the magnetic constant, and $\vec{m}_1$ and $\vec{m}_2$ are the magnetic moments of each coil, defined by:

$$\begin{aligned}\vec{m}_i &= n_i I_i A_i \hat{n}_i \\ &= I_{eff,i}\, A_i \hat{n}_i\end{aligned}$$

n_i being the number of turns in coil i, I_i being the current, A_i the area enclosed by the loop, and $\hat{n}_i$ being the unit vector along the axis of the coil, oriented in the direction dictated by the right-hand rule following the current around the loop.

For two identical, coaxially-aligned coils with planes parallel to one another, the dipole force equation reduces to:

$$\vec{F} = \frac{3\mu}{2\pi} \frac{A_1 A_2 I_{eff,1} I_{eff,2}}{|\vec{r}_{12}|^4} \, \hat{r}_{12}$$

with $\hat{r}_{12}$ the unit vector in the direction of $\vec{r}_{12}$ towards the other coil. The above formula is multiplied by -1 if the currents are in opposite directions.

3.4.2   Sources of error in numerical approximation

There are two sources of error that contribute to the difference in force calculations between the numerical model and the far-field dipole approximation: 1) the discretization of the coils into straight line segments rather than a continuous curve, and 2) the distance between the coils. The errors resulting from these two sources decrease to zero as the number of line segments in the discretization or the distance between coils increases to infinity.

Discretization: When using the Biot-Savart force law, the number of calculations to determine the resultant force and torque on each coil due to the other's magnetic field is $O(\phi^2)$, with ϕ being the number of differential elements around the coil, making fine discretization of curved coils (though more accurate to the curve of the coil) computationally expensive when computing the electromagnetic force.

Distance: The numerical force falls off as $1/r^2$, and the dipole force falls off as $1/r^4$, so we expect for very small ($r < 1$) values that the dipole force dominates, but then the dipole force is much greater than the numerical force right after $r = 1$ and then the difference between the two calculated forces goes to zero as $r \to \infty$. A quick visualization of this trend is shown in Figure 16.
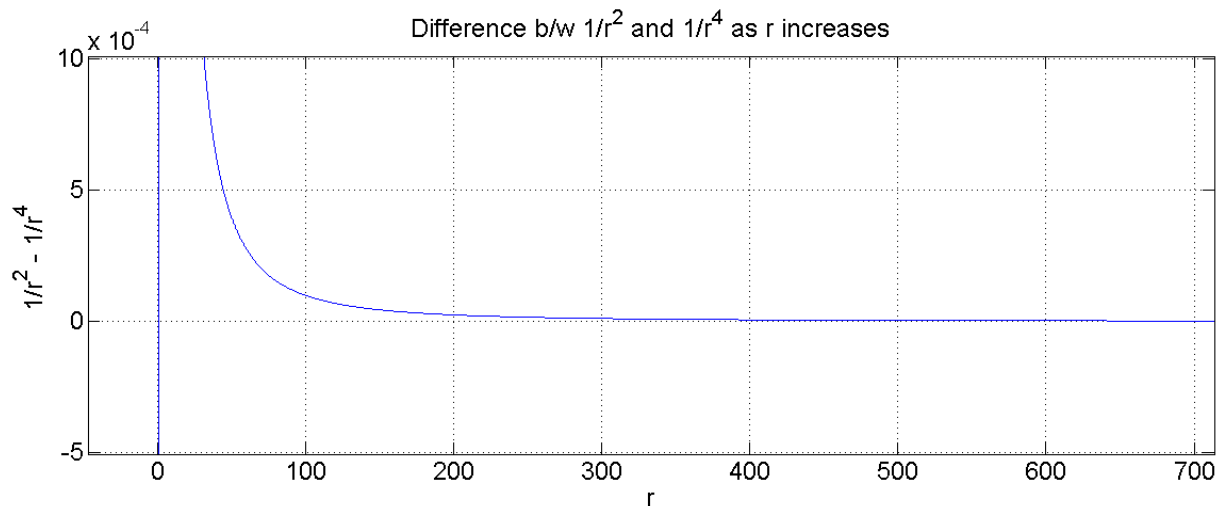
Figure 16: Proportional difference between numerical and dipole approximations

There is not a specific ratio of $D_{i,j}$ to r_{ij} at which the far-field approximation becomes valid; rather, one can determine what constitutes an acceptable percent error between the two. Figure 17 plots the initial force between a 1m diameter coil and a 0.98m diameter coil facing each other against the distance between them in both the numerical model and the dipole approximation, showing the convergence of the initial force values as the distance between the coils increases. The coils are slightly different sizes in order to avoid overlap of the coils in space for very small ($r_{ij} \ll 1$) distances.
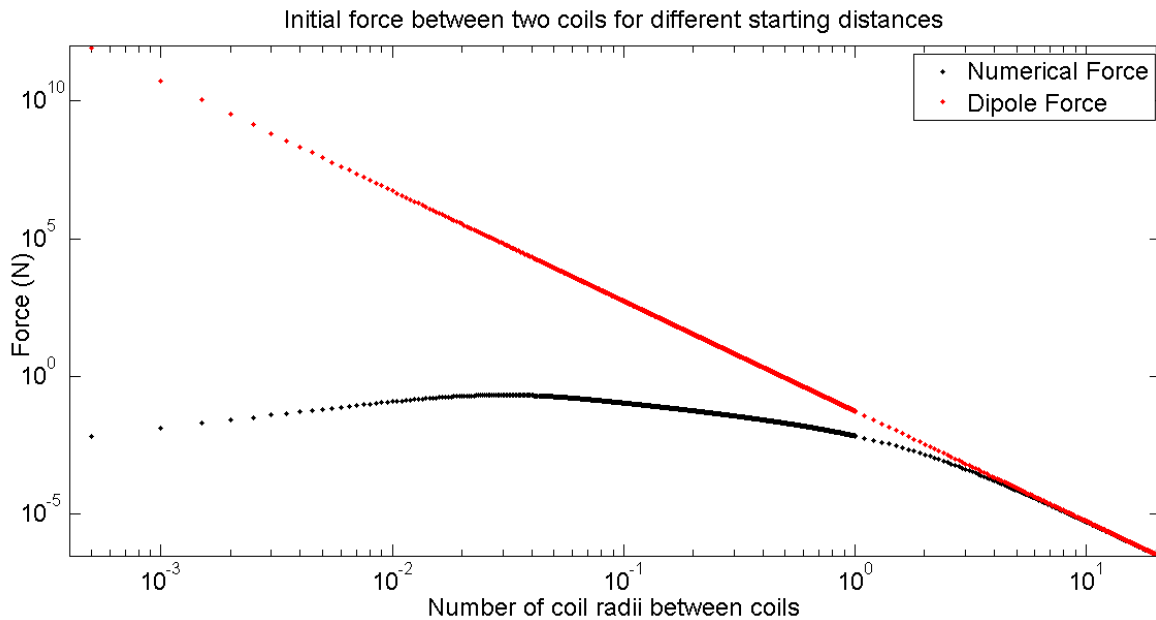
Figure 17: Comparison of numerical and dipole initial forces over a range of starting distances

Table 4 lists the error of the dipole force calculation compared to the numerical force calculation for distances that are various multiples of the coil radius.

Table 4: Error between numerical and dipole force calculations

Distance in coil radii	Error (%)
1	87.4
5.021	16.5
10.05	4.7
15.07	2.2
15.98	2.0
16.98	1.8
20	1.3

Assuming an acceptable error in force of 2%, we find from Figure 17 and Table 4 that the distance at which the far-field approximation becomes valid is ~16 times the coil radius, or $8D$. This activity validates that the six degree-of-freedom approach presented in this chapter converges to the dipole approximation as expected at distances far from each other. There is no equivalent validation of the approach for the near-field, so this far-field convergence must suffice. We emphasize that the purpose of validation is to verify the accuracy and performance of our numerical methods in calculating the Biot-Savart force (which is a well-known consequence of the Lorentz force law and Gauss's law and is valid at any distance between coils) and to make sure that it agrees with another valid calculation of electromagnetic force that does not require a numerical approximation to calculate, the dipole force. The fact that the dipole case only converges to the true Biot-Savart forces in the far-field does not affect the Biot-Savart formulation in the near field: if the models agree in the far-field, then the Biot-Savart formulation is correctly and closely approximating behavior in the near-field.

3.4.3   Validation models

Validation of the numerical code for coil dynamics consisted of comparing the simulation results for full dynamics (i.e. those governed by the Biot-Savart force law) with those in the dipole approximation in the appropriate distance limit. Ten different deployment configurations were used for validation purposes: 1) Axially-aligned coils with elastic tethers between them, 2) hinged coil-panel systems with torque springs attached. For axially-aligned coils, rigid body rotation is not expected to occur. Therefore, validation for the Separate configuration focused solely on the rectilinear motion of the coils. The equations of motion implemented in the validation models will be discussed below.

3.4.3.1   *Separate configuration*

For two axially aligned coils whose planes are parallel to one another, motion will exist (for either force model, dipole or numerical) in one direction. Thus, we may directly compare the axial separation of the two coils as a function of time; this will later serve to give an idea of what characteristic time scales are required deployment for various tether and coil sizes and, ultimately, for various load sizes.

The equations of motion in the Laplace force case are:

$$m_1 \frac{d^2\vec{r}_1}{dt^2} = \sum_{\alpha=1}^{3}\left[-k_\alpha \Delta L_\alpha H_\alpha \hat{P}_{elast,\alpha} + \vec{F}^{(1)}_{\alpha,damp}\right] + \frac{\mu I_{eff,1} I_{eff,2}}{4\pi} \oint_{\text{Loop 1}} d\vec{l}_1 \times \oint_{\text{Loop2}} \frac{d\vec{l}_2 \times \vec{r}_{12}}{|\vec{r}_{12}|^3}$$

$$m_2 \frac{d^2\vec{r}_2}{dt^2} = \sum_{\alpha=1}^{3}\left[k_\alpha \Delta L_\alpha H_\alpha \hat{P}_{elast,\alpha} + \vec{F}^{(2)}_{\alpha,damp}\right] + \frac{\mu I_{eff,1} I_{eff,2}}{4\pi} \oint_{\text{Loop 2}} d\vec{l}_2 \times \oint_{\text{Loop 1}} \frac{d\vec{l}_1 \times \vec{r}_{21}}{|\vec{r}_{21}|^3}$$

while in the dipole case, they are:

$$m_1 \frac{d^2\bar{r}_1}{dt^2} = \sum_{\alpha=1}^{3} \left[-k_\alpha \Delta L_\alpha H_\alpha \hat{P}_{elast,\alpha} + \vec{F}_{\alpha,damp}^{(1)} \right] + \frac{3\mu}{2\pi} \frac{A_1 A_2 I_{eff,1} I_{eff,2}}{|\vec{r}_{12}|^5} (\bar{r}_1 - \bar{r}_2)$$

$$m_2 \frac{d^2\bar{r}_2}{dt^2} = \sum_{\alpha=1}^{3} \left[k_\alpha \Delta L_\alpha H_\alpha \hat{P}_{elast,\alpha} + \vec{F}_{\alpha,damp}^{(2)} \right] - \frac{3\mu}{2\pi} \frac{A_1 A_2 I_{eff,1} I_{eff,2}}{|\vec{r}_{12}|^5} (\bar{r}_1 - \bar{r}_2)$$

3.4.3.2 Unfold configuration

In the hinge configuration, the equations of motion follow from the discussion above; for the Biot-Savart force law, we have:

$$I_{Hinge}^{(1)} \frac{d^2\theta_1}{dt^2} \hat{j} = \kappa(|\theta_2 - \theta_1| - \theta_0)\hat{j} - \beta\dot{\theta}_1\hat{j} + \hat{j} \cdot \left[\frac{\mu I_{eff,1} I_{eff,2}}{4\pi} \underbrace{\oint \vec{r}_1 \times d\vec{l}_1}_{\text{Loop 1}} \times \underbrace{\oint \frac{d\vec{l}_2 \times \vec{r}_{12}}{|\vec{r}_{12}|^3}}_{\text{Loop 2}} \right]$$

$$I_{Hinge}^{(2)} \frac{d^2\theta_2}{dt^2} \hat{j} = -\kappa(|\theta_2 - \theta_1| - \theta_0)\hat{j} - \beta\dot{\theta}_2\hat{j} + \hat{j} \cdot \left[\frac{\mu I_{eff,1} I_{eff,2}}{4\pi} \underbrace{\oint \vec{r}_2 \times d\vec{l}_2}_{\text{Loop 2}} \times \underbrace{\oint \frac{d\vec{l}_1 \times \vec{r}_{21}}{|\vec{r}_{21}|^3}}_{\text{Loop 1}} \right]$$

where $I_{Hinge}^{(1)}$ and $I_{Hinge}^{(2)}$ are defined as above. For symmetry and simplicity, the single torque spring model has been used.

For the dipole case, we consider only the situation in which each hinged panel is of the same length. Consider the expression for the force acting on the centers of each coil, again letting $\Delta\theta \equiv |\theta_1 - \theta_2|$ be the angle between the hinge panels, we have by the geometry:

$$|\vec{F}_{12}| = \frac{3\mu}{4\pi} \frac{I_{eff,1} I_{eff,2} A_1 A_2}{|\vec{r}_{12}|^4} [1 + \cos^2(\Delta\theta/2)],$$

the force acting along a line that passes through the centers of the coils. If we calculate the torque due to this force about the hinge, we find (recalling that the moment arm is of length L_m):

$$\vec{\tau}_{Hinge}^{(1)} = \frac{3\mu}{4\pi} \frac{I_{eff,1} I_{eff,2} A_1 A_2 L_m}{r_{12}^4} [1 + \cos^2(\Delta\theta/2)] \cos(\Delta\theta/2) \, \hat{j}$$

$$\vec{\tau}_{Hinge}^{(2)} = -\vec{\tau}_{Hinge}^{(1)}$$

Noting that $r_{12} = 2L_m \sin(\Delta\theta/2\,)$, we have, finally:

$$|\vec{F}_{12}| = \frac{3\mu}{64\pi} \frac{I_{eff,1} \, I_{eff,2} \, A_1 A_2}{L_m^{\,4}} \left[\frac{1 + \cos^2(\varDelta\theta/2)}{\sin^4(\varDelta\theta/2)}\right]$$

and

$$\vec{\tau}_{Hinge}^{(1)} = \frac{3\mu}{64\pi} \frac{I_{eff,1} \, I_{eff,2} \, A_1 A_2}{L_m^{\,3}} \left[\frac{1 + \cos^2(\varDelta\theta/2)}{\sin^3(\varDelta\theta/2)\tan(\varDelta\theta/2)}\right]\hat{\jmath}$$

$$\vec{\tau}_{Hinge}^{(2)} = -\vec{\tau}_{Hinge}^{(1)}$$

Thus, the corresponding dipole model equations of motion are:

$$I_{Hinge}^{(1)} \frac{d^2\theta_1}{dt^2}\hat{\jmath} = \kappa(|\theta_2 - \theta_1| - \theta_0)\hat{\jmath} - \beta\dot{\theta}_1\hat{\jmath} + \frac{3\mu}{64\pi}\frac{I_{eff,1} \, I_{eff,2} \, A_1 A_2}{L_m^{\,3}}\left[\frac{1 + \cos^2(\varDelta\theta/2)}{\sin^3(\varDelta\theta/2)\tan(\varDelta\theta/2)}\right]\hat{\jmath}$$

$$I_{Hinge}^{(2)} \frac{d^2\theta_2}{dt^2}\hat{\jmath} = -\kappa(|\theta_2 - \theta_1| - \theta_0)\hat{\jmath} - \beta\dot{\theta}_2\hat{\jmath} - \frac{3\mu}{64\pi}\frac{I_{eff,1} \, I_{eff,2} \, A_1 A_2}{L_m^{\,3}}\left[\frac{1 + \cos^2(\varDelta\theta/2)}{\sin^3(\varDelta\theta/2)\tan(\varDelta\theta/2)}\right]\hat{\jmath}$$

3.4.4　Validation results

The foregoing equations of motion for the Separate and Unfold configurations were solved for several variations of the physical parameters, and the dipole and numerical results compared. In the Separate case, the coils are both of radius 0.5 m. They begin, axially aligned, at a distance of 5.0 m, with the tethers having an unstretched length $L_t = 6$ m. The coil wires, assumed to have the density of copper, have a cross-sectional area of 10^{-4} m $\times$ 4×10^{-3} m $= 4 \times 10^{-7}$ m^2, have 90 turns, and current of 100 A running through them, which are typical values for industry standard HTS wire. [6] The baseline damping coefficient for a single tether is $b_0 = 2/3$ kg/s and the baseline single tether spring constant is $k_0 = 0.1$ N/m. The mass of a payload attached to each coil is 10 kg, which could include the weight of a cooling system for the coil or other apparatus.

In the Unfold configuration, the coils have the same radius, cross sectional area, number of turns, and current as in the Separate configuration. The baseline damping coefficient $\beta_0 = 60$ N $\cdot$ m $\cdot$ s/rad and the baseline torque spring constant is $\kappa_0 = 1$ N $\cdot$ m/rad. The moment arm of the coil $L_m = 10$ m, while the panel has a length of $h = 20$ m and a mass of $m_{panel} = 10$ kg. The spring has an unstretched angle of $\theta_0 = 45° = \pi/4$ rad, and the coils have an initial separation of $\theta_{init} = 45° = \pi/4$ rad. In both cases, the coils are discretized by $\phi = 17$ points; these baseline parameters are summarized in Table 5.

Table 5: Baseline values of physical parameters for simulation

| Variables	Symbol	Value
General		
Diameter	D	1 m (=2R)
Current through wire	I	100 A
# of turns	n	90
Effective current	I_{eff}	$I \times n = 9000$ A
Density per unit length of wire	ρ	$10^{-4}\text{m} \times 4 \times 10^{-3}\text{m} \times 894 \text{ kg/m}^3$ $= 3.58 \text{ kg/m}$
Discretization of coil	φ	17 points
Separate Configuration		
Initial distance between coil centers	d_{start}	5 m
Unstretched length of tethers	L_t	6 m
Tether damping coefficient	b_0	2/3 kg/s
Elasticity of tethers	k_0	0.1 N/m
Mass, payload	$m_{payload}$	10 kg
Mass, coil	m	$\rho \pi D + m_{payload} = 10.20$ kg
Unfold Configuration		
Initial angle between coils	θ_{init}	45° or $\pi/4$ rad
Unstretched angle of spring	θ_0	45° or $\pi/4$ rad
Torque damping coefficient	β_0	60 N $\cdot$ m $\cdot$ s/rad
Torsional spring constant	κ_0	1 N $\cdot$ m/rad
Mass of panel attached to coil	m_{panel}	10 kg
Length of panel	h	20 m
Hinge moment arm length	L_m	10 m

3.4.4.1 Tether validation
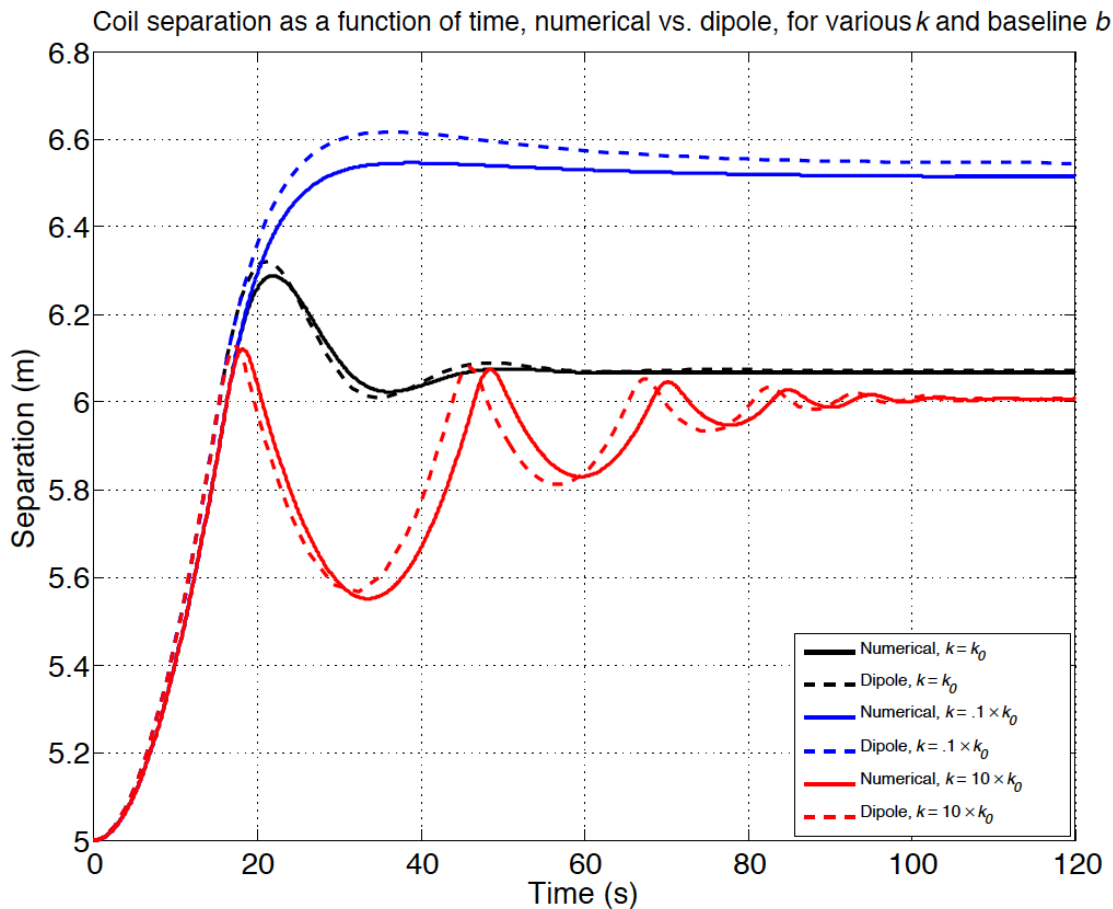
Figure 18: Coil separation as a function of time for Separate configuration. Spring constant is varied, while damping coefficient is kept at the baseline value.

In Figure 18, we see the effect of varying the spring constant *k* across all three tethers on the separation of the coils in the Separate configuration for both the numerical, Biot-Savart force law (solid line) and dipole approximation (dotted line). The differences between the numerical model and dipole calculations are consistent with the small errors predicted above in Section 3.4.2. For all cases, the agreement between the numerical force calculation and the dipole approximation responses is good, with the discrepancy primarily due to the fact that the dipole approximation tends to overestimate forces at shorter separations. Since the coils start ten coil radii apart, agreement is within a few percent.

The black lines show the response of the system as a function of time for the baseline case. Initially, the coils start 5 m apart, and they are accelerated away from one another by electromagnetic repulsion. After a separation of 6 m, which is the natural length of the tethers, elastic forces come into effect, and we see the coils begin to get pulled back while still being repelled from one another by the electromagnetic force. Ultimately, the motion is damped and reaches steady state after about 90 s.

The blue and red lines represent the response of the system for $k = .1 \times k_0$ and $k = 10 \times k_0$, respectively. For the lower k system, we see the diminished effect of the elastic forces manifest in both the lower oscillation amplitude during pullback, and in the larger steady state separation acquired by the system; steady state is reached at a later time than in the baseline case. For the larger k, we see increased oscillation amplitudes as expected, while again, steady state occurs at a later time than the baseline situation. We can therefore surmise that, for the given $b = b_0$, the baseline k represents something closer to a critically damped system than for the other two ks considered. For the higher k case, the steady state separation is smaller than the baseline case because the tethers are able to resist electromagnetic repulsive forces more effectively.

Coil separation as a function of time, numerical vs. dipole, for various b and baseline k
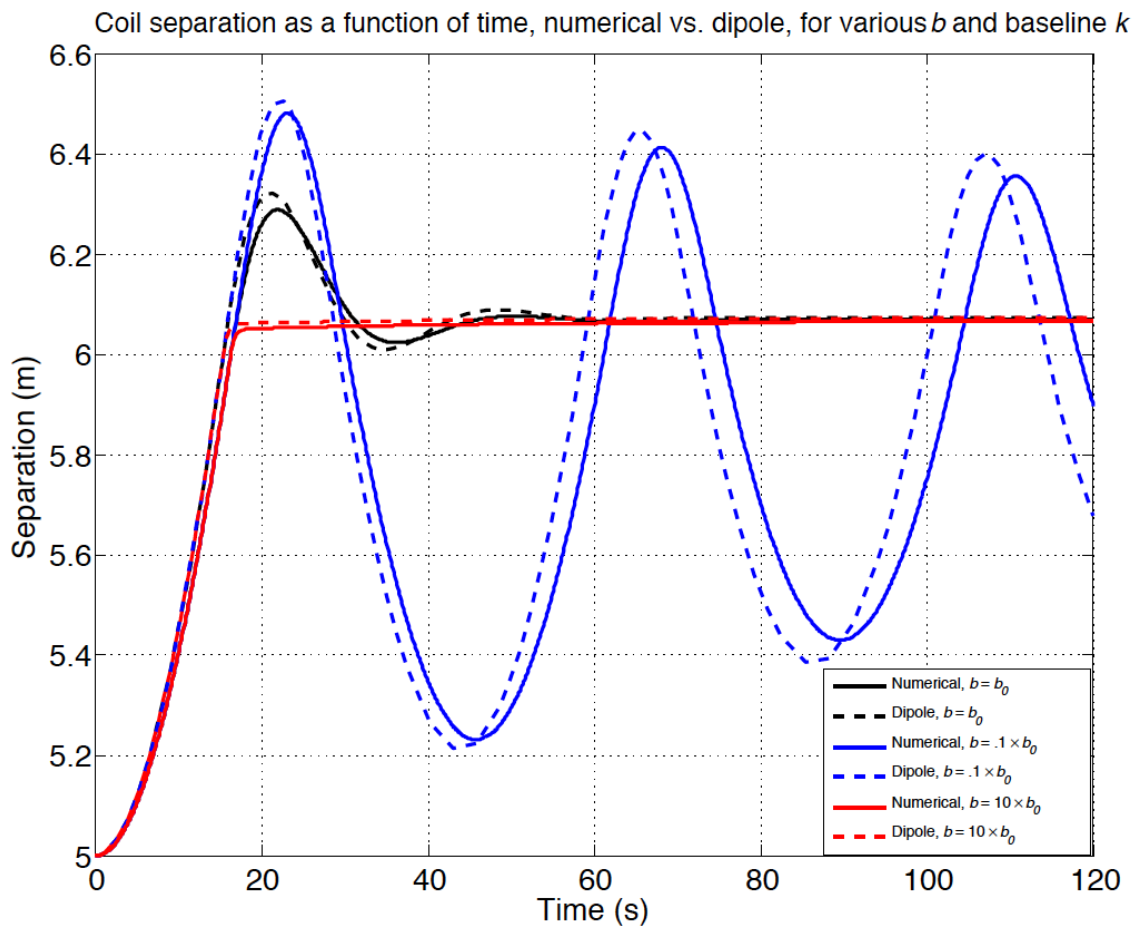
Figure 19: Coil separation as a function of time for Separate configuration. Damping coefficient is varied, while spring constant is kept at the baseline value.

In Figure 19, we see the response of the system with the spring constant for the tethers fixed at $k = k_0$, while b is varied. The black line represents the response of the system for baseline k and b values; this is the same response as that shown for the baseline case in Figure 18. Since k is not changed, the equilibrium value about which oscillations can occur is the same for all b values.

We see, for diminished b ($b = .1 \times b_0$; blue lines), that oscillations due to elastic forces (once again, coming into play once the separation is greater than 6 m) are less effectively damped than in the baseline case. For the larger, $b = 10 \times b_0$ case (red lines), we see that the system is close to being critically damped, if slightly overdamped. Nevertheless, the high b case reaches steady state slightly sooner than the baseline case. Again, qualitative agreement between the numerical and dipole cases is good.
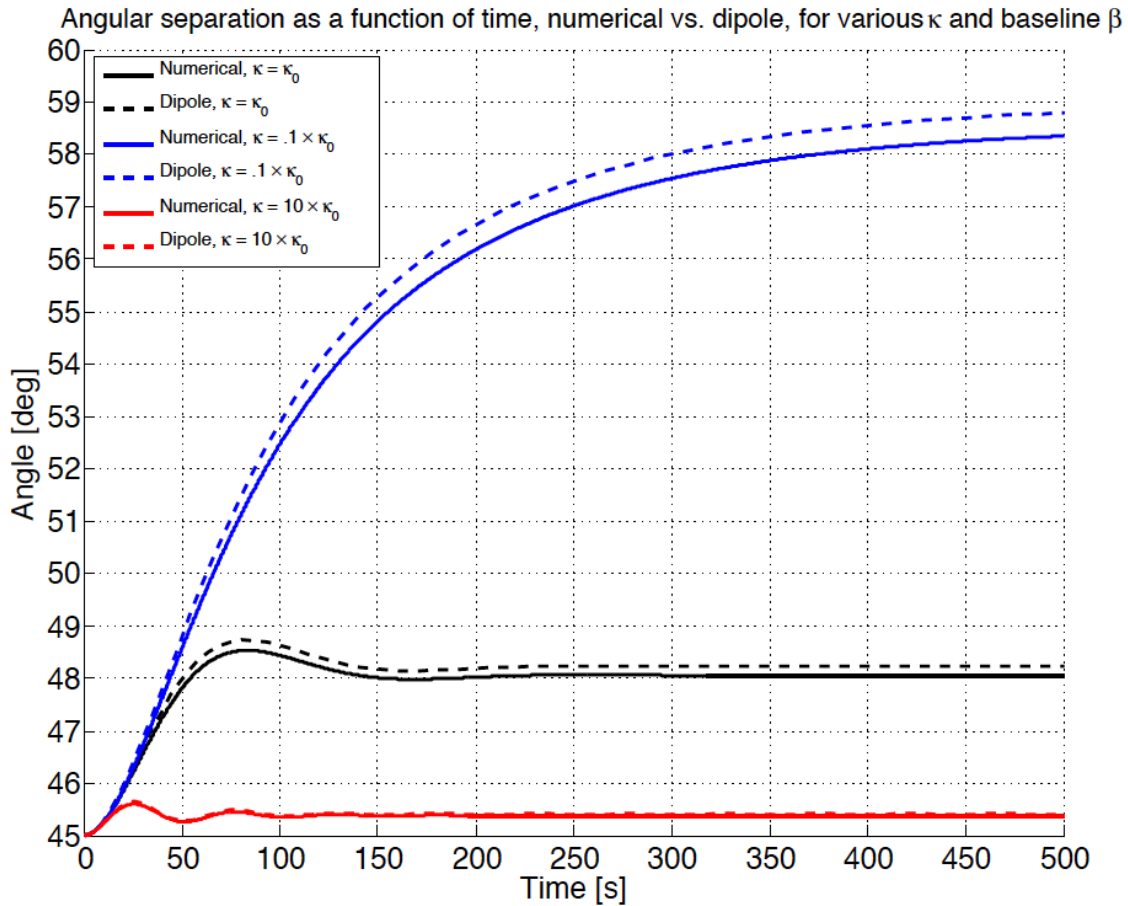
3.4.4.2 Hinge validation

Figure 20: Angular separation between hinge elements for the Unfold configuration. Hinge spring constant is varied, while torque damping coefficient is kept at the baseline value.

In Figure 20, we see the angular separation response for the Unfold configuration as a function of time. Again, the black lines are the response of the system for the baseline case, for both numerical (solid line) and dipole (dotted line) force calculations. We see that the coils execute about two cycles of oscillation before equilibrium is reached at an angle of about $48°$. For a lower torque spring constant $\kappa = .1 \times \kappa_0$ (blue lines), the system is comparatively overdamped for the given torque damping coefficient $\beta = \beta_0$. Subsequently, oscillations are nonexistent over the time period considered and steady state about a larger equilibrium separation is not acquired. On the other hand, for a larger torque spring constant $\kappa = 10 \times \kappa_0$ (red lines), we see a smaller equilibrium angle, due to the increased resistive capacity of the spring, and an increased number of oscillations before steady state is reached.
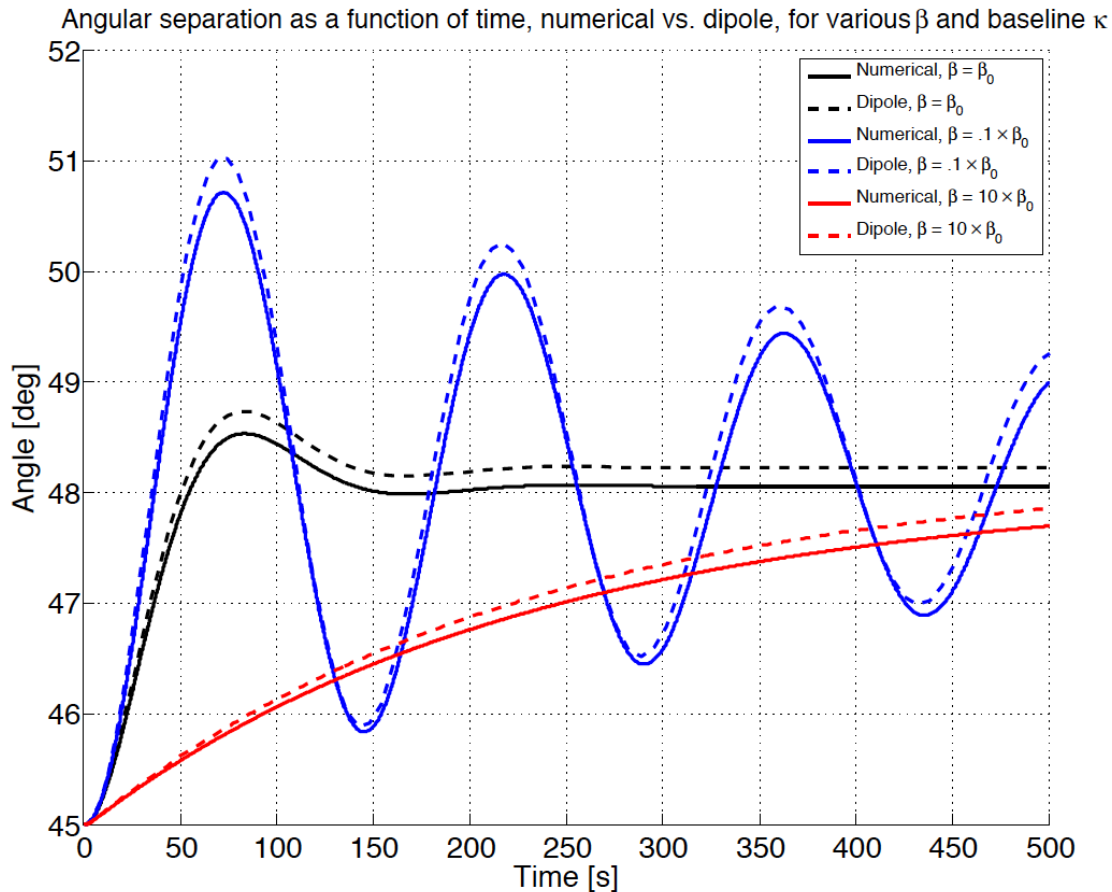
Figure 21: Angular separation between hinge elements for the Unfold configuration. Torque damping coefficient is varied, while hinge spring constant is held at the baseline value.

In Figure 21, we have the Unfold angular separation response for various torque damping coefficients β, with the torque spring constant fixed at $\kappa = \kappa_0$. Since κ is fixed, the steady state angular separation of the system does not change, so that motions are either about this steady state value (equal again to about $48°$) or asymptotic to it in an overdamped case. The baseline case (black) is the same as in Figure 20, while the response for a decreased damping coefficient $\beta = .1 \times \beta_0$ is shown in blue. We see an increase in oscillation cycles for a given time period over the baseline case due to the system being relatively underdamped, while by comparison, the $\beta = 10 \times \beta_0$ case is overdamped (red lines), not reaching the steady state angular separation and instead asymptotic to it.

3.4.4.3 Effect of discretization

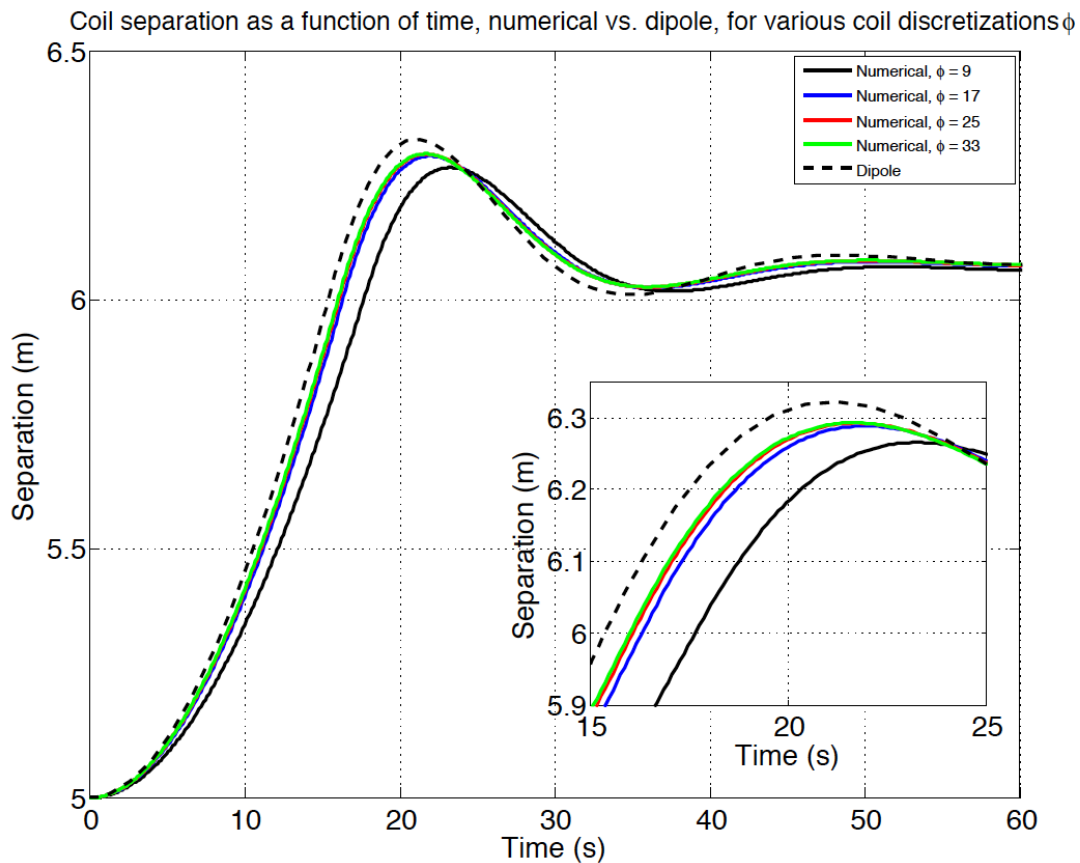**Figure 22: Effect of discretization on numerical calculations. Baseline tether case is calculated for Biot-Savart/numerical and dipole force laws, with the former approximated by increasingly finer discretizations ϕ. The inset shows the same, near the oscillation peak occurring around 20 s.**

In the previous sections, we investigated the response of the Separate and Unfold configurations as a function of time for both the dipole and Biot-Savart force laws. The numerical calculation of the latter depended upon the discretization ϕ of the coil, with ϕ the number of discrete points approximating the circular shape of the coil. Again, the baseline ϕ used in the previous calculations was 17. Nevertheless, it is important to understand the effect of varying ϕ from the standpoint of numerical accuracy, while for computational efficiency, it is worthwhile to keep ϕ as small as possible without sacrificing that accuracy.

In Figure 22, we show the effect of varying ϕ on the response of the Separate configuration, with baseline parameters used for k and b. For reference, the dipole calculation is shown as the dotted black line. The smallest discretization considered, $\phi = 9$, is shown in solid black, while the responses for $\phi = 17$, 25, and 33 are shown in blue, red, and green, respectively. While the error is considerable for the $\phi = 9$ case, the $\phi = 17$, 25, and 33 cases are close to one another, with the $\phi = 17$ and 25 approaching the $\phi = 33$ line, which is naturally closest to the true response. Since for each integration time step, the number of calculations goes as ϕ^2, we have chosen $\phi = 17$ for both its relative speed and accuracy.

3.4.5   Note on elasticity of panel

We note that there exists an expression for the torque about the center of mass of a coil in the dipole limit. The expression is

$$\vec{\tau}_{O,Dipole}^{(1)} = \frac{\mu}{4\pi}\left[\vec{m}_1 \times \left(\frac{3\vec{r}(\vec{m}_2 \cdot \vec{r})}{r^5} - \frac{\vec{m}_2}{r^3}\right)\right]$$

$$\vec{\tau}_{O,Dipole}^{(2)} = \frac{\mu}{4\pi}\left[\vec{m}_2 \times \left(\frac{3\vec{r}(\vec{m}_1 \cdot \vec{r})}{r^5} - \frac{\vec{m}_1}{r^3}\right)\right]$$

While there will be a tendency for the magnetic moments to want to rotate about their centers due to the above torques, it is important to note that, as long as the panels are taken to be rigid, these torques exert no influence on the motion of the coil about the hinge axis. The influence of these torques would only be manifest if the panels were elastic, in which case the torques around the center of the coils would impart a moment on the panel resulting in bending of the panel. Accounting for this would necessitate solving the dynamic bending equations for the panels and would, to an extent determined by the deployment geometry and the material properties of the panel, affect the distance between the coils.

To gauge what this criterion would be for which bending is appreciable, we may conduct a simple order of magnitude analysis. From the theory of beam bending, we have that the bending moment of a beam is given by:

$$-EJ\frac{\partial^2 y}{\partial x^2}$$

where *x* is a coordinate directed along the axis of the unbent beam, *E* is the elastic modulus of the beam material, and *J* (not to be confused with the current) is the area moment of inertia of the beam. If we approximate the deflection *y* of the beam due to the dipole torque as δ and take $x \sim L_m$, then we have, using the dipole torque expression,

$$EJ\frac{\delta}{L_m^2} \sim \frac{\mu}{2\pi}\frac{I_{eff,1}\,I_{eff,2}\,A_1 A_2}{r^3}$$

or, rearranging,

$$\delta \sim \frac{\mu}{2\pi}\frac{I_{eff,1}\,I_{eff,2}\,A_1 A_2}{r^3}\frac{L_m^2}{EJ}$$

Now, the criterion for which this would have a negligible effect on the hinge dynamics of the coil-panel system (by altering the coil center-to-coil center distance) is that: [1]

$$\frac{\delta}{r} \ll 1$$

or

$$\frac{\mu}{2\pi} \frac{I_1 I_2 A_1 A_2}{r^4} \frac{L^2}{EJ} \ll 1$$

Since E is typically on the order of $10^{10} - 10^{11}$ Pa for metals and $\mu = 1.26 \times 10^{-6}$ T·m /A, we can rewrite the above in a more illuminating manner by considering a lower elastic modulus case:

$$\frac{I_1 I_2 A_1 A_2}{J r^4} \ll 2\pi \times 10^{16} \frac{A^2}{m^2}$$

This criterion will generally be easily satisfied. Furthermore, since at short distances, the dipole approximation for forces and torques tends to overestimate that due to the actual force law (see below), the above expression may be taken as a general rule for ensuring that bending effects are negligible.

3.4.6 Motion of a coil under its own force in Expand configuration

Consider a flexible coil that is in some noncircular configuration (as in Figure 23). If current is run through this coil, a given differential coil element will experience a force due to the electromagnetic forces exerted on it by all other elements on the coil. It is therefore possible for a stowed coil to reconfigure itself, or Expand, into a different shape under the influence of its own electromagnetic interactions. We note that, for the rigid coil considered elsewhere in this report, such self-interactions have no bearing on the shape of the coil, so that in that case, it is assumed that the coil can effectively "absorb" the effect of self-interactions.

Figure 23: Expand deployment configuration

---

[1] A more precise statement may be $\frac{\frac{d}{dr}|\vec{F}_{12}|_{r_{12}} \delta}{|\vec{F}_{12}|_{r_{12}}} \ll 1$; however, for simplicity, we use the given relation.

Suppose we have a flexible coil, the position of a point on the coil given by $\vec{r}$. Let us parameterize the position of a point on the coil by the coil length s, so that, in general, $\vec{r} = \vec{r}(s, t)$, where t is time. If the string is of constant length (or inextensible), the equations of motion for the string are given by:

$$\rho \frac{d^2\vec{r}}{dt^2} = \frac{d}{ds}\left(\sigma \frac{d\vec{r}}{ds}\right) + \vec{F}$$

$$\frac{d\vec{r}}{ds} \cdot \frac{d\vec{r}}{ds} = 1$$

The second equation is a restatement of the Pythagorean theorem as applied to a infinitesimal coil element. σ is the magnitude of the local tension in the string, so that the vector

$$\sigma \frac{d\vec{r}}{ds}$$

is a force acting across the cross section of the coil. For an inelastic coil, both equations above must be solved simultaneously. If however the coil is elastic, following a linear elastic force law, the equations of motion reduce to a generalized wave equation:

$$\rho \frac{d^2\vec{r}}{dt^2} = \frac{d}{ds}\left[EA_c \frac{d\vec{r}}{ds}\right] + \vec{F}$$

where E is the elastic modulus of the coil material and A_c is the cross sectional area of the coil. In general, both are a function of s, but, if the coil material is uniform along its length, we have:

$$\rho \frac{d^2\vec{r}}{dt^2} = EA_c \frac{d^2\vec{r}}{ds^2} + \vec{F}$$

The force $\vec{F}$ is calculated from the Biot-Savart law given before, but applied to the coil itself:

$$\vec{F} = \frac{\mu I^2}{4\pi} \frac{d\vec{l}}{|d\vec{l}|} \times \int_{\substack{coil \\ \vec{r} \neq \vec{r}\prime}} \frac{I d\vec{l}\prime \times (\vec{r} - \vec{r}\prime)}{|\vec{r} - \vec{r}\prime|^3}$$

where $\vec{r}\prime$ is the vector to any point on the coil not equal to $\vec{r}$ and $d\vec{l}\prime$ is the differential coil element at $\vec{r}\prime$. An in depth discussion of the dynamics of self-coil deployment will be reserved for the Phase II report; nevertheless, we include here some preliminary results of calculations relevant to the self-force deployment.
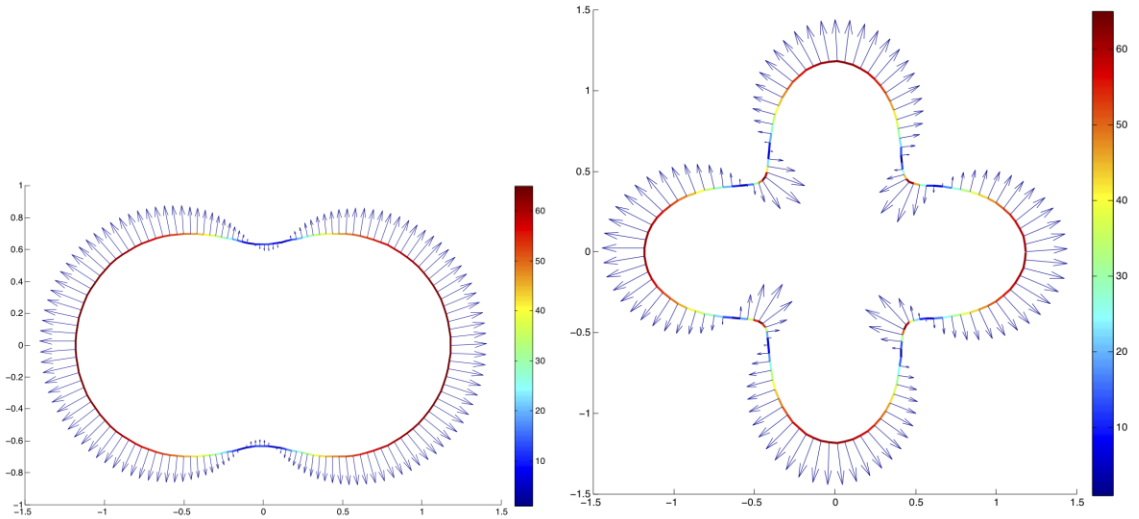
Figure 24: Instantaneous self force on coil for two different coil shapes. Direction and magnitude of force indicated in arbitrary units.

In Figure 24, we show the instantaneous force vectors acting along coils of different shapes. We note that inflection points along the curve are coincident with locations where the electromagnetic self-force vanishes.

In Figure 25, we see a visualization of the time evolution of self-deployment of a coil in accordance with the equations of motion above for an inelastic coil. The coil starts from a stowed, folded position, and, over time, acquires a circular shape due to the mutual repulsion of coil elements. We note that, during self-deployment, the coil will generally oscillate for some period about an equilibrium circular configuration. Nevertheless, as any material is not perfectly elastic, these oscillatory motions will ultimately be damped out, the efficiency with which is occurs depending on the construction and material properties of the coil. At the present, we have not implemented elasticity in the coil material.
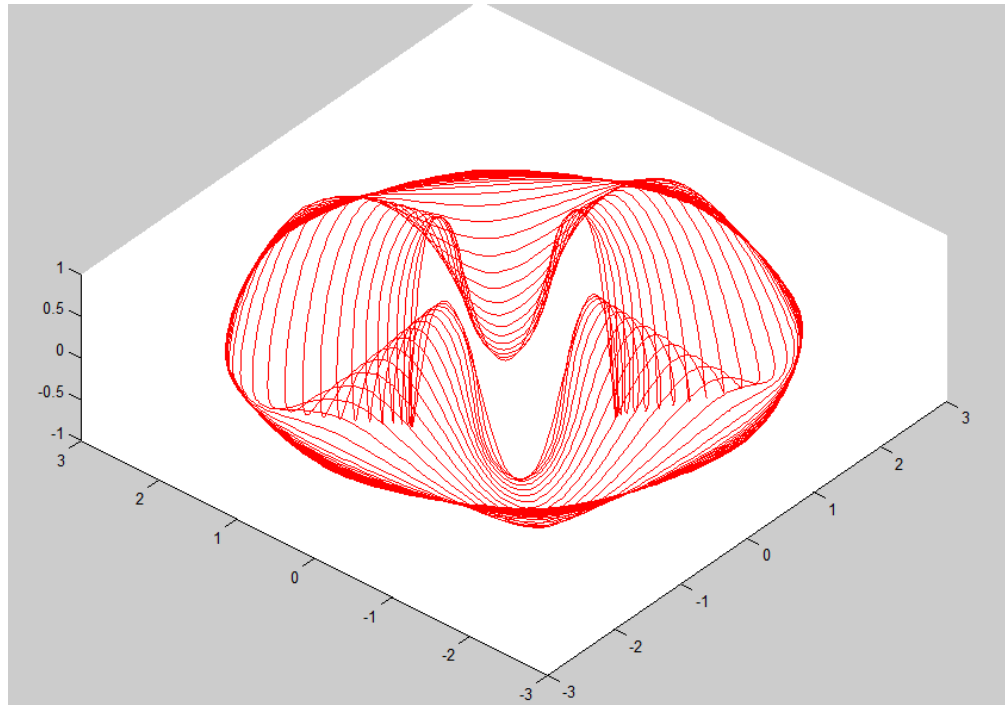
Figure 25: Visualization of self-deployment of a coil from a stowed configuration to a planar, circular shape.

3.5   Conclusion

In this chapter, we have detailed the derivation of the equations of motion for current-carrying coils under the influence of electromagnetic forces and constraining elements. We have developed and validated a set of numerical simulation tools to evaluate the performance of electromagnetic system dynamics. By using the numerical models for rigid coils with appropriate mechanical constraints, we can now begin to set up the systems engineering trades for the implementation of electromagnetic deployables in candidate space system designs and investigate the ranges of values over which an electromagnetic structure is feasible.

4　Chapter 4 – Feasibility

In this chapter, we will study the feasibility of electromagnetic structures in space systems by using the models described in Chapter 3 to generate data over a range of design variables for the Separate and Unfold functional configurations, including current, coil diameter, number of turns, and others. These data are intended to provide a means of trading electromagnetic designs with one another for different application requirements. We will also introduce the prevailing trades between variables and between electromagnetic structures and alternative structural technologies such as inflatables and tensegrity structures.

4.1　Electromagnetic structure design variables

Electromagnetic structures have a variety of independent design variables as well as dependent design variables that are a function of the other variables. Table 6 displays several of the most important variables in the design vector for electromagnetic structures as well as their interdependencies, which are listed in the third column.

Table 6: Design variables

Variables	Symbol	Function of?
Independent, General		
Current through wire	I	--
Diameter	D	--
# of turns	n	--
Density per unit length of wire	ρ	--
Initial distance between coil centers	d_{start}	--
Initial angle between coils	θ_{init}	--
Angle between coils (over time)	θ	--
Stowed structure length	L_s	--
Damping coefficient	b, β	--
Discretization of coil	φ	--
Independent, Tethered		
Unstretched length of tethers	L_t	--
Elasticity of tethers	k	--
Independent, Hinged		
Torsional spring constant	κ	--
Mass of panel attached to coil	m_{panel}	--
Unstretched angle of spring	θ_0	--

Dependent		
Effective current	I_{eff}	I, n
Current element	Idl	I_{eff}, φ, D
Mass (each coil)	m	D, n, ρ
Mass (total)	m_{tot}	m, m_{panel}
Distances from elements on coil 1 to coil 2	r_{ij}	D, d, ϑ, φ
Force (one element on another)	F	Idl, r_{ij}
Force (total on coil)	F_{tot}	F
Distance between coil centers (over time)	d	d_0, F, L_t, κ, m, m_{panel}
Force (dipole)	F_{dip}	I_{eff}, D, n, d, ϑ
Acceleration	a	F, m
Characteristic/Equilibrium length	L_{eq}	F, d, L_t and k (if applicable)
Size ratio	S	L_{eq}, L_s
Torque	τ	F, D
Hinge moment arm length	L_m	d, θ_{init}
Equilibrium angle of hinge	θ_{eq}	F, κ, L_m
Deployment time	T	F_{dip} or F, m, L_t, b, k,θ_0,L_m,d
Moment of inertia	[I], I_{hinge}	m, L_m, θ_{init}, D, m_{panel}

There are several other design variables that come into play when more than two coils are being considered, the coils have variable current controllers, or when the coils are different sizes, but for now we are just examining two-coil, same-sized coil systems with constant currents throughout the deployment.

4.2   Reformulation of equations of motion for trade space analysis

Before exploring the variable or trade space, it is important to note that the number of independent variables, when the equations of motion are written as is, is large. To examine variance across each of the dependent variables as a function of changing each independent variable individually would be an overwhelming amount of data and plots. Therefore, it is worth exploring methods by which the dimensionality of the variable space can be reduced. One method by which this can be accomplished is via non-dimensionalization of the equations of motion. This process, which is commonly used in fluid dynamics and heat and mass transfer, greatly reduces the variable space by creating dimensionless variables that are combinations of the original ones. The process will be demonstrated below for both the Separate and Unfold configurations. We assume that in both cases the relevant geometries and properties for each coil, panel, and tether are the same (i.e. $m_1 = m_2 \equiv m$, $k_1 = k_2 \equiv k$, etc.).

First, we choose an important, characteristic geometrical variable against which we scale *all* variables in the problem that have dimensions of length; next, we do the same for the time scale. We choose R, the radius of each coil, as the characteristic length variable. We choose as the characteristic time variable $\mathcal{T}$, which we set arbitrarily to 1 second. Now, we proceed to define dimensionless auxiliary variables based on the variable originally appearing in the equations of motion; these dimensionless auxiliary variables will be distinguished by tildes "~" or asterisks "*" and are given in Table 7.

Table 7: Dimensionless variable definitions

Dimensionless variable	Variable definition
$\tilde{R}_i \equiv \dfrac{R}{R} = 1$	Radius of coil i
$\tilde{\bar{r}}_i \equiv \dfrac{\bar{r}_i}{R}$	Vector position center of coil i
$\tilde{\vec{r}}_i \equiv \dfrac{\vec{r}_i}{R}$	Vector position of a point on coil i
$\tilde{\vec{r}}_{ij} \equiv \dfrac{\vec{r}_{ij}}{R}$	Vector distance between a point on coil i to a point on coil j
$d\tilde{\vec{l}}_i \equiv \dfrac{d\vec{l}_i}{R}$	Vector differential length element at a point on coil i
$L_{t,\alpha}{}^* \equiv \dfrac{L_{t,\alpha}}{R}$	Length of tether α
$\tilde{\vec{P}}_\alpha^{(i)} \equiv \dfrac{\vec{P}_\alpha^{(i)}}{R}$	Vector position of tether α attachment point on coil i
$\tilde{t} \equiv \dfrac{t}{\mathcal{T}}$	Time
$\tilde{\vec{V}}_\alpha \equiv \dfrac{\mathcal{T}}{R}\vec{V}_\alpha$	Relative velocity of tether α attachment points on coils 1 and 2
$d_{start}{}^* \equiv \dfrac{d_{start}}{R}$	Starting coil separation
$L_{eq}{}^* \equiv \dfrac{L_{eq}}{R}$	Equilibrium separation of coils

Substituting the above dimensionless variables in for the original variables yields the following general equations of motion:

Tether:

$$m\frac{d^2(R\tilde{\vec{r}}_1)}{d(\mathcal{T}\tilde{t})^2} = -\sum_{\alpha=1}^{3}\left\{k_\alpha(R\Delta\tilde{L}_\alpha)H_\alpha\hat{P}_{elast,\alpha} + b_\alpha\left(\frac{R}{\mathcal{T}}\right)|\tilde{\vec{V}}_\alpha|H_\alpha\left[\frac{\text{sign}(\tilde{\vec{V}}_\alpha)}{\sqrt{3}}\cdot\hat{P}_{elast,\alpha}\right]\hat{P}_{elast,\alpha}\right\} + \frac{\mu I_{eff,1}I_{eff,2}}{4\pi}\oint_{\text{Loop 1}}\left(Rd\tilde{\vec{l}}_1\right)\times\oint_{\text{Loop 2}}\frac{(Rd\tilde{\vec{l}}_2)\times(R\tilde{\vec{r}}_{12})}{|R\tilde{\vec{r}}_{12}|^3}$$

$$m\frac{d^2(R\tilde{\vec{r}}_2)}{d(\mathcal{T}\tilde{t})^2} = +\sum_{\alpha=1}^{3}\left\{k_\alpha(R\Delta\tilde{L}_\alpha)H_\alpha\hat{P}_{elast,\alpha} + b_\alpha\left(\frac{R}{\mathcal{T}}\right)|\tilde{\vec{V}}_\alpha|H_\alpha\left[\frac{\text{sign}(\tilde{\vec{V}}_\alpha)}{\sqrt{3}}\cdot\hat{P}_{elast,\alpha}\right]\hat{P}_{elast,\alpha}\right\} - \frac{\mu I_{eff,1}I_{eff,2}}{4\pi}\oint_{\text{Loop 2}}\left(Rd\tilde{\vec{l}}_2\right)\times\oint_{\text{Loop 1}}\frac{(Rd\tilde{\vec{l}}_1)\times(R\tilde{\vec{r}}_{21})}{|R\tilde{\vec{r}}_{21}|^3}$$

Hinge:

$$I_{Hinge}^{(1)}\frac{d^2\theta_1}{d(\mathcal{T}\tilde{t})^2}\hat{j} = \kappa(|\theta_2-\theta_1|-\theta_0)\hat{j} - \beta\frac{d\theta_1}{d(\mathcal{T}\tilde{t})}\hat{j} + \frac{\mu I_{eff,1}I_{eff,2}}{4\pi}\oint_{\text{Loop 1}}(R\tilde{\vec{r}}_1)\times\left(Rd\tilde{\vec{l}}_1\right)\times\oint_{\text{Loop 2}}\frac{(Rd\tilde{\vec{l}}_2)\times(R\tilde{\vec{r}}_{12})}{|R\tilde{\vec{r}}_{12}|^3}$$

$$I_{Hinge}^{(2)}\frac{d^2\theta_2}{d(\mathcal{T}\tilde{t})^2}\hat{j} = -\kappa(|\theta_2-\theta_1|-\theta_0)\hat{j} - \beta\frac{d\theta_2}{d(\mathcal{T}\tilde{t})}\hat{j} + \frac{\mu I_{eff,1}I_{eff,2}}{4\pi}\oint_{\text{Loop 2}}(R\tilde{\vec{r}}_2)\times\left(Rd\tilde{\vec{l}}_2\right)\times\oint_{\text{Loop 1}}\frac{(Rd\tilde{\vec{l}}_1)\times(R\tilde{\vec{r}}_{21})}{|R\tilde{\vec{r}}_{21}|^3}$$

Collecting all the constant terms then yields:

Tether:

$$\frac{d^2\tilde{\vec{r}}_1}{d\tilde{t}^2} = -\sum_{\alpha=1}^{3}\left\{\left(\frac{k_\alpha\mathcal{T}^2}{m}\right)\Delta\tilde{L}_\alpha H_\alpha\hat{P}_{elast,\alpha} + \left(\frac{b_\alpha\mathcal{T}}{m}\right)|\tilde{\vec{V}}_\alpha|H_\alpha\left[\frac{\text{sign}(\tilde{\vec{V}}_\alpha)}{\sqrt{3}}\cdot\hat{P}_{elast,\alpha}\right]\hat{P}_{elast,\alpha}\right\} + \frac{\mu I_{eff,1}I_{eff,2}\mathcal{T}^2}{4\pi mR}\oint_{\text{Loop 1}}d\tilde{\vec{l}}_1\times\oint_{\text{Loop 2}}\frac{d\tilde{\vec{l}}_2\times\tilde{\vec{r}}_{12}}{|\tilde{\vec{r}}_{12}|^3}$$

$$\frac{d^2\tilde{\vec{r}}_2}{d\tilde{t}^2} = +\sum_{\alpha=1}^{3}\left\{\left(\frac{k_\alpha\mathcal{T}^2}{m}\right)\Delta\tilde{L}_\alpha H_\alpha\hat{P}_{elast,\alpha} + \left(\frac{b_\alpha\mathcal{T}}{m}\right)|\tilde{\vec{V}}_\alpha|H_\alpha\left[\frac{\text{sign}(\tilde{\vec{V}}_\alpha)}{\sqrt{3}}\cdot\hat{P}_{elast,\alpha}\right]\hat{P}_{elast,\alpha}\right\} + \frac{\mu I_{eff,1}I_{eff,2}\mathcal{T}^2}{4\pi mR}\oint_{\text{Loop 2}}d\tilde{\vec{l}}_2\times\oint_{\text{Loop 1}}\frac{d\tilde{\vec{l}}_1\times\tilde{\vec{r}}_{21}}{|\tilde{\vec{r}}_{21}|^3}$$

Hinge:

$$\frac{d^2\theta_1}{d\tilde{t}^2}\hat{j} = +\frac{\kappa\mathcal{T}^2}{I_{Hinge}}(|\theta_2-\theta_1|-\theta_0)\hat{j} - \frac{\beta\mathcal{T}}{I_{Hinge}}\frac{d\theta_1}{d\tilde{t}}\hat{j} + \frac{\mu I_{eff,1}I_{eff,2}\mathcal{T}^2R}{4\pi I_{Hinge}}\oint_{\text{Loop 1}}\tilde{\vec{r}}_1\times d\tilde{\vec{l}}_1\times\oint_{\text{Loop 2}}\frac{d\tilde{\vec{l}}_2\times\tilde{\vec{r}}_{12}}{|\tilde{\vec{r}}_{12}|^3}$$

$$\frac{d^2\theta_2}{d\tilde{t}^2}\hat{j} = -\frac{\kappa\mathcal{T}^2}{I_{Hinge}}(|\theta_2-\theta_1|-\theta_0)\hat{j} - \frac{\beta\mathcal{T}}{I_{Hinge}}\frac{d\theta_2}{d\tilde{t}}\hat{j} + \frac{\mu I_{eff,1}I_{eff,2}\mathcal{T}^2R}{4\pi I_{Hinge}}\oint_{\text{Loop 2}}\tilde{\vec{r}}_2\times d\tilde{\vec{l}}_2\times\oint_{\text{Loop 1}}\frac{d\tilde{\vec{l}}_1\times\tilde{\vec{r}}_{21}}{|\tilde{\vec{r}}_{21}|^3}$$

Next, we will redefine the dimensionless coefficients from the above equations in order to simplify the expressions. We also prescribe "baseline" values to each of the constituent variables in order to find a baseline value for each of the dimensionless parameters to use in anchoring plots of variable trades. The dimensionless quantities presented below in Table 8 now represent the key parameters for each functional configuration:

Table 8: Dimensionless parameter definitions

Dimensionless parameter	Parameter definition	Baseline values of included variables	Dimensionless parameter values for trades [Baseline]
$\gamma = \dfrac{\mu I_{eff,1} I_{eff,2} \mathcal{T}^2}{4\pi m R}$	Tether (Separate) force coefficient	$I_{eff,1}, I_{eff,2} = 9000$ A $m = 10.2$ kg $R = 0.5$ m	$\gamma_0 = 1.588$
$k^* = \dfrac{k_\alpha \mathcal{T}^2}{m}$	Tether (Separate) spring constant	$k_\alpha = 0.1$ N/m $m = 10.2$ kg	$k_0{}^* = 0.010$
$b^* = \dfrac{b_\alpha \mathcal{T}}{m}$	Tether (Separate) damping constant	$b_\alpha = 2/3$ N/m^2 $m = 10.2$ kg	$b_0{}^* = 0.065$
$\xi = \dfrac{\mu I_{eff,1} I_{eff,2} \mathcal{T}^2 R}{4\pi I_{Hinge}}$	Hinge (Unfold) force coefficient	$I_{eff,1}, I_{eff,2} = 9000$ A $R = 0.5$ m I_{Hinge} $= 1.343 \times 10^3$ kg·m^2	$\xi_0 = .003$
$\kappa^* = \dfrac{\kappa \mathcal{T}^2}{I_{Hinge}}$	Hinge (Unfold) spring constant	$\kappa = 1$ N · m/rad I_{Hinge} $= 1.343 \times 10^3$ kg·m^2	$\kappa_0{}^* = 7.443 \times 10^{-4}$
$\beta^* = \dfrac{\beta \mathcal{T}}{I_{Hinge}}$	Hinge (Unfold) damping constant	$\beta = 60$ N · m · s/rad I_{Hinge} $= 1.343 \times 10^3$ kg·m^2	$\beta_0{}^* = 0.045$

We are able to plot dimensionless dependent variables of interest against these dimensionless parameters in order to study the effects of certain system trades in each of the Separate and Unfold configurations as well as the behavior of unconstrained coils. Section 4.3 introduces and models several of the more interesting trades.

4.3   Trades

In each of the three models/functional configurations introduced in this report, there are a number of trades of system parameters that can be investigated in order to see relative sensitivity between variables as well as establish what combinations of parameters result in a viable system design. This section will discuss these trades from a mission level perspective and then explore them in detail using the models we have constructed.

Three of the most important parameters across most space missions are mass, required power, and system cost, reduction being desired in each of the three. As can be seen from the definition of the coefficient γ, force is proportional to the product of mass and current (power being proportional to the current through each coil as well as the number of coils in the system, which is fixed at two in this analysis). Therefore, mass and current can be traded against each other for a fixed γ, or γ can be reduced to a small value, thus minimizing both. The power of nondimensionalizing the variables in this problem is the ability to group these important parameters together such that the interior parameters can be switched around and still retain the same dimensionless parameter value and thus system behavior. A system designer can take the plots in this section and determine the desired γ or ξ for the desired behavior, as well as corresponding spring and damping constants, and then use the defined relationship to trade the interior parameters like mass and current. System cost is assumed to correlate positively with the number of turns in each coil and with the number of coils in the system, so lowering mass and current can be related to a reduction in system cost. Note that a complete cost analysis was not performed in the course of this Phase I work but is planned for future hardware development research.

Many of the plots in this section plot γ or ξ against deployment time T for various $k*$ and $b*$. While deployment time is not usually a key performance parameter in the deployment of space structures, these plots are mainly for exploring reasonable ranges of values for the system parameters. Plotting against deployment time gives a nice visualization of how changing each variable affects the end result of the system, as well as lets us see easily when a certain design does not ever converge to a steady state. Also, some of the operational configurations that are possible with electromagnetic structures may be more time critical, such as a Deformation to avoid a collision or a Reconfiguration quickly in reaction to a sudden event of interest for observational spacecraft, making deployment time an important parameter in these cases.

4.3.1 Six Degree of Freedom (6DoF) free

The 6DoF free case does not correspond to any of the functional configurations in particular, but it represents the basis for all electromagnetic structures and is valuable for studying some of the most basic relationships between variables without the complication of boundary constraints, especially between force and resultant motion. Force is very important at a mission level because all motion and equilibrium configurations are directly related to the force coefficient.

The force generated between two electromagnetic coils is proportional to $1/d^2$ By nondimensionalizing d into multiples of coil radii (d/R) and using a range of γs as specified in Table 8, we can see easily the effect on the force of variation of the variables contributing to the force calculation. Figure 26 relates the force coefficient γ to the time it takes for two unconstrained coils to repel to twenty times their original starting distance.
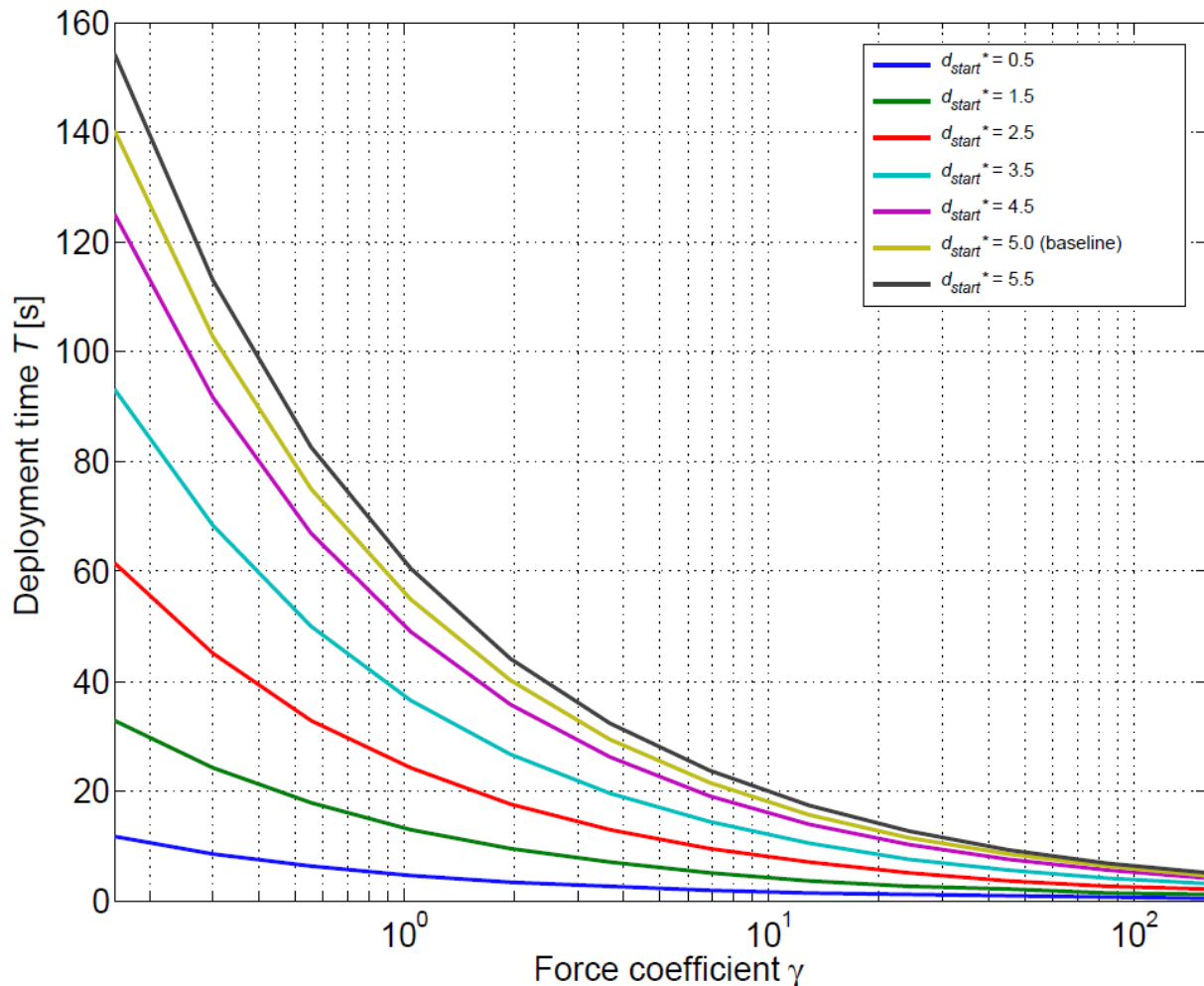

Figure 26: Time T to separate to 20 x d_{start}* as a function of γ plotted for values of d_{start}* from $0.5\ to\ 5.5$.

Deployment time decreases with increased force, which follows from Newton's second law. Since force is comprised of the force coefficient γ and a term dependent on distance between the coils, the distance term dominates the force calculation for small γs, especially for small d_{start}*s,* and we see that the lines are divergent and that *T* is influenced strongly by d_{start}* for small γs. High γs dominate the force calculation and so we see convergence and little dependence by *T* on d_{start} with high γs.

4.3.2   Tethered constraints in Separate configuration

The tethered case presented in this Phase I report examines the behavior of axially aligned coils during separation, or the configuration pictured in Figure 10 with three tethers. The behavior of coils with altered angles (which introduces torques on the coils), axial offsets or attraction instead of repulsion will be investigated further in our Phase II work.

4.3.2.1   *Force F_{tot} versus deployment time T*

The deployment time of two tethered coils depends on the electromagnetic force between them, and the damping coefficient b^* and spring constant k^* of the tethers. The values of k^* used in the plots in this chapter are for each tether; effectively, the spring constants are three times this value since there are three tethers in the system.   The electromagnetic force depends on two parameters in the nondimensionalized equations of motion: γ and the distance $|\tilde{r}_1 - \tilde{r}_2|$ between the coils. Deployment time in the tethered case is defined as the time the system takes to reach the steady state. For numerical calculations, we define the steady state to be the case in which both the relative velocity and acceleration of the two coils are arbitrarily close to zero:

$$\left|\frac{d(\tilde{r}_1 - \tilde{r}_2)}{d\tilde{t}}\right| \leq \epsilon_1, \left|\frac{d^2(\tilde{r}_1 - \tilde{r}_2)}{d\tilde{t}^2}\right| \leq \epsilon_2$$

For our calculations, we choose:

$$\epsilon_1, \epsilon_2 = 2 \times 10^{-6}$$

The following plots investigate how the deployment time *T* is a function of γ, b^*, k^*, $d_{start}{}^*$, and $L_t{}^*$.   These variables encompass most of those variables from Table 6 that affect the motion and steady state position of the system without our plots becoming redundant with variables that are closely related to one another. In each of the following cases, one variable is being varied, and the others are fixed at the baseline values given in Table 8.

4.3.2.1.1 Varying damping coefficient $b*$

Damping in our tether model occurs only while the tether is being stretched past its unstretched, natural length $L_t{}^*$. Damping depends on the tether materials and its construction. Oscillations are not desirable in deployment of space structures, especially large ones, because they could possibly amplify or aggravate structural incongruities or defects and the effect of such defects on stability of the structure. We can use deployment time as a metric to see quickly which system designs result in the shortest period of oscillations before convergence to steady state. Note that this plot does not tell us anything about the magnitude of the oscillations, just the duration. Section 3.4.4 shows validation plots of the motion of coils over time, highlighting the amplitude and duration of oscillations. Figure 27 shows how the deployment time T varies as a function of γ for variable $b*$, with $k*$ and $d_{start}*$ fixed at their baseline values. The baseline value, $b_0{}^*$, is drawn in red.
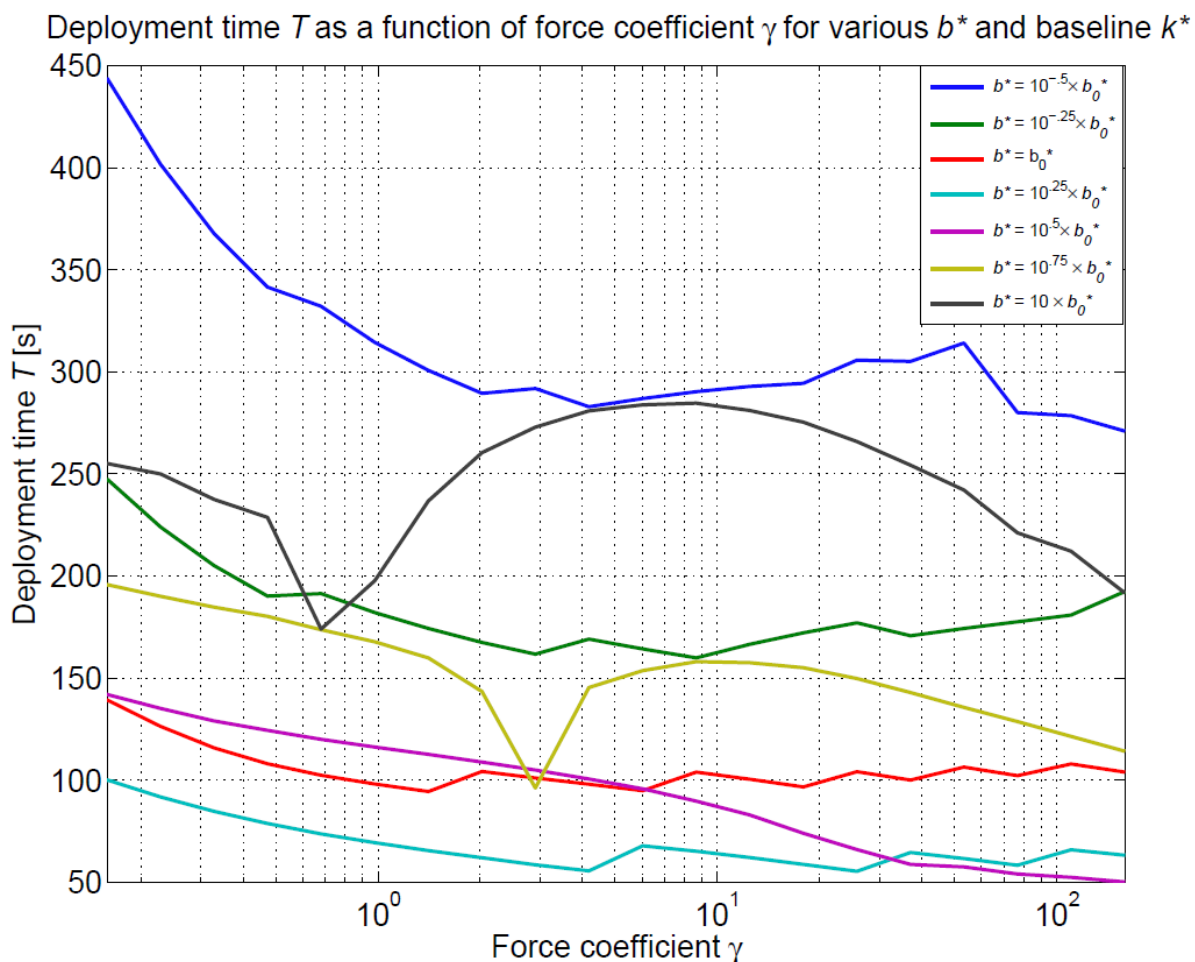

Deployment time T as a function of force coefficient γ for various $b*$ and baseline $k*$

Legend:
- $b* = 10^{-5} \times b_0{}^*$
- $b* = 10^{-25} \times b_0{}^*$
- $b* = b_0{}^*$
- $b* = 10^{25} \times b_0{}^*$
- $b* = 10^5 \times b_0{}^*$
- $b* = 10^{75} \times b_0{}^*$
- $b* = 10 \times b_0{}^*$

Figure 27: Deployment time T as a function of γ plotted for different values of $b*$ from $10^{-.5}b_0{}^*$ to $10b_0{}^*$.

We can see that T is higher (underdamped) across all γs for lower values of $b*$ than for higher values of $b*$ until we reach the minimum deployment times at $10^{.25}b_0{}^*$ (teal), which represents a value close to critical damping for the system. $10^{.5} \times b_0{}^*$ (purple) damps out oscillations

slightly faster than teal for high values of γ. Then, starting with $10^{.5} \times b_0{}^*$ (purple) and continuing on through the progressively larger values of $10^{.75} \times b_0{}^*$ (gold) and $10 \times b_0{}^*$ (grey), we see a trend back up towards longer, overdamped *T*s. The general trend is towards longer *T*s from smaller γs, since smaller electromagnetic forces result in smaller accelerations, and, hence, smaller damping forces and longer oscillatory motion. For the values of damping at and around the baseline (red, teal), the deployment time remains fairly consistent across the span of γs (after an initial startup lag due to the small forces) because larger electromagnetic forces are met with larger damping forces in response to their higher velocity and are damped out just as quickly as medium forces in this critical damping regime.

4.3.2.1.2 Varying spring constant $k*$

Figure 28 shows how the deployment time T varies as a function of γ for variable $k*$ and with $b*$ and d_0* fixed at their baseline values. The baseline value k_0* is drawn in red. For reference and comparison with Figure 27, the red baseline line is the same in each plot. There is a clearer order in Figure 28 than in Figure 27: small γs lead to longer Ts and larger γs lead to shorter Ts. This is in accord with the observation that smaller electromagnetic forces, for a given $b*$, give rise to smaller accelerations and hence smaller damping and longer periods of oscillation.
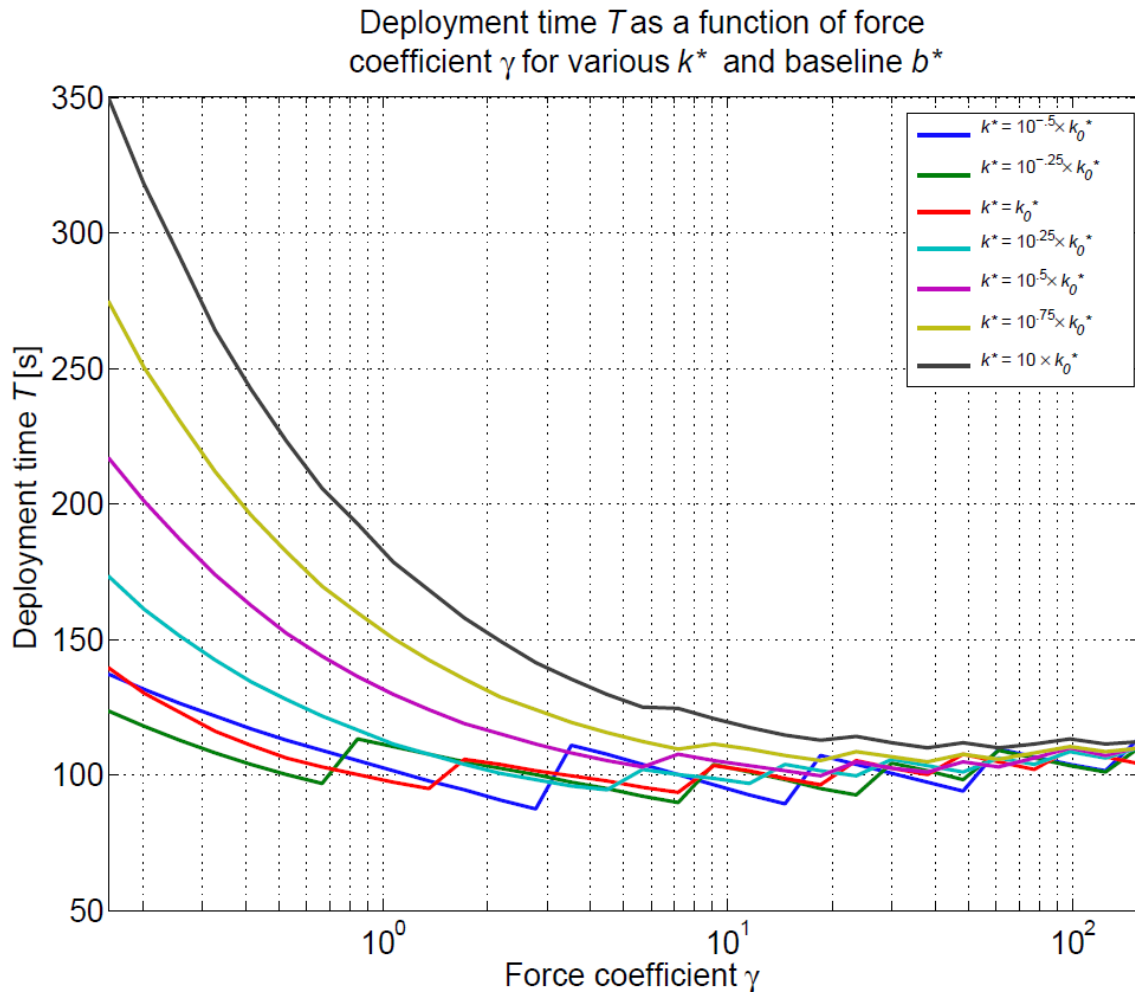

Figure 28: Deployment time T as a function of γ plotted for different values of $k*$ from $10^{-.5}k_0*$ to $10k_0*$.

The baseline (red) and the two smaller-than-baseline $k*$ values (blue and green) give the shortest Ts for all γs plotted. We see a larger spread of Ts between the $k*$ values with small γs, with larger $k*$s leading to longer T. Nevertheless, all $k*$ lines converge to nearly the same T for large γs. This narrowing follows from the increase in damping due to larger electromagnetic forces. Coils moving initially with the same small γ (and thus the same velocity) are pulled back together much harder upon reaching the stretching point of tethers with high spring constants. Large spring forces increase the number of oscillations before settling to the steady state length, thus increasing T. With large γs, the large resultant velocity of the coils triggers a correspondingly large damping force. Larger $k*$s and their larger resultant spring force and snapback velocity are also acted upon by damping, so even though they would, sans damping, take much longer to settle to steady state than cases with small $k*$s, damping serves to balance that effect.

4.3.2.1.3 Varying initial distance d_{start}*

Figure 29 shows how the deployment time T varies as a function of γ for variable d_{start}*, with b* and k* fixed at their baseline values. The baseline value, d_{start}* = 10 (coil radii), is drawn in gold. For reference and comparison with Figure 27 and Figure 28, the gold baseline line is the same as the red baseline line in the previous two plots. Usually when deploying from a stowed position, the starting distance between the coils is small (like the blue line), but studying how starting position affects the deployment behavior lets us consider multi-stage deployments where the coils start farther apart after an initial deployment activity. We use 10 coil radii for a baseline starting distance throughout this chapter arbitrarily, but Figure 29 conveys the effect of changing that value on the system dynamics.
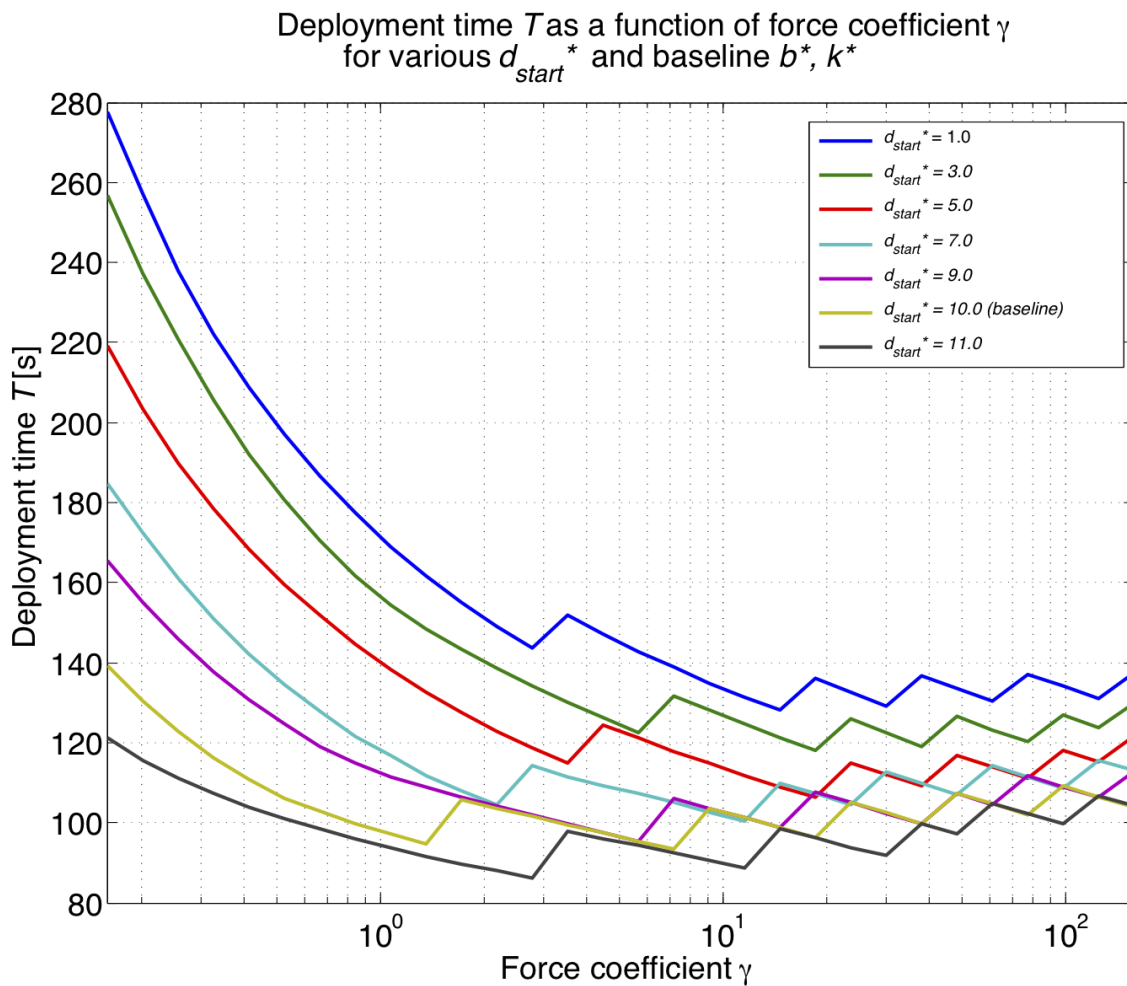

Figure 29: Deployment time *T* as a function of *γ* plotted for different values of d_{start}* from 0.5 to 5.5 coil radii.

The behavior in Figure 29 is similar to that in Figure 28; small γs lead to longer Ts, and larger γs lead to shorter Ts, but the various $d_{start}*$ values converge to the same value of T at $\gamma \sim 12$ in Figure 28 while they have nowhere near converged by $\gamma \sim 100$ in Figure 29. The range of Ts for $\gamma \sim 0.1$ is wider in Figure 28, however. This observation means that for small $\gamma \lesssim 0.5$, the system is more sensitive to changes in $k*$ than in $d_{start}*$, but for $\gamma \gtrsim 12$, the system is almost completely insensitive to changes in $k*$, while it remains sensitive to changes in $d_{start}*$. When the coils start closer to the unstretched length of the coil (in this case, $L_{eq}*$ = 6 coil radii), they have less time to accelerate before their motion is resisted by the tether spring force. That is why $d_{start}*$ = 5.5 (black) deploys the fastest regardless of γ's value; the coils do not gain a high momentum that must then be damped out to achieve equilibrium. The coils that start closer together (small $d_{start}*$s) experience exponentially higher electromagnetic forces than those coils that start farther apart due to the force's proportionality to the inverse of the distance between the coils squared. Larger forces result in larger oscillations that take more time to damp to steady state, so small $d_{start}*$s have longer Ts across the board.

4.3.2.1.4 Varying tether length L_t*

In Figure 30 and Figure 31, we see how, in the Separate configuration, the deployment time varies as a function of the force coefficient γ for various dimensionless unstretched tether lengths L_t*. The baseline value, L_t* = 12 (coil radii), is drawn in green. The green line is the same baseline line that is present in the other γ versus T plots.   The length of the tether is directly related to the characteristic or equilibrium length of the structure, L_{eq}*, which will be discussed further in the next section. Since d_{start}* is fixed at 10 coil radii in each case, we can see how increasing L_t* for a given starting distance affects the deployment behavior. Figure 30 and Figure 31 are very similar to Figure 29 because the difference between the starting and unstretched lengths is what really matters, not the value of either in particular. The values of each of L_t* and d_{start}* affect the component of the force that includes distance, but γ can be adjusted to balance that effect, leaving the relationship between L_t* and d_{start}* and T primarily dependent upon L_t* - d_{start}*.
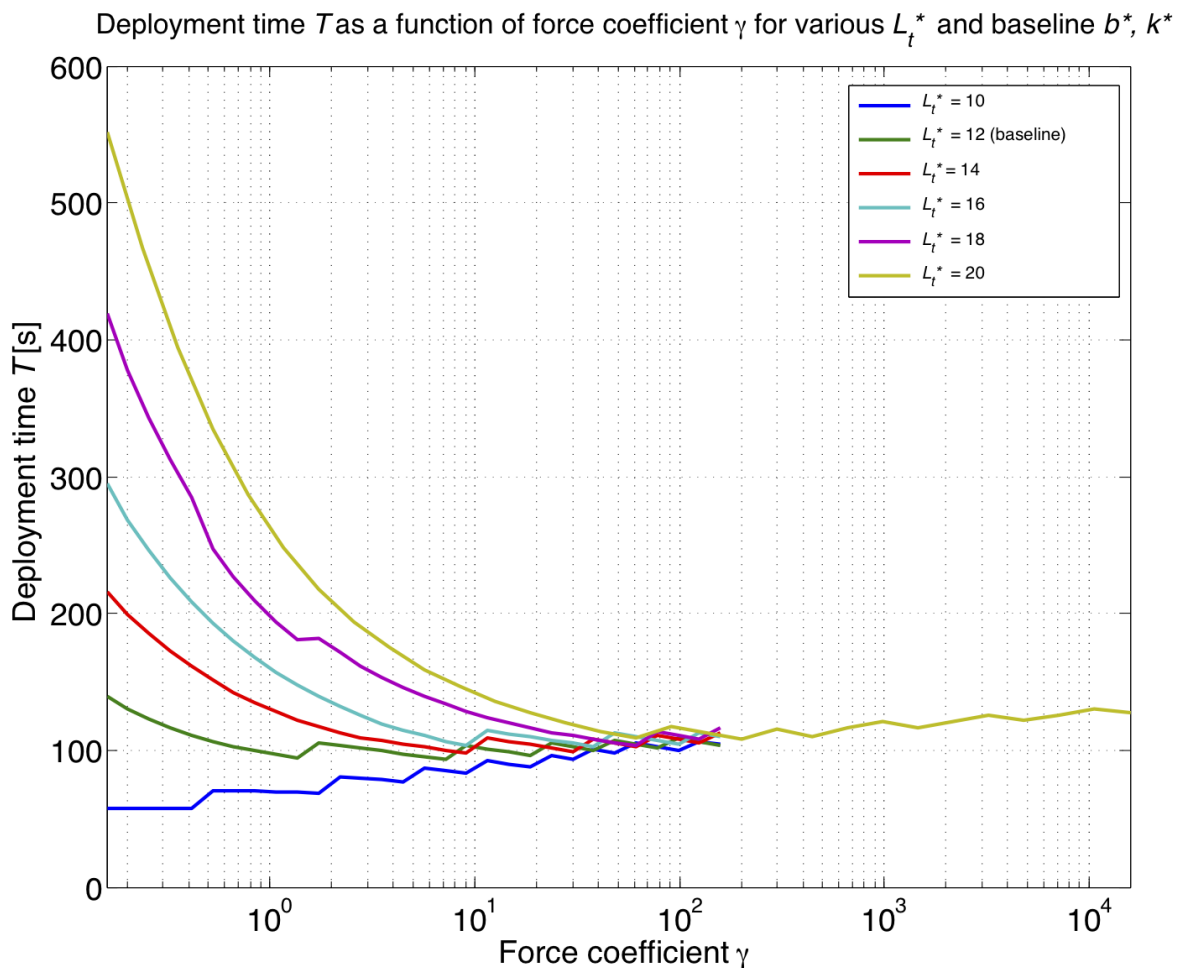

Figure 30: Deployment time T as a function of γ plotted for different values of L_t* from 5 to 10 coil radii.

In Figure 30 and Figure 31, we see how, in the Separate configuration, the deployment time varies as a function of the force coefficient γ for various dimensionless unstretched tether lengths L_t*. The spring and damping coefficients k* and b*, and the starting coil separation d_{start}* are the same for all cases. For low γ we see how, expectedly, deployment time is longer for larger L_t*. This longer time is because a greater distance must be traversed from a given d_{start}* for the tether's restorative force to take effect. This is most clearly demonstrated in Figure 31, where long tether lengths of $15L_t$* and $20L_t$* have deployment times well over 1000 s (The model was only run for 1000 seconds to generate Figure 31, so the y-intersect for the two longest tether lengths are not included but can be extrapolated from the other points). On the other hand, for larger γs, we see that the acceleration of the coils (and subsequent damping to the steady state) occurs so fast that all the deployment times for different L_t* tend to converge to the same T.
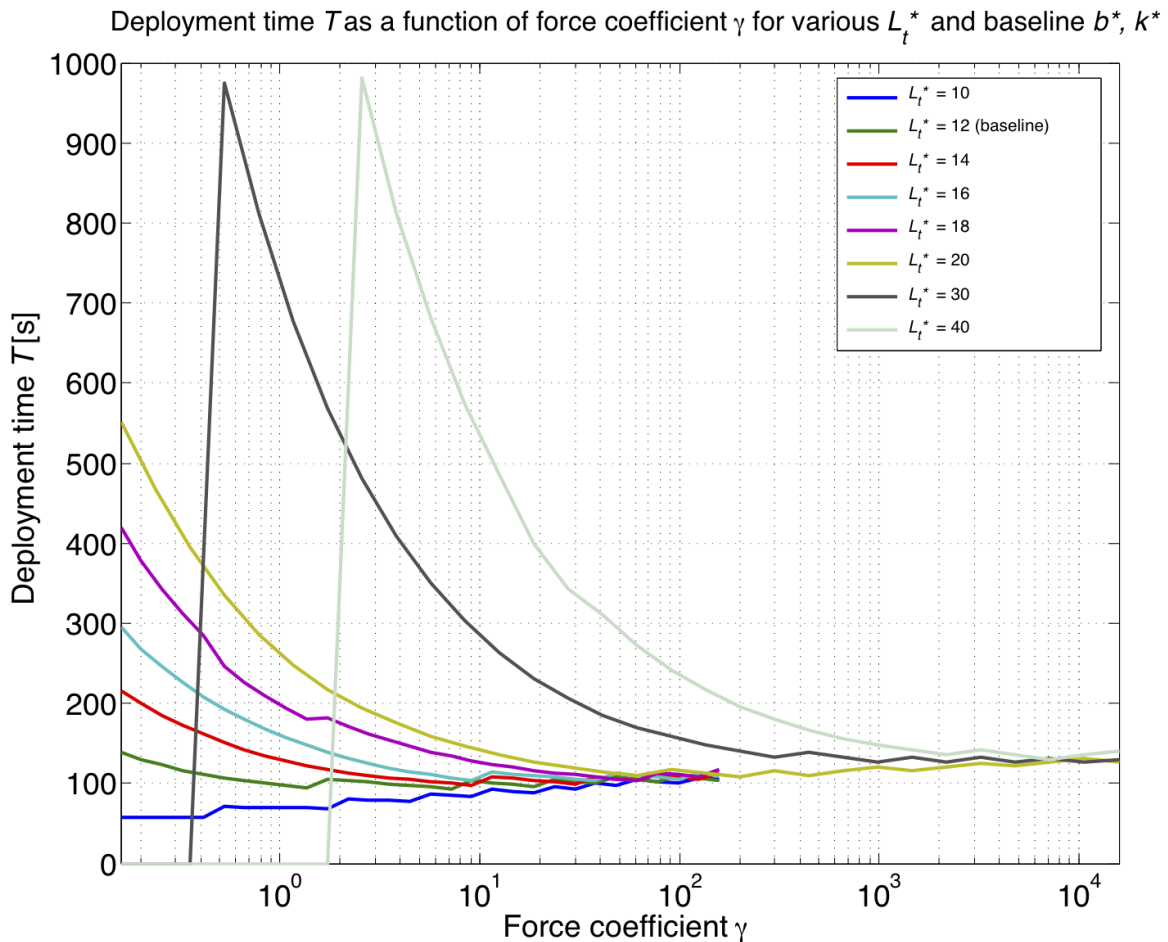

Deployment time T as a function of force coefficient γ for various L_t^* and baseline b^*, k^*

Figure 31: Deployment time *T* as a function of *γ* plotted for different values of L_t* from 5 to 20 coil radii.

*4.3.2.2 Force F_{tot} versus characteristic/equilibrium length L_{eq}**

The equilibrium length L_{eq}*of the deployed structure is a very important metric for spacecraft designers, as high-level performance requirements generally dictate the deployed size. **L_{eq}* is thus more directly representative of the viability of HTS structures as compared to other structural technologies than is deployment time.** The major design variable besides the force coefficient that affects L_{eq}* is k*. Damping (b*) and the initial position of the coils d_{start}*only affect the deployment time, not the steady state length, so long as the tethers are assumed to stay below their yield stress and therefore not stretch inelastically. Figure 32, Figure 33, and Figure 34 show these effects very succinctly. In Figure 32, where k* is varied, we see that different k*s result in different values of L_{eq}*, as do different L_t*s in Figure 33. However, in Figure 34, which gives the same single line regardless of how many b* or d_{start}* values are being plotted, we see that neither b* nor d_{start}* affects the L_{eq}* for a given γ. The takeaway from this trade is that only the force coefficient as well as the spring constant k* and natural, unstretched length L_t* of the tethers have the ability to affect the final, steady state configuration of the tethered structure. This is consistent with the conceptual model, because these parameters define the force balance in the steady state condition, while other parameters only define the starting conditions or describe the intervening system dynamics during deployment.

4.3.2.2.1 Varying k*

Figure 32 shows how the equilibrium length L_{eq}* varies as a function of γ for variable k*, with b* and d_0* fixed at their baseline values. The baseline value of k* is the red line. Figure 32, Figure 28, and Figure 31 highlight one of the more interesting system trades in a tethered system: in order to increase the equilibrium length of the system without adding coils, one can employ tethers with longer unstretched lengths or use tethers with shorter lengths that require stretching. Longer tether systems do not require as much current in each coil after initial deployment, since electromagnetic force required to maintain coils at the taut length of the tethers is significantly less than that required to actually stretch the tethers.

However, as we see in Figure 31, shorter tethers take less time to deploy than longer tethers, and low k* values deploy the fastest, as we see in Figure 28, because damping occurs during periods of the tethers being stretched and low k* tethers stretch the most. We assume mass-less tethers in the models in this report, but shorter tethers also present mass savings, though on a scale that would only matter to relatively small spacecraft. Low k* tethers also provide the capability for a system to Reconfigure or for some instruments to Refocus; an addition of current results in a longer structure, and a subtraction of current from a stretched tether system shortens the structure. In a high k* system, the system could not be extended without enormous force beyond its unstretched length, and retraction would basically require formation flight control of the coils as they would not be constrained in their motion.

Stretched tethers present a risk to the spacecraft, though: if there is a power failure, even momentarily, the electromagnetic force keeping the tethers stretched would disappear, and the spring force would pull the coils back together with no electromagnetic force to slow them as they approach collision. This could result in damage to the spacecraft or deployed structure unless redundancy is built into the power subsystem for each coil to provide temporary power or a slow fade of current to reduce the snapback from the stretched tether. Therefore, the most significant trade is risk of damage versus almost instantaneous Reconfigurability.

Equilibrium length L_{eq} as a function of force coefficient γ for various k^* and baseline b^*
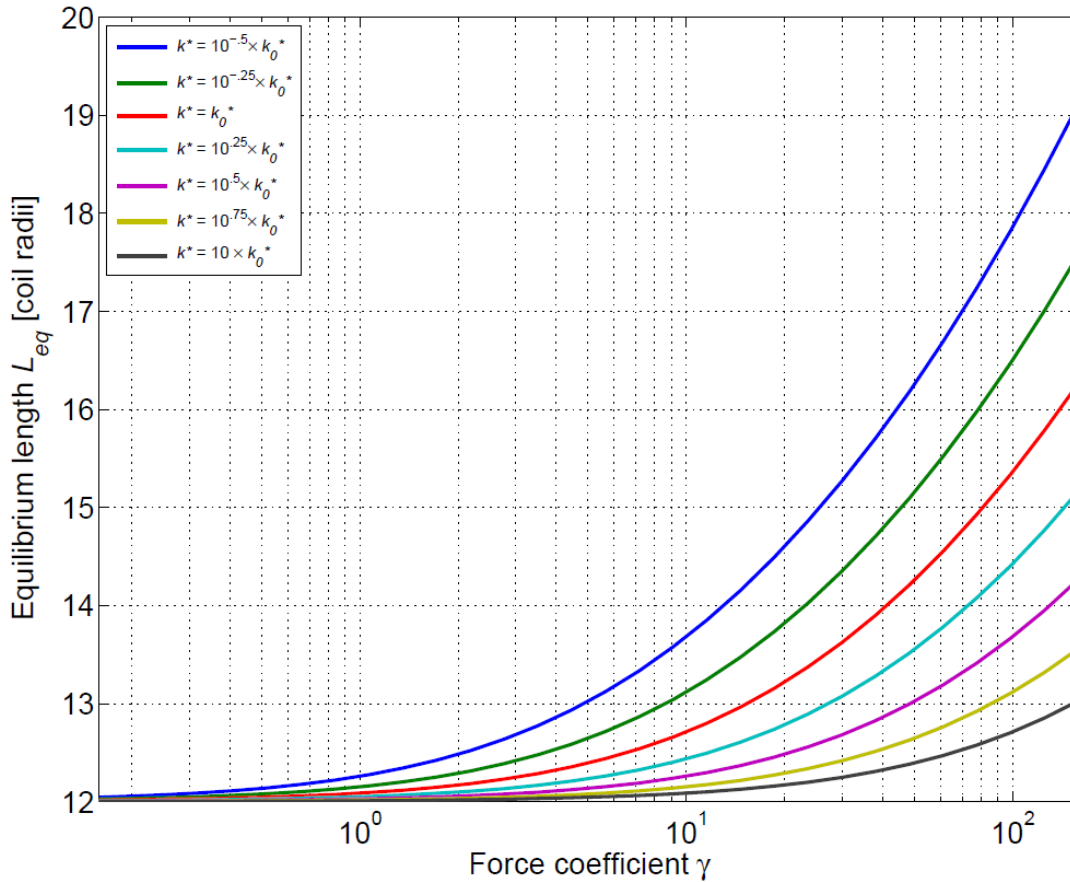

Figure 32: Equilibrium length L_{eq}^* as a function of γ plotted for different values of k^* from $10^{-.5}k_0^*$ to $10k_0^*$.

For low γs, the equilibrium length does not change for all but the smallest k^*. This is because the electromagnetic force is dwarfed by the restoring spring force in the case of larger k^*s, so only the smallest spring forces (blue, green) are of comparable magnitude to the smaller electromagnetic forces and allow some stretching. As γ increases, the electromagnetic force begins to dominate the spring force and stretch the tethers in steady state, starting with the smaller k^*s and finally stretching the system with the strongest spring force (black) around ten times the baseline k^*. We see a growing L_{eq}^* and difference between the different k^* values for large γs because high electromagnetic forces dominate spring forces (which increase linearly as L_{eq}^* increases) and thus stretch the tethers more the smaller the k^*.

4.3.2.2.2 Varying unstretched tether length L_t*

Figure 33 shows how the equilibrium length L_{eq}* varies as a function of γ for variable tether length L_t*, with b*, k*, and d_0* fixed at their baseline values. The baseline value of L_t* is pictured in teal. As per the discussion in Section 4.3.2.2.1 above, we observe that the equilibrium length increases with higher force coefficients γ and is more sensitive to the unstretched length of the tether at lower γs, since the spring force dominates the electromagnetic force there. High γs dominate the spring force, and as the tethers stretch, $L_{eq}^{*} - L_t^{*}/L_t^{*}$, or the amount the tethers stretch (ΔL) as a fraction of the unstretched length, gets smaller. For the same large γ, when L_{eq}^{*} is large as a consequence of the large force, ΔL does not vary much with L_t^{*}, which is why the lines converge for high γ.
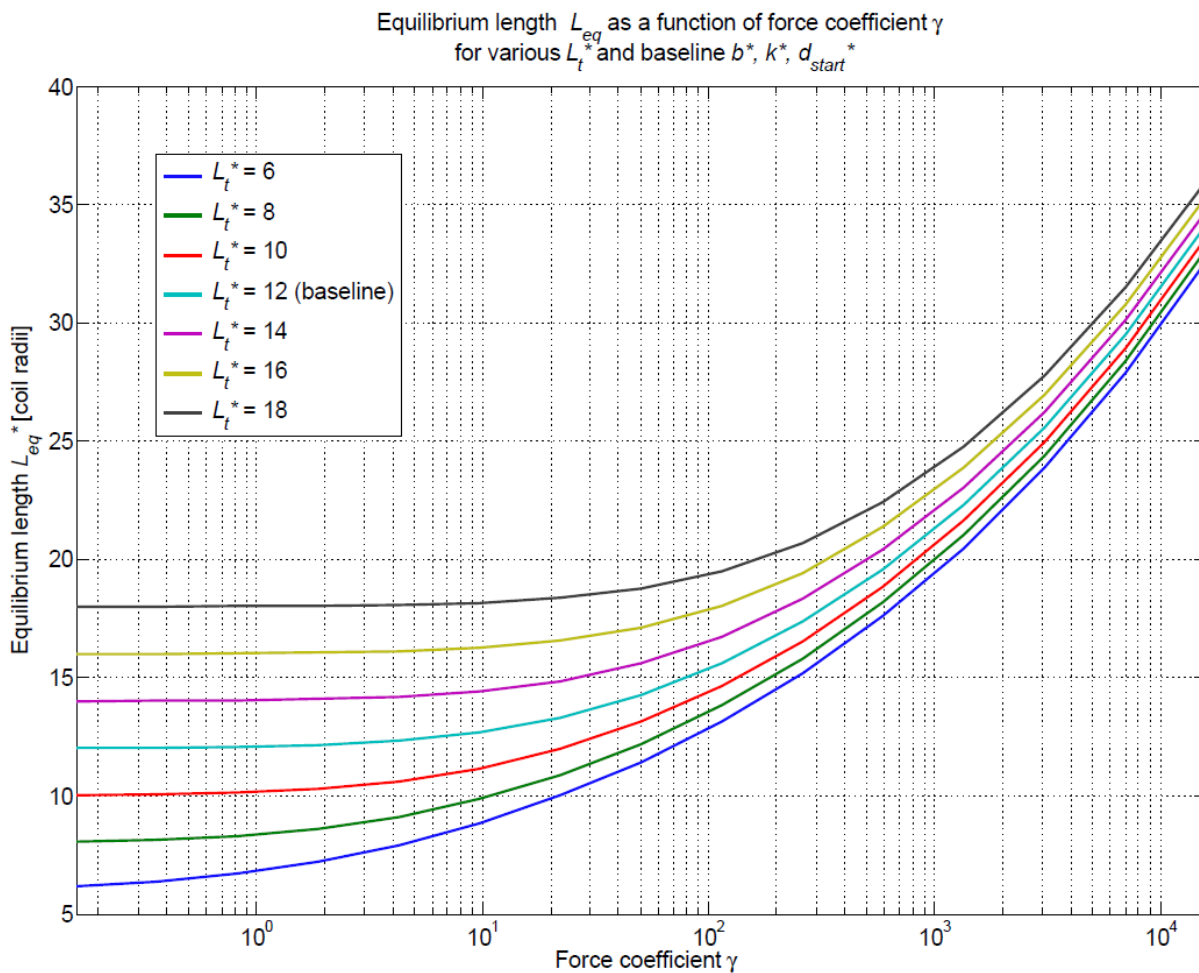

Figure 33: Equilibrium length L_{eq}*as a function of γ plotted for different values of L_t* from 6 to 18 coil radii.

Varying damping coefficient b or initial distance d_{start}* has zero impact on the steady state result of the system, as can be seen in Figure 34; all values of damping and initial distance settle out to the same steady state length L_{eq}* in the end, regardless of the time taken to do it. The blue line in Figure 34 is the same as the baseline teal line in Figure 33.
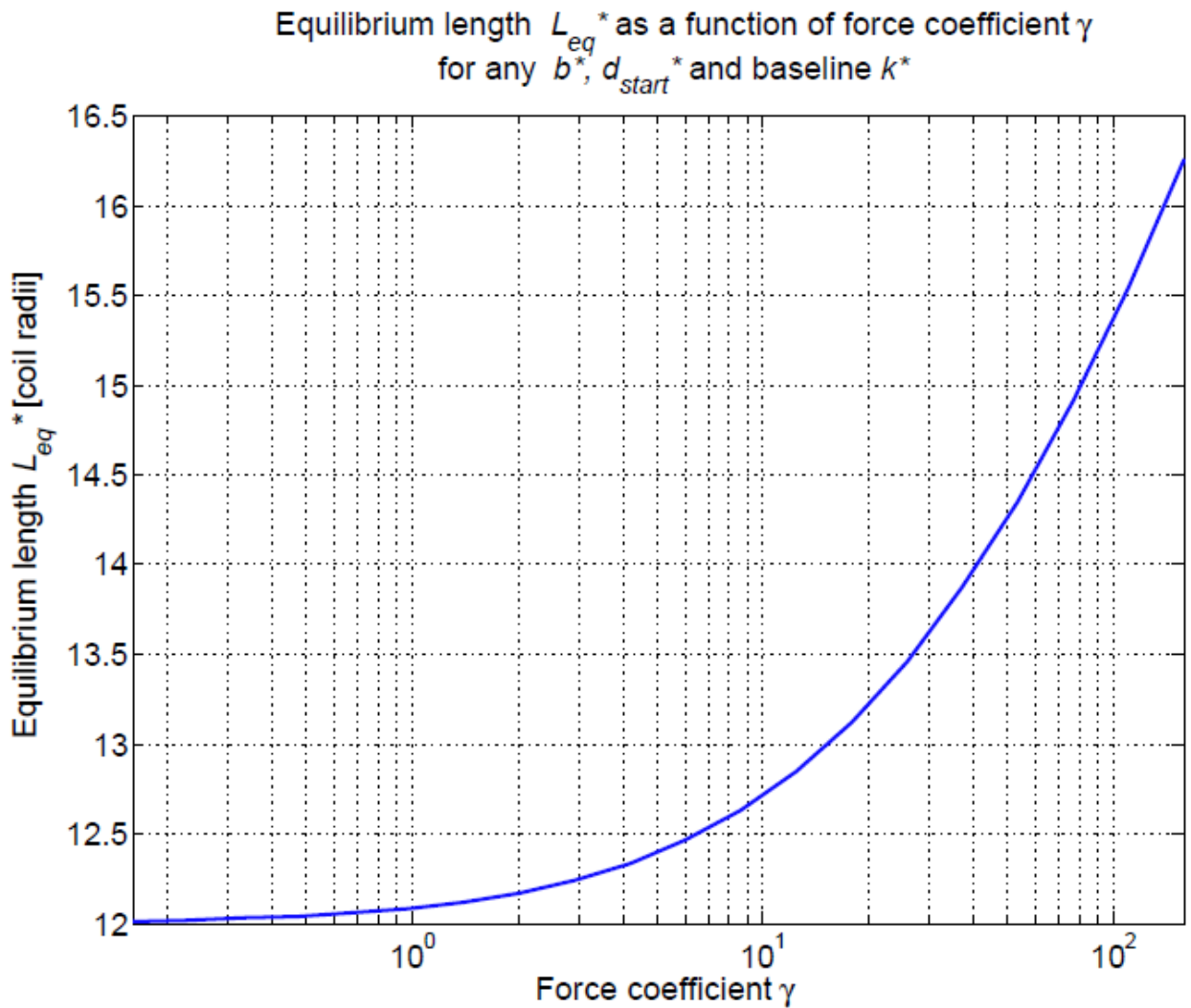

Figure 34: Equilibrium length L_{eq}*as a function of γ with k* fixed at baseline k_0* and any value of b* or d_{start}*.

4.3.3   Hinged constraints in Unfold configuration

The hinged case presented in this Phase I report examines the behavior of two coils affixed to panels joined with a hinge and a torsional spring and damper along a mutual edge, or the configuration pictured in Figure 13. The following trades are intended to provide insight into the selection of design variables like panel size, effective current, spring constant, rotational damping coefficient, and natural spring angle.

4.3.3.1 Moment ξ versus deployment time T

The deployment time of two hinged coils depends on the electromagnetic moment between them, and the damping coefficient β^* and spring constant κ^* of the hinge. The electromagnetic force depends on two parameters in the nondimensionalized equations of motion: ξ and the angle $|\theta_1 - \theta_2|$ between the coils. Deployment time in the hinged case is defined as the time the system takes to reach the steady state. For numerical calculations, we define the steady state to be the case in which both the relative angular velocity and the angular acceleration of the two coils are arbitrarily close to zero:

$$\left|\frac{d(\theta_1 - \theta_2)}{d\tilde{t}}\right| \leq \epsilon_1, \left|\frac{d^2(\theta_1 - \theta_2)}{d\tilde{t}^2}\right| \leq \epsilon_2$$

Again, we choose:

$$\epsilon_1, \epsilon_2 = 2 \times 10^{-6}$$

The following plots investigate how the deployment time T for the Unfold configuration is a function of ξ, β^*, κ^*, θ_{init}, and θ_0.   These variables encompass most of those variables from Table 6 that affect the motion and steady state angular separation of the hinged system without our plots becoming redundant with variables that are closely related to one another. In each of the following cases, one variable is being varied, and the others are fixed at the baseline values given in Table 8.

4.3.3.1.1 Varying damping β

Figure 35 shows how the deployment time T varies as a function of ξ for variable damping coefficient β^*, with spring constant κ^* fixed at its baseline value. The baseline value of β^* is drawn in red. The longest deployment times T are for both overdamped systems (blue, black, and green lines) and underdamped systems. The shortest Ts are for those systems for which β^* for a given κ^* results in close to critical damping behavior (magenta and teal lines). For the overdamped cases (black and gold), higher ξs result in the system being forced to asymptote more quickly towards equilibrium. In the underdamped case (blue), increasing ξ simply increases oscillations and results in the system settling to steady state after increasingly longer times. The blue line experiences ranges over ξ where T does not increase with ξ, followed by ranges where it does. This likely reflects a combination of several factors: an overly restrictive criterion for steady state deployment time (ϵ_1, ϵ_2), the fact that ξ is plotted logarithmically (as it is in all of these figures), and the relative insensitivity of the system to the moment coefficient

at low values, all of which could combine and result in the presence and emphasis of numerical noise, especially for small ξ.

This plot indicates to system designers that for a given $\kappa*$, it is possible to select an ideal, close to critically-damping $\beta*$ (teal and magenta) value that remains ideal regardless of ξs and its internal variables.
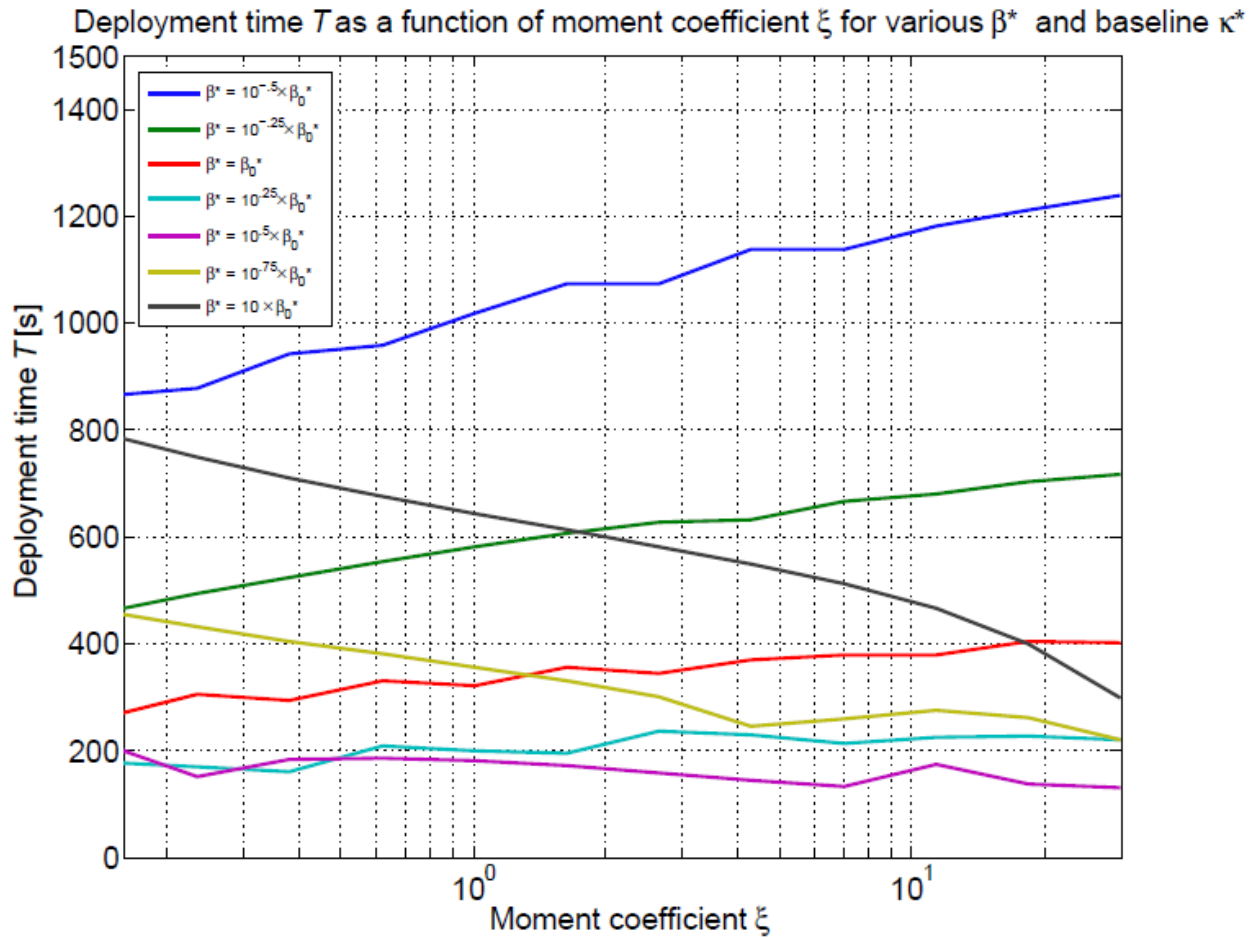

Figure 35: Deployment time T as a function of ξ plotted for different values of $\beta*$ from $10^{-.5}\beta_0*$ to $10\beta_0*$.

4.3.3.1.2 Varying spring constant κ

Figure 36 shows how the deployment time T varies as a function of ξ for variable spring constant κ^*, with β^* fixed at its baseline value. The baseline value of κ^* is not shown in this plot; however, the closest value is $10^{0.09} \times \kappa_0^*$, drawn in teal. The lowest κ^* case plotted here (jagged blue) takes longest to reach steady state for low moment coefficients, because the system is relatively underdamped with respect to the baseline β^*, and, therefore, oscillations are allowed to persist for a longer period of time before reaching steady state. For low κ^*, the system is more sensitive to various combinations of the baseline β^* and ξ, resulting in the jagged nature of the line. For progressively larger κ^*s, the deployment time is relatively insensitive to κ^* itself but increases with ξ and is smoother the higher κ^*.

System designers will want to, for $\xi \gtrsim .1$, choose a low κ^* (like jagged blue) for faster deployment time; for $\xi \lesssim .1$, it is advantageous to choose a κ^* larger than the baseline value.
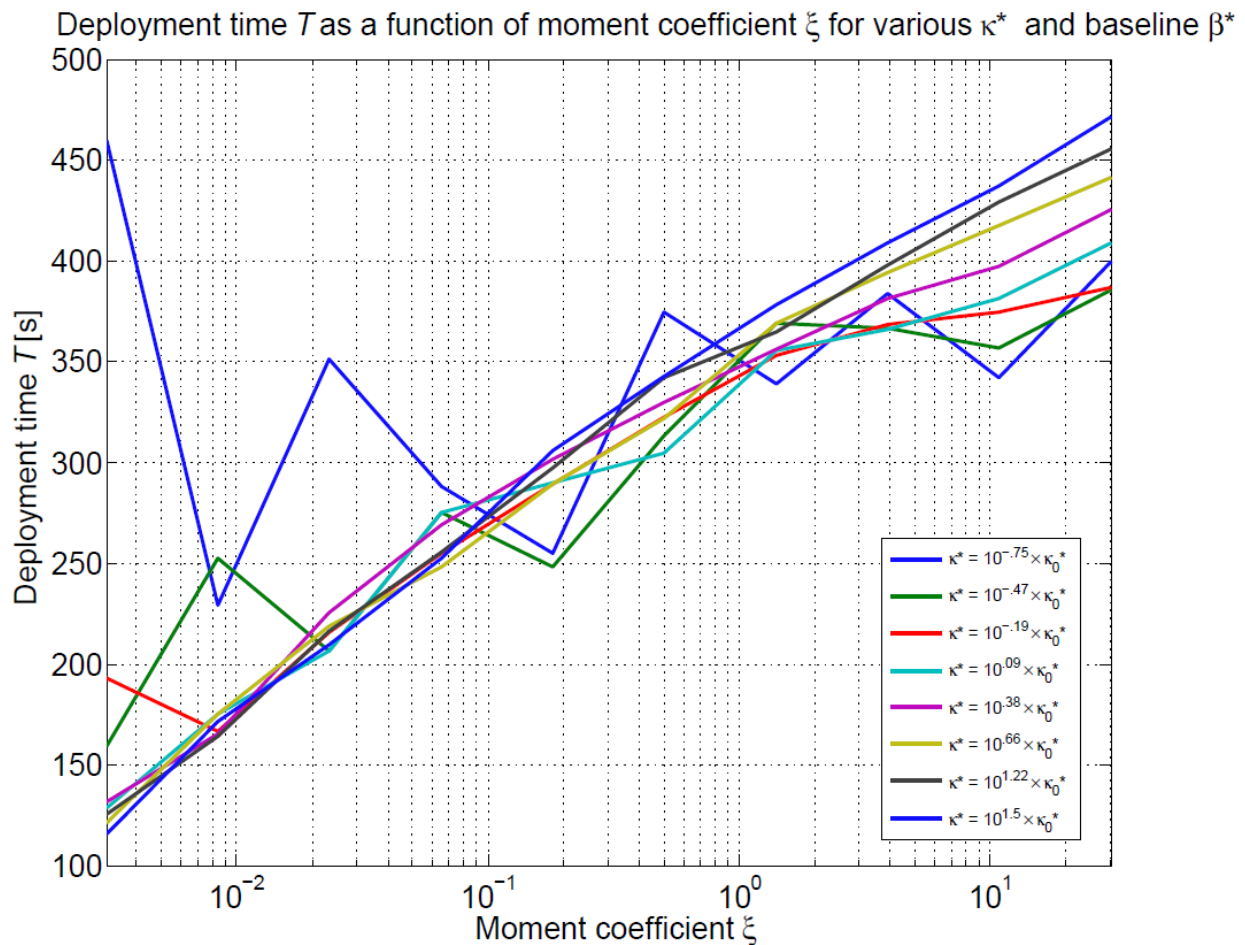

Figure 36: Deployment time T as a function of ξ plotted for different values of κ^* from $10^{-.75}\kappa_0^*$ to $10^{1.5}\kappa_0^*$.

4.3.3.1.3　Varying initial angle θ_0 and natural angle θ_{init}

Figure 37 and Figure 38 show how the deployment time T varies as a function of ξ for variable starting angle θ_{init} with β^* and κ^* fixed at their baseline values. In Figure 37, the natural angle of the spring $\theta_0 = \pi/8$, and in Figure 38, $\theta_0 = 3\pi/4$. These two θ_0 values were selected to bracket a large range of natural angles. The baseline value of both θ_{init} and θ_0 is $\pi/4$, drawn in this plot in teal. Starting the coils at the same angle as the natural angle of the spring (red, or $\pi/8$) results in the shortest deployment times for $\xi \lesssim 0.1$; this is because small moments do not stretch the spring much beyond its natural length, and therefore any disturbances from this θ_0 are smaller and the oscillations of lower amplitude than when $\theta_{init} \neq \theta_0$. For high ξ, $\theta_{init} > \theta_0$ results in the shortest deployment times, because the spring force is already working to resist the electromagnetic repulsion at the start of deployment, so that the system can "settle" into equilibrium relatively quickly. An exception to this observation is $\theta_{init} = 3\pi/4$ (gold), which is so large that the spring force dominates the electromagnetic force and causes the system to oscillate too much.
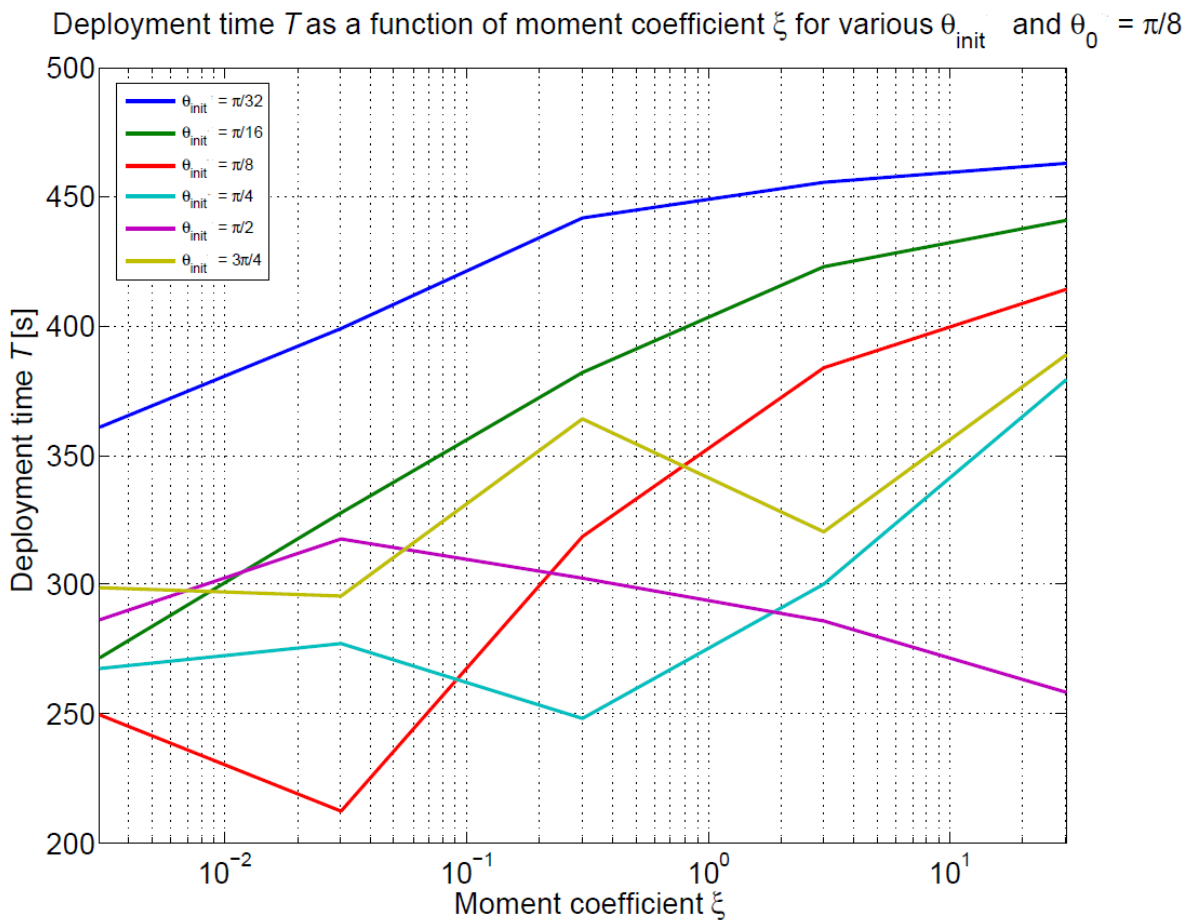

Figure 37: Deployment time T as a function of ξ plotted for different values of θ_{init} from $\pi/32$ to $3\pi/4$ and $\theta_0 = \pi/8$.

In Figure 38, where the natural spring angle $\theta_0 = 3\pi/4$, all of the θ_{init}s plotted are smaller than or equal to the natural spring angle, meaning that the spring force is assisting electromagnetic repulsion from the start of deployment. Therefore, the system will general exhibit oscillations that are larger than the corresponding cases in Figure 37, resulting in the overall deployment times observed below. We also observe that the optimal θ_{init} (for lowest deployment time) increases with increasing ξ from $\theta_{init} = \pi/16$ to $\pi/2$, suggesting that for higher moments, it is preferable to begin at an angle closer to the natural length of the spring but not so large that it causes the system to oscillate too much.

From a systems standpoint and, for most applications, it is desirable for initial deployment to start the coils as close together as possible, to maximize the stowed-to-deployed size ratio of the structure. In that case, while deployment time might not be a primary concern, long deployment times imply large amplitude oscillations at high moments, which are not desirable. A current controller to reduce oscillation seems from these figures to be important for coils that start very close together and thus will experience high initial electromagnetic forces. One reason that the initial angle might be much greater than 0 is for Reconfigure or Deform operations, wherein the panels remain less than π apart, or not quite flat, in order to enable refolding or retracting of a deployed panel via electromagnetic attraction. For those applications, these plots are very useful.
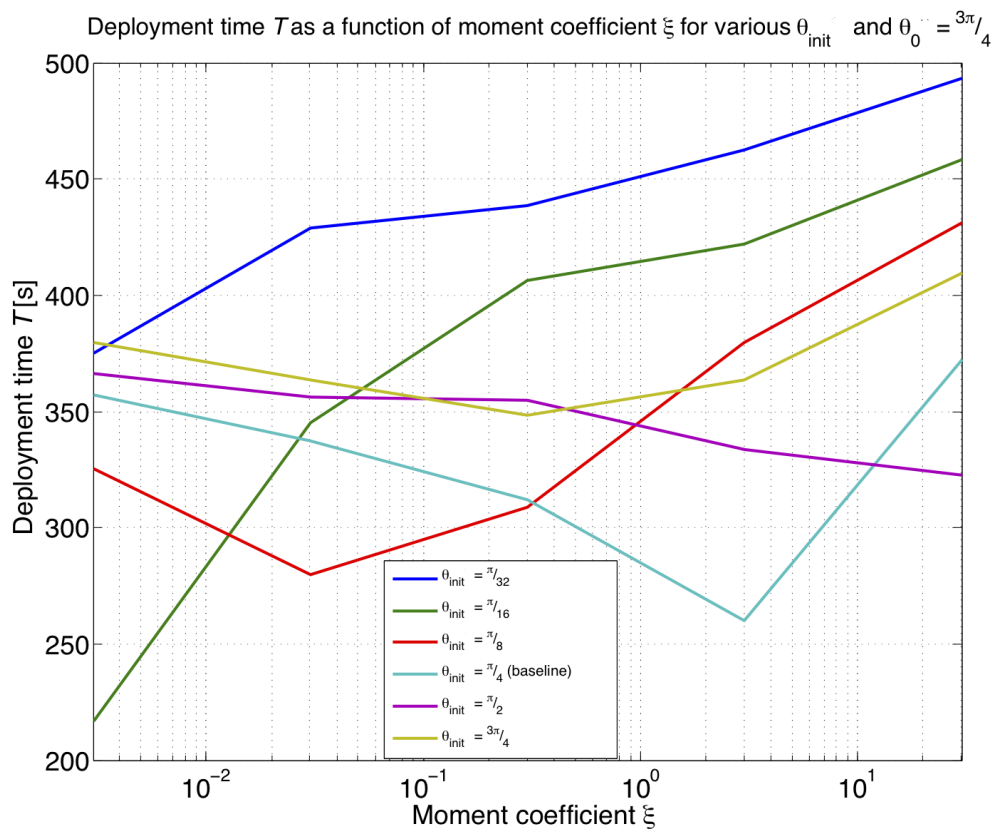

Figure 38: Deployment time T as a function of ξ plotted for different values of θ_{init} from $\pi/32$ to $3\pi/4$ and $\theta_0 = 3\pi/4$.

4.3.3.2 *Moment ξ versus equilibrium angle*

As in the tethered case, the equilibrium angle θ_{eq} defines the final hinge geometry after deployment. θ_{eq} is independent of initial conditions, and damping and is therefore only dependent on the moment coefficient ξ, the spring constant κ^*, and the unstretched natural angle of the spring, θ_0.

4.3.3.2.1 Varying spring constant κ* and natural angle of spring θ_0

In Figure 39, we see how the equilibrium angle depends on the moment coefficient for various values of κ^* and for two different values of θ_0, 0 and π/4. For both values of θ_0, the largest θ_{eq}s are achieved for the smallest spring constants, indicating the inability of the springs to resist larger electromagnetic moments. Subsequently, the system will tend to settle to an equilibrium angle of 180° (blue, green, and red), where the electromagnetic moments also vanish. Similarly to the tethered case, smaller equilibrium angles result from larger spring constants. The effect of increasing the natural spring angle to π/4 is to shift up the equilibrium angles from a minimum of 0 for $\theta_0 = 0$ to a minimum of π/4.

Since equilibrium positions do not depend on inertia, any combination of κ^* and ξ below can be chosen to effect a desired equilibrium angle. System designers can select a κ^* and ξ for their design using this data.
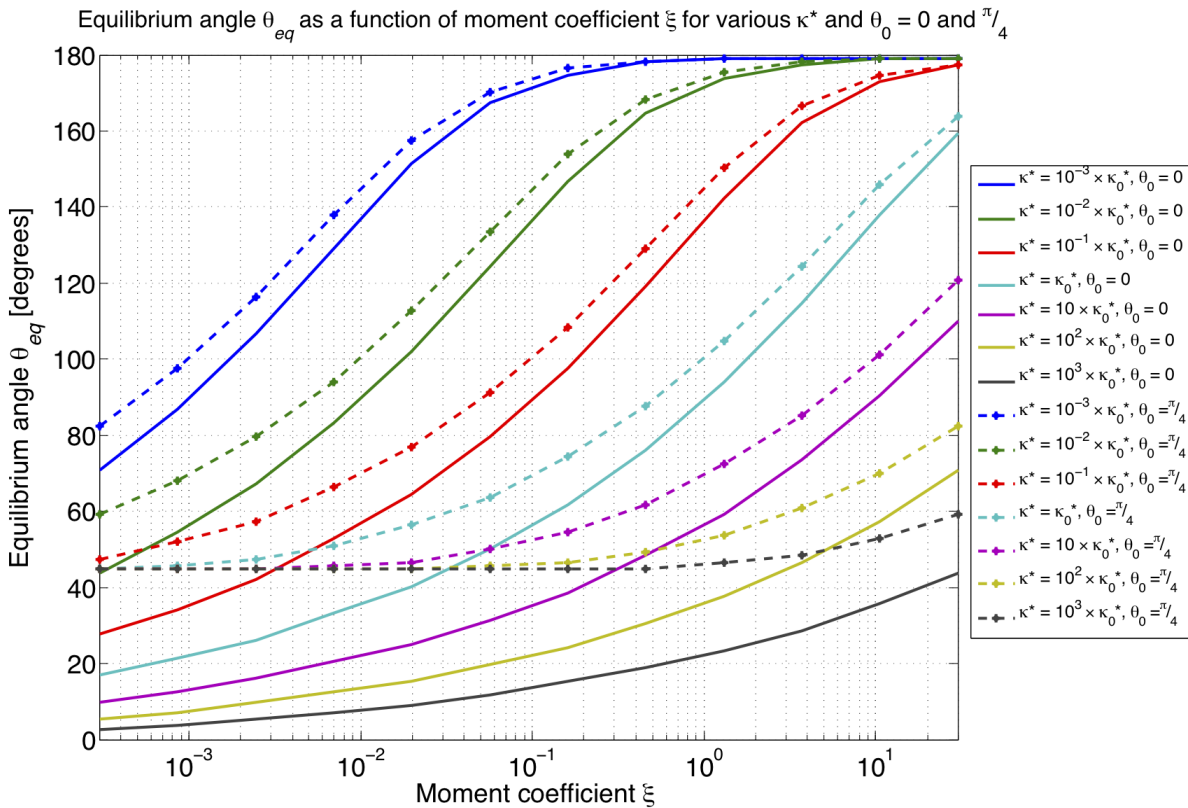

Figure 39: Equilibrium angle θ_{eq} as a function of moment coefficient ξ for various κ^* and θ_0 = 0 and π/4.

4.4   Conclusion

In this chapter, we have made use of the models originally presented in Chapter 3 in order to perform high-level analysis of the interconnectivity of the system variables. This analysis was enabled by introducing a number of dimensionless parameters which combine many of the design variables and facilitate systems-level analysis by reducing the dimensionality of the variable space. We focused on two primary metrics: deployment time T, and the equilibrium or characteristic length L_{eq} (or angle θ_{eq}) of the system after deployment. The effect of varying design variables and their dimensionless counterparts was presented in such a way as to facilitate the decision-making process of a system designer.

5   Chapter 5: Viability

Revisiting the initial questions of the study, we see that Chapter 4 addressed Question 1, the technical feasibility question:

> ***Question 1:*** *Can we use electromagnetic forces generated by and acting between high-temperature superconductor current-carrying coils to move, unfold, and support parts of a spacecraft from its stowed position?*

by exploring the underlying physical concepts of electromagnetic structures and the effect of system parameters on deployment dynamics and steady-state positions.   From Chapter 4, we conclude that the baseline physical principles of HTS structures are sound and that limitations on the use of the technology will come from mission requirements and available subsystem budgets. Questions 2 and 3 both involve the mission and economic viability of HTS structures in the space acquisition environment:

> ***Question 2:*** *For which operations does this technology represent an improvement over existing or in-development options?*

> ***Question 3:*** *What new mission capabilities does this technology enable?*

and will thus be included in this chapter on the viability of HTS structures as a structural technology for space systems. A summary of the general advantages and disadvantages of HTS structures as compared to "traditional" structural options (panels, beams, motors, pyrotechnic bolts) at subsystem levels is included below in

Table 9. Red text indicates a disadvantage, or area where HTS structures are competitively weaker than traditional structures and mechanisms. Green text indicates an ability or property that HTS structures have that traditional structures do not. Black indicates a parameter that depends on the properties of the electromagnetic structure design.

Table 9: Subsystem advantages and disadvantages of HTS structures over traditional options

Subsystem or process	Example impacts of HTS structure choice
Avionics/ Comms	Potential electromagnetic interference
Thermal	Additional thermal control required : heatpipes + cryocoolers, little or no conduction
ADCS	Current regulation needed, Earth's magnetic field, additional momentum trading possible
Optical Path (Payload)	Risks to position accuracy and disturbance control
Structures	Reduction of mass (*extra thermal mass* for each coil cooling system, *but for large structures could be* an overall reduction of mass), vibration isolation, increased compaction/size ratio, enables reconfiguration with no additional components
Propulsion (if formation flying)	No propellant required, eliminates thruster plumes
Power	Additional power draw for both coil currents and cryocoolers
Testing	Difficult in 1g without a complex testing rig

There are three kinds of trades that lead to the selection of an HTS structure design. The first is a mission performance trade, where mission destinations, orbital parameters, and performance needs like reconfigurability are traded based on the high level requirements of the project. Since spacecraft environment is important to the use of HTSs thermally, and HTSs can enable some more difficult performance needs, these trades inform the next kind of trade, which occurs at the subsystem level. At this level, an HTS structural system is compared to other structural options, both traditional and "alternative" (defined below), and the impact of the structural choice on subsystem budgets is evaluated. At the final, component level, trades are performed amongst various HTS designs, such as those in Chapter 4.

In this chapter, we will discuss in a little more detail the comparison between HTS structures and other "alternative" structural technologies like inflatables and tensegrity structures. We will also explore some of the design trades that affect the "internal" variables, or the constituent variables of the dimensionless parameters plotted in Chapter 4, as well as the other variables included in Table 6.

5.1   Alternative structural technology trades

Currently, structural designers reduce structural mass by using lightweight materials, such as aluminum frames, and bydesigning for a high strength-to-weight ratio using isogrid panels and structural optimization. In order for HTS structures to find a foothold amidst these traditional structural options and other innovative, alternative solutions focusing on mass reduction, they should present a strong advantage over other techniques in important metrics like mass, compaction ratio, and thermal and vibrational isolation. Then, despite the additional thermal and power needs of HTS structures, they could still be a preferable selection.

In

Table 10, we summarize important aspects of several leading alternative structural technologies. "Alternative" is taken to mean a departure from purely rigid, metallic structural elements in this discussion, such as composite materials (both rigid and shape memory), tensegrity structures, and inflatable membranes.

Table 10:　Description of alternative structural technologies

Alternative Structural Technology	Description	Contributors/ Projects	Disadvantages w.r.t HTS deployed structures
Composites	• Lightweight and strong • Customizably anisotropic • Maintains shape • Good for enclosures • Can reenter atmosphere • Low coeff. of thermal expansion	• SpaceShipOne • MPCV • ELV payload fairings • Pellegrino (Caltech)	• No thermal or vibrational isolation • No staged deployment • Mostly traditional mechanisms for deployment • No reconfigurability
Tensegrity	• Very lightweight and stiff • Keeps beams under compression with tensioned cables • "Snap out" non-reversible deployment	• Knight, B. • Fuller, B. • Skelton, R. • Snelson, K.	• No thermal or vibrational isolation • Polygonal shapes – may not be advantageous for mirrors or lenses • No reconfigurability • Size limited by beam and tether lengths • No staged deployment
Inflatable	• Very lightweight material • Easy to implement round shapes • Inflates a membranous shell with gas • Compact stowage	• Echo 1 • Explorer 9 • L'garde (Inflatable Antenna Experiment, decoys) • Adherent • Cadogan (ILC Dover)	• Leakage over time (UV curing might help) • One rip renders useless • No reconfigurability • No staged deployment • Compressive loads require pressure or curing • Must carry pressurized gas

5.1.1 Comparison of HTS structures to alternative structural technologies

Table 11 qualitatively lists key trades between HTS structures and other structural support and actuation technologies. The Other Technology column lists the technology against which HTS structures are being compared. The second and third columns show the desirable attributes of the Other Technology versus HTS Structures respectively.

Table 11: Comparison of HTS structures to alternative structural technologies

Other Technology	Other Tech Attribute vs.	HTS Structures Attribute
Inflatables	Low power and potentially lower mass	Longer lifetime
Tensegrity	Low power and no thermal control	Controllability of deployment and potential reversibility
Composites	Low power and no thermal control	Shape change and compaction/size ratio
Pyrotechnics	Reliable impulse	Deployment control and potential reversibility
Piezoelectrics	Precision	Range of motion
Spring-loaded booms and hinges	Lower power and potentially lower mass	Controllability of deployment and potential reversal
Traditional motorized actuators	Heritage	Low mass and thermal/vibrational isolation

Table 12 depicts a qualitative comparison of electromagnetic support and the three structural support technologies listed above (inflatables, tensegrity structures, and composites) across a variety of characteristics of interest for spacecraft designers. Values of these characteristics (in this table, yes, no, or other) that are generally considered good for the specific metric by spacecraft designers are green, values that are dependent on the specifics of the implementation of the technology and could be either good or not are yellow, and those values that are considered less desirable are red. All characteristics are treated equally in this table, but in some applications, some attributes may be valued more highly than others. The takeaway from Table 12 is that HTS structures compare favorably to other structural techniques in most performance metrics associated with spacecraft structures, but that the HTS power and thermal requirements are significantly less desirable. Further development of HTS structures should focus on mitigating the risk that the power and thermal metrics present to successful technology integration.

Table 12: Qualitative comparison of deployable structure options

good either not CHARACTERISTICS OF INTEREST	Composites	Tensegrity	Inflatable	Electromagnetic
Lightweight?	Yes	Yes	Yes	Yes
Strong?	Yes	Yes	If cured/rigidized	Yes
High compaction ratio?	Booms under development	Yes	Yes	Yes
Beams limited by payload fairing	Only if solid panels	Yes	No	No
Traditional deployment mechanisms required (mass)	Often	Yes, high loads/shock otherwise	Yes	No
Durable?	Yes	Yes	No	Yes
Vibrational isolation?	No	No	No	Yes, in some configs
Thermal isolation?	No	No	No	Yes
Low coeff. of thermal expansion?	Yes	If made with composite bars	Only if shape memory polymer (SMP) composites	Yes
Thermal control required?	No	No	No	Yes
Power required for deployment?	No	Depends on method	No	Yes
Staged deployment/ assembly?	No	No	No	Yes
Can be non-polygonal?	Yes	No	Yes	Yes
Reconfigurable w/out mechanisms?	No	No	No	Yes

5.2   Internal variable trades

The variables internal to the nondimensionalized coefficients used in Chapters 3 and 4 encompass other variables in the design vector for an HTS structure, including mass (of coils m, of attached components like m_{panel}, or of the total system m_{tot}), power draw (of each coil, taken as P_{coil}, or of the thermal subsystem, taken as $P_{thermal}$), number of turns in the coil n, diameter of coil D, stowed structure length L_s, the damping coefficient b or β, the spring constant k or κ, the temperature that a coil is maintained at T_e, the magnetic field $\vec{B}$, and the different forces and torques.

Table 13 displays several of these system trades: the first column names an increase or decrease in one variable, and the second column reflects the reactions of other system variables to that change. Red text is a change that is generally not in the direction expressed in an objective vector for spacecraft (an example general one shown below), such as an increase in mass or power. Green text is a change that is in the direction specified in the objective vector, such as a minimization of mass or power. Black text labels variables that can *optionally* be changed along with the first column change and which might be good or bad or neither. In the case of increasing dimensionless spring or damping constants, for example, selection of either of these variables is likely not due to maximizing or minimizing these variables individually but rather through the maximization or minimization of another variable related to both constants from the plotted relationships in Chapter 4, such as equilibrium length.
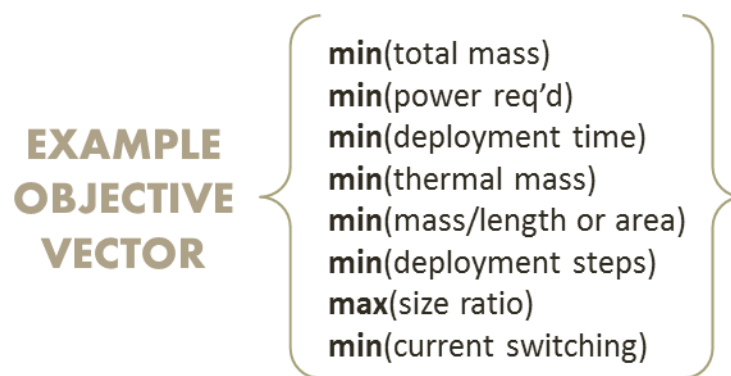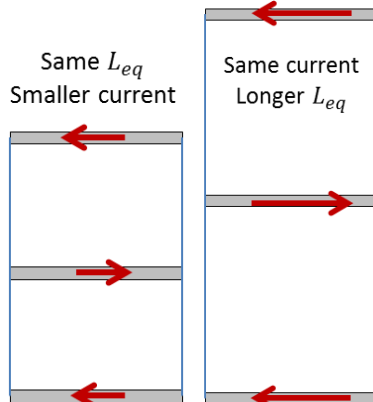
EXAMPLE OBJECTIVE VECTOR

min(total mass)
min(power req'd)
min(deployment time)
min(thermal mass)
min(mass/length or area)
min(deployment steps)
max(size ratio)
min(current switching)

Table 13: System variable trades

Trade	Effects on other variables	Variables involved	Diagram
Temperature of coil T_e ↓ in order to increase critical current density	↑ Thermal power draw ↑ ↑ Magnetic field to mass ratio ↑ ↑ Coil power draw ↑	P_{coil}, $P_{thermal}$, T_e, $\vec{B}$, m	
Number of turns *n* in coil ↑ to increase effective current	↑ Magnetic field from higher effective current ↑ ↑ Mass of coil ↑ ↓ Current through each wire ↓ Power/mass ratio	$\vec{B}$, m_{coil}, P_{coil}, n, I_{eff}	
Radius of coil *R* ↓ to increase magnetic force	↓ Mass of coil ↓ ↑ Magnetic field ↑ ↑ Force ↑ Dimensionless damping Dimensionless spring constant	R, m_{coil}, $\vec{B}$, F, k or κ, b or β	
# of coils *N* ↑ to reduce current in coils or increase characteristic length	↑ Mass of system ↑ ↑ Thermal power draw ↑ and [- Linear structural density - ↑ Characteristic length ↑ ↑ Coil power draw ↑] or [↑ Linear structural density ↑ - Characteristic length- ↓ Coil power draw ↓]	m_{tot}, L_{eq}, P_{coil}, $P_{thermal}$	

Amount of current *I* ↑	↑ Coil power draw ↑ ↑ Magnetic field ↑ ↑ Force ↑ ↑ Characteristic length ↑ ↓ Size ratio ↓ Dimensionless damping Dimensionless spring constant	$P_{coil}, L_{eq},$ $\vec{B}, F, k$ or κ, b or β	

Some more detailed discussion of the trades in Table 13 is included below:

- Temperature of coil T_e ↓
  - This trade makes reference to the relationship between the critical current density that an HTS wire can support and its temperature. As temperature decreases below T_c, the critical current density in the wire also increases, so at colder temperatures, more current can be run through the same coil, and thus a higher magnetic field and force can be generated at the cost of more thermal power (to cool the coil to a lower temperature) and more coil power (to generate the higher current)
- Number of turns in coil *n* ↑
  - Increasing the number of turns in the coil increases the effective current in the coil to

$$I_{eff} = nI$$

and therefore increases γ, increasing the magnetic force. However, when current is flowing through multiple turns of a coil, the magnetic field of one turn exerts a magnetic force on the current in another turn, forcing it towards one side of the wire and effectively reducing the size channel through which the current can flow. The wire's critical current density limits how much current can flow through any portion of the wire's cross section, so once that limit is reached, the total current cannot increase; therefore, additional turns of wire reduce I and result in a loss term.

The same change in power per unit mass value can result from an increase in mass, with power being held constant, or from a decrease in power, with the mass being held constant. The latter would indicate a decrease in effective current unless *n* is being increased and *R* is being decreased to result in the same mass but a higher possible effective current, as observable in the relationship:

$$\frac{P_{coil}}{m_{coil}} = \frac{IV}{n2\pi\rho R}$$

where V is the voltage across the coil and is assumed constant.

- Radius of coil $R \downarrow$
    - We recall that the mass of the coil may be written:

$$m = 2\pi R \rho$$

ρ is the linear density of the coil, given by:

$$\rho = \rho_V n A_c$$

and ρ_V is the volume density of the coil material, *n* the number of turns in the coil, and A_c the cross sectional area of the coil. We may then rewrite the dimensionless force parameter γ as follows:

$$\gamma = \frac{\mu I_{eff,1} I_{eff,2} \mathcal{T}^2}{8\pi^2 \rho R^2}$$

Hence, we see that:

$$\gamma \propto \frac{1}{R^2}$$

so that decreasing the radius of the coil increases the magnetic force.

While it may seem like making *R* arbitrarily small is beneficial due to the increase in the magnetic field through γ, we must keep in mind that changing *R* also has an effect on the dimensionless damping and spring coefficients, *b** and *k**, respectively:

$$b^* = \frac{b\mathcal{T}}{2\pi\rho R}$$
$$k^* = \frac{k\mathcal{T}^2}{2\pi\rho R}$$

Thus, if the designer has a limited choice of actual materials, and hence *b* and *k*, in order to implement a desired dynamical and structural configuration, *R* cannot be made arbitrarily large or small and must in fact be chosen so that the interplay of damping and elastic forces give the desired deployment dynamics and equilibrium configuration as per the analysis in Chapter 4.

- # of coils $N \uparrow$
    - The number of coils in the system N can be increased for one of two primary purposes: the increasing of the characteristic length of the structure with the same current per coil, or the reduction of current through each coil with the same characteristic length. The first purpose results in no increase in the linear structural density, or mass per unit length, whereas the second purpose increases the linear structural density as there are now more coils for the same characteristic length. This dual choice is reflected in the bracketed terms in Table 13. Either choice results in an increase in the mass of the system and in the power required for cooling of the coils.

- Amount of current I ↑
  - For a current density below the critical value for the wire, increases in current result in an increase in the magnetic field and thus electromagnetic force. For a given damping and spring constant, the characteristic length or angle will then increase as a result of the increased electromagnetic force. Thus, the size ratio (stowed-to-deployed) of the system will decrease but the coil power draw will increase due to the increased current.

Now that we have set up the basic constraints on coil motion, in future work we can now expand on these constraints to include multi-operation deployments, complex tether configurations and multi-hinge cases that enable Reconfiguration or temporary Deformation of a paneled structure. These studies, to occur in the course of our Phase II work, will examine the feasibility of "new mission capabilities" as motivated by Question 3.

5.3   Phase II study plans

Our proposed Phase II effort will, in the two additional years of study time beyond the end of this Phase I study, expand upon the primary questions of our Phase I study, develop HTS structures further towards the attainment of TRL 3, and reduce the risks associated with new technology development. Our Phase II effort includes Prof. Raymond Sedwick, Director of the University of Maryland's Space Power and Propulsion Lab, as a co-investigator focused on the development and testing of a flexible cryogenic heatpipe as a key enabling technology for a number of HTS structural applications that require a flexible HTS coil (such as those in the Expand configuration). We also add collaborators from the NASA Goddard Space Flight Center (GSFC) Mission Engineering and Systems Analysis division, including Dr. Carl Adams, assistant chief of technology, to the team to support technology trade studies and integration feasibility assessment and analysis for HTS structures in a large, complex, and fairing-limited precision structure such as the James Webb Space Telescope (JWST).

In our Phase I work, we have identified a number of potential barriers to the feasibility of HTSs as a replacement for traditional structures. We have sorted them into three categories of feasibility barriers to be addressed in Phase II in order of decreasing impact: **Power and Thermal**, **Dynamics and Control**, and **Implementation**. The four impact categories with which each concern is associated: Cost (dollars, mass and power), Spacecraft Performance, Development Time, and Key Enabling Technologies. The three key enabling technologies that our technology development effort focuses on are rigid deploying HTS coils, flexible deploying HTS coils, and flexible cryogenic heatpipes. All of these key technologies require experimental, modeling, and feasibility work in our Phase II effort.

The power and thermal subsystems are those most adversely affected by the use of HTSs, as described earlier in this report. Because a large portion of the power required by HTS structures is consumed by thermal equipment, these two subsystems are inextricably linked in our study of feasibility issues. The power and thermal barriers we will discuss in this section are:

- *Cost:* Complex power and thermal control, generation and management,
- *Cost:* Thermal vacuum chamber testing expenses
- *Performance:* Power for HTS operations needing to be taken from other subsystems
- *Key technology:* Low-power rigid and flexible cryogenic heatpipes
- *Performance:* Lower power cryocoolers

Coil dynamics and control with coil boundary constraints, though, introduce performance feasibility issues that must be addressed in order for any technology advancement to take place and include:

- *Performance:* Coil dynamics
- *Performance:* Stability of configuration
- *Performance:* Position accuracy and knowledge
- *Performance:* Disturbances (Cryocooler vibration, solar pressure)

Implementation feasibility concerns center around the competitiveness of HTS structures with other technologies, either in cost, key performance metrics, or the ability of less complex HTS structures to be competitive enough of a structural option to find purchase on missions in order to gain flight heritage to then motivate the research and development of more complex HTS structures.

- *Cost:* Cost may be uncompetitive with other structural options
- *Performance:* Performance may be uncompetitive in multi-subsystem tradespace
- *Performance:* Potential EMI, negatively affecting other subsystems on board or vice versa
- *Development Time:* Technology roadmap may be too linear to allow missions to use less complex HTS structures as flight hardware prior to completion

Two more years to study the implementation of HTS structures under a NIAC Phase II allows us to:

- Reduce risk in areas of uncertainty with regard to feasibility issues above
- Assess the mission-general and mission-specific (JWST) impact of many of the feasibility issues discussed in this section with simulation and experimentation
- Collaborate with NASA to fully understand the needs of the customer in order to lay out a reasonable and accomplishable roadmap towards integration
- Advance key technologies necessary for full utilization of HTS structural configurations
- Explore the impact of HTS structures on other spacecraft subsystems in greater detail, elaborating on the trades suggested in Phase I with quantitative comparisons

5.4   Summary and conclusions

In this Phase I report, we have conducted an initial feasibility study for the use of high-temperature superconducting coils as deployment and support elements in spacecraft structures. We have also introduced system performance trades that will be further quantified in the Phase II work.

In Chapter 1, we introduced the notion of high-temperature superconductors and the ways they could potentially be useful in spacecraft structures. We discussed the five primary benefits that HTS structures can offer to the aerospace community:

1. Reduced mass
2. Larger structures with same launch vehicles
3. Vibration- and thermally-isolated structures
4. Staged deployment, in-space assembly with fewer operations, and partial system replacements
5. Reconfiguration of structures after deployment

and introduced the three primary research questions relevant to this study.

In Chapter 2, we motivated the work of Chapter 3 by discussing the physical principles underlying superconductivity and how electromagnetic interactions between conducting coils can result in their motion. We also discussed previous work in the use of electromagnetic forces for relative motion, positioning and deployment as well as the state of the industry for superconducting wire construction.

In Chapter 3, we developed the equations of motion for coils responding to electromagnetic forces while under the influence of constraining elements (i.e. tethers and hinged panels) and validated our numerical models against known analytical solutions.

In Chapter 4, we modified our equations of motion for trade analysis by nondimensionalizing them and introducing several dimensionless parameters that encode many of our design variables. We presented the results of numerous simulations using the numerical models introduced in Chapter 3, detailing the response of tethered and hinged coil systems for various dimensionless parameters and, hence, combinations of the original design variables.

In Chapter 5, we discussed on the basis of the results from Chapter 4 the viability of HTS structures in the context of trade analyses. Trades were described at the mission level, the structural subsystem level, and the component level.

On the basis of the work performed in this Phase I study, we have come to the following conclusions:

1) The fundamental physics support the basic concept of using electromagnets for deployment.
2) With existing technology and capabilities, the use of HTS coils for the deployment activities investigated herein is achievable, though with significant work to be done in dynamic controllability, system optimization, sizing and scaling, thermal control, and mission integration analysis. Our Phase II work will address many of these topics as well as economic viability.

By the end of Phase II, we aim to have completed and tested an experimental flexible cryogenic heatpipe, a technology integration case study of JWST, laboratory experimental demonstrations of HTS coils unfolding panels and separating while superconducting, and models calibrated both by experiments and analytical solutions. These are the first steps along the HTS technology demonstration path, and those steps combined with the foundation laid in our Phase I report and the feasibility and implementation analysis to be conducted in Phase II will bolster the credibility and prepare the technology for further TRL advancement.

6　Works Cited

1]　J. R. Wertz, *Space Mission Engineering: The New SMAD,* Microcosm Press, 2011.

2]　D. A. Bearden, "When is a Satellite Mission Too Fast and Too Cheap?," in *MAPLD International Conference*, 2001.

3]　http://www.lhc-closer.es, "Superconductivity in Short," [Online]. Available: http://www.lhc-closer.es/php/index.php?i=1&s=4&p=8&e=0. [Accessed 21 May 2012].

4]　Bruker Daltonics, "Record current with powder-in-tube superconductor," 2008.

5]　V. Selvamanickam, "Coated Conductors: From R&D to Manufacturing to Commercial Applications," in *Superconductivity Centennial Conference*, Den Haag, the Netherlands, 2011.

6]　SuperPower Inc., "SuperPower®2G HTS Wire Specifications," [Online]. Available: http://www.superpower-inc.com/system/files/SP_2G+Wire+Spec+Sheet_for+web_2012FEC_v2_0.pdf.

7]　"HTS Cable and weave closeup," General Cable Superconductors Ltd, 2009. [Online]. Available: http://www.gcsuperconductors.com/about-us/galleries/gcsgallery/hts-cable-and-weave-closeup.

8]　J. Llambes and D. Hazelton, "Advantages of Second-Generation High Temperature Superconductors for Pulsed Power Applications," in *Pulsed Power Conference*, Washington, DC, 2009.

9]　L. L. Jones, W. R. Wilson, J. Gorsuch, J. Shoer and M. Peck, "Flight Validation of a Multi-Degree-of-Freedom Flux-Pinned Spacecraft Model," in *AIAA Guidance, Navigation, and Control Conference*, Portland, 2011.

10]　M. Shao, S. Turyshev, N. Pedreiro, D. Tenerreli, A. Carrier and S. Doravari, *New Sciencecraft and Test Mass Concepts for the LISA Mission,* 2011.

11]　D. Kwon and R. Sedwick, *Cryogenic Heat Pipe for Cooling High Temperature Superconductors with Application to Electromagnetic Formation Flight Satellites,* Massachusetts Institute of Technology, 2009.

12]　L. M. Elias, *Dynamics of Multi-Body Space Interferometers Including Reaction Wheel Gyroscopic Stiffening Effects: Structurally Connected and Electromagnetic Formation Flying Architectures,* MIT, 2004.

13]　R. Zubrin, "NIAC Study of the Magnetic Sail," NASA, 1999.

14] J. Powell, G. Maise, J. Paniagua and J. Rather, "Magnetically Inflated Cable (MIC) System for Large Scale Space Structures," NASA Institute of Advanced Concepts, 2006.

[15] G. Benford, O. Goronostavea, A. Prichard, J. Benford, L. Nakodym, D. Vaughan and H. Harris, "Sail deployment by microwave beam—experiments and simulations," in *Space Technology And Applications International Forum*, Albuquerque, 2002.

[16] K. Amboss and W. Knauer, "Lightweight Reflecting Structures Utilizing Magnetic Deployment Forces". United States of America Patent 3605107, 17 July 1969.

[17] R. Sedwick and D. Kwon, *Cryogenic Heat Pipe for Cooling High Temperature Superconductors with Application to Electromagnetic Formation Flight Satellites,* Massachusetts Institute of Technology, 2009.

[18] Sunpower Corporation, "Sunpower Inc. - The CryoTel Family of Cryocoolers," [Online]. Available: http://www.sunpower.com/cryocoolers/cryotel.php. [Accessed 25 May 2012].

[19] J. R. Wertz, Spacecraft Attitude Determination and Control, D. Reidel, 1980.

[20] S. Schweighart, Electromagnetic Formation Flight Dipole Solution Planning, Cambridge: Massachusetts Institute of Technology, 2005.

[21] D. W. Hazelton, F. Roy and P. Brownsey, "Superpower Inc. Recent Developments in 2G HTS Coil," in *2011 EUCAS (European Conference on Applied Superconductivity)*, Den Haag, The Netherlands, 2011.

[22] Sunpower Corporation, "CryoTel Cryocooler FAQs," [Online]. Available: http://www.sunpower.com/cryocoolers/faq.php.

[23] D. Kwon, *Electromagnetic Formation Flight of Satellite Arrays,* Massachusetts Institute of Technology, 2005.

[24] R. Sedwick, *Subproposal to MIT on NASA NIAC Phase II Proposal,* College Park, 2012.